学位論文

Evolution and nucleosynthesis of massive first stars

（大質量初代星の進化と元素合成）

東京大学大学院理学系研究科
天文学専攻

髙橋 亘

Abstract

A few hundred million years after the Big Bang, dark ages of the universe ends with the emergence of first stars. First stars, also known as the Population III (Pop III) stars, severely impact on the environment of the early universe; they initiate the cosmic re-ionization by emitting high energy photons, they synthesize heavier elements than ^{7}Li, introducing diversities in the baryon matters, and the final explosions as supernovae crush and inject the synthesized material into the ambient primordial gases.

Understanding the nature and properties of the first stars is one key topic in modern astronomy and astrophysics. In this work, I purpose to constrain the important properties of first stars, the initial masses and the rotation properties. Demand for this kind of constraints has been increasing, as resent cosmological simulations provide valuable information on the first star formation, such as the wide initial mass distribution of $\sim$ 10–1000 $M_\odot$ and rapid rotation at their birth. I conduct detailed comparisons between the theoretical yields of first stars and the abundance patterns of metal-poor stars. Key idea is that metal-poor stars existing in the local universe would be born from the chemically primitive gas clouds existed in the early universe. Assuming that the signatures of the first nucleosynthesis are imprinted on the characteristic abundance patterns in metal-poor stars, the abundance comparison provides the properties of Pop III source stars.

Yields of Pop III core-collapse supernovae are calculated for 12–140 $M_\odot$ rotating and non-rotating first stars. The novelty of this part is to take the wide initial mass range and the effect of rotation into account for Pop III stellar yields. The stellar evolutions are firstly calculated, then metal ejections by supernova explosion are calculated by the weak explosion model, in which only outer distributing matter, which is not affected by the explosive nucleosynthesis, is ejected. I find some characteristic nucleosynthesis taking place in the outer shell-helium regions. Intermediate-mass α elements of Mg and Si are abundantly produced by more massive models, and only rotating models produce N, Na, and Al. These characteristic patterns are well reflected in the stellar yields and enable us to constrain the properties of source stars of metal-poor stars. More massive 145–260 $M_\odot$ first stars are confirmed to explode as pair-instability supernovae. The full evolution from the zero-age-main-sequence phase to explosion in addition to the nucleosynthesis is systematically calculated for non-rotating progenitors for the first time. I find that the characteristic odd-even variance is indicated by nearly mass-independent ratios of [Na, Al, Sc/Mg], the ratios of [Si, Ca/Mg] are useful to determine the initial mass, and the low [Ni/Fe] or [Zn/Ni] ratios indicate the low temperature explosion of PISN. These abundance patterns are useful to discriminate the hypothetical PISN children from the other metal-poor stars.

The yields of the weak explosion model are compared with the three most-iron-deficient stars discovered so far. The abundance pattern in SMSS 0313-6708

is well explained by 50–80 M$_\odot$ non-rotating models, rotating 30–40 M$_\odot$ models well fit the abundance of HE 0107-5240, and both non-rotating and rotating 15–40 M$_\odot$ models explain HE 1327–2326. Next, the first systematic comparison of theoretical PISN yields with a large stellar abundance data compiled in *SAGA* database including SDSS J0018-0939 is conducted. While no metal-poor star is found from the sample to show the characteristic signatures of PISN yields, the robust capability of utilizing the ratios of [Na, Ca, Sc, Cr, Co, Zn/Mg] for the discrimination is shown.

In conclusion, I have obtained the indication of the existence of $\sim$ 15–80 M$_\odot$ first stars for the first time. Some of them would rotate, but some of others would not. This indicates the diversity of the rotation properties of the first stars. On the other hand, signatures of more massive weak supernovae from $\sim$ 100–140 M$_\odot$ stars have not yet found. Moreover, no metal-poor stars in the current big sample of *SAGA* database are found to exhibit signature of PISN yields occurring from 145–260 M$_\odot$ first stars. The lack of the children of very massive first stars is incompatible with the wide initial mass distribution of first stars estimated by the recent cosmological simulations.

Acknowledgments

I express my greatest appreciation to my supervisor Hideyuki Umeda and to my collaborator Takashi Yoshida for many years of supports, discussions, and encouragements on my research. I sincerely thank the collaborators Kohsuke Sumiyoshi and Shoichi Yamada for many stimulating discussions and helpful supports. I am deeply grateful to members of the Department of Astronomy for long years daily supports. A part of this work has been done during a half-year visit at the Geneva Observatory. I express my deepest gratitude to Prof. George Meynet and to his laboratory members Authur Choplin and Giovanni Privitera for their respectful accommodations and helpful supports.

I appreciate indications and suggestions by the examiners, Yuzuru Yoshii (chief), Izumi Hachisu, Kazuyuki Omukai, Toshitaka Kajino, and Yoichi Takeda, which improve the quality of this thesis. I would like to appreciate many exciting discussions and interesting suggestions on this work by Nozomu Tominaga, Shingo Hirano, Takuma Suda, and Wako Aoki. I would like to thank Sylvia Ekström and Cyril Georgy for insightful discussions on the stellar evolution and helpful assistance for the usage of GENEC. I am grateful to Stanford Woosley, Alexander Heger, Bill Paxton, Frank Timmes, Norbert Langer, Georges Meynet, and Alessandro Chieffi for providing detail information about energy generation rates in their code. I am also thankful to Alex Heger for providing pre-collapse structures of their PISN models.

Finally, I wish to thank my family for their understanding and continuous support during my life.

Contents

List of Figures

List of Tables

Chapter 1

Introduction

First stars, also known as Population III (Pop III) stars, were key drivers of the evolution of the early universe. Their high energy radiations constituted an important component of ionizing photons to initiate the cosmic re-ionization. They were the first nuclear reactors in the chemically primitive universe, creating heavier isotopes than ^{7}Li. Massive first stars, furthermore, would explode as first supernovae in the universe. The explosions spread over the circumference, crushing and heating up the ambient gases. Processed stellar materials were ejected by the explosions and mixed with the primordial gases, changing the chemical properties.

A number of questions arise on the nature of the first stars. How these first stars evolve and end their lives? What are the evolutionary properties that characterize them from metal-rich stars? What kind of nucleosynthesis takes place, and how do they eject the processed materials out to the primordial circumference? More to say, how can we answer to those questions?

1.1   Formation of first stars

Formation of the first stars has been extensively investigated by cosmological simulations over the past decades (e.g., Abel et al., 2002; Bromm et al., 2002; Yoshida et al., 2004). The unique advantage of these simulations is that the high precision initial conditions can be obtained from the direct application of the ΛCDM model of cosmological structure formation, which is calibrated by *WMAP* (Komatsu et al., 2011) and more recently by *Planck* (Planck Collaboration et al., 2014) satellites. The ab-initio cosmological simulations treat dynamics of dark matters together with hydro-thermo-dynamic evolution of gases in a general-relativistically evolving frame. Firstly a primordial gas cloud, embedded in a dark matter mini-halo of 10^5–10^6 M$_\odot$, collapses at redshifts $z \sim 20$–30 due to gravitational instability (Yoshida et al., 2003). The adiabatic collapse increases the temperature of the primordial gas cloud, resulting in stabilization of the structure. As more efficient cooling due to atomic-hydrogen needs higher temperature to operate, further collapse requires molecular-hydrogen cooling that activates in lower temperature environment. Experiencing complicated chemical evolution of atomic and molecule hydrogen (e.g. Omukai & Nishi, 1998a), finally a proto-stellar core of ~ 0.01 M$_\odot$ is

formed in a gas cloud of ~ 1000 M$_\odot$ (e.g., Omukai & Nishi, 1998b; Yoshida et al., 2008).

The evolution of the core during the successive accretion phase remains unclear. Traditionally, it was believed that the high gas temperature results in the high accretion rate onto the proto-stellar core, according to a simple estimate of $\dot{M}_{\rm acc} \simeq M_{\rm Jeans}/t_{\rm ff} \propto T^{3/2}$, where $\dot{M}_{\rm acc}$, $M_{\rm Jeans}$, and $t_{\rm ff}$ are the accretion rate, the Jeans mass, and the free-fall time of the gas cloud, respectively. Hence, a massive initial mass of the first star was estimated from the high accretion rate, reaching ~ 100 M$_\odot$ or even higher (Bromm & Larson, 2004). On the other hand, recent simulations claim that other important processes, such as irradiation by the protostar (McKee & Tan, 2008; Hosokawa et al., 2011, 2012) and disk rotation and fragmentation (e.g., Stacy et al., 2010; Clark et al., 2011), significantly affect the accretion history.

The large angular momentum of accreting gas not only enables to form a rapidly rotating first star (Stacy et al., 2011, 2013), but also decreases the mass accretion rate and allows a disk to form around the core (Tan & McKee, 2004). In the growing accretion disk, global gravitational instabilities are suggested to set in (Gammie, 2001). A small perturbation thus grows and finally disrupts the disk, triggering disk fragmentation. This indicates that Pop III stars may have a large fraction of binaries or multiple systems (e.g., Greif et al., 2012). The possible binary or multiple system formation is especially important as small mass metal-free stars can be formed from the path (Clark et al., 2011). A small mass Pop III star of $\lesssim 0.8$ M$_\odot$ can survive the long history of the universe, thus still to be observable in our Galaxy, if it exists. However, the fate of the fragmented disk is not so clear. A recent three-dimensional simulation including the effects of UV feedback suggests that many fragmented segments migrate inward and finally accrete onto the central star (Hosokawa et al., 2016). On the contrary to the multiple system formation, this process rather enhances the mass accretion rate.

Radiation from the proto-star is another process to reduce the mass accretion rate. Once the central proto-star has grown to ~ 10 M$_\odot$, the UV radiation from the star evaporates the accretion disk, intercepting the further accretion to take place (Omukai, 2001; McKee & Tan, 2008). Since this is a feedback process, in which the source star of the UV radiation itself is affected by the mass accretion, a self-consistent simulation is desired for the accurate estimation. Such a work is firstly done by Hosokawa et al. (2011), who show that the efficient UV radiation feedback indeed regulates the mass accretion rate and accordingly a first star of a few tens of solar masses is formed. Furthermore, the same consistent calculation is conducted for a large number of samples collected from a cosmological simulation in Hirano et al. (2014). They obtain a wide spread initial-mass-distribution, spanning from ~ 10 M$_\odot$ to ~ 1000 M$_\odot$, for Pop III stars (Hirano et al., 2015).

1.2 Evolution of first stars

The fundamental importance of first stars provokes extensive investigations on the evolution (Woosley & Weaver, 1995; Chieffi et al., 2001; Schaerer, 2002; Marigo et al., 2001, 2003; Siess et al., 2002; Chieffi & Limongi, 2004; Umeda & Nomoto,

2002, 2005; Gil-Pons et al., 2007; Lau et al., 2008; Ekström et al., 2008; Heger & Woosley, 2002, 2010; Chatzopoulos & Wheeler, 2012; Yoon et al., 2012, 2015).

These authors have calculated evolution of first stars utilizing stellar evolution codes, which are generally calibrated to give reasonable agreements to stars, especially to the sun, in our Galaxy and Magellanic clouds. In this meaning, calculations of Pop III stellar evolution inherit the large uncertainties in the treatments of macroscopic physics of convection, wind mass loss, and stellar rotation, which are generally described by parameterized phenomenological approaches. On the other hand, only the intrinsic uncertainties are incorporated in the microphysics, such as the opacity, the nuclear reaction rates, and the neutrino emission rates. Especially, the initial composition of first stars are provided by the accurate and precise theory of big-bang nucleosynthesis (e.g. Steigman, 2007),

One important effect of first stars on the environment is radiation of ionizing photons (Schaerer, 2002). Owing to the much more compact structure than stars in the local universe, massive first stars radiate exceptionally strong ionizing fluxes (Tumlinson & Shull, 2000). The intensity of the ionizing flux mainly depends on the initial mass of the first star. Those ionizing radiations not only initiate the cosmic re-ionization (e.g. Haiman & Loeb, 1997) but also possibly change the path of the nearby star formation to the so-called Pop III.2 channels, in which photo-ionized gases enhance H_2 and HD formation (Yoshida et al., 2007) or photo-dissociated gases lose the molecule coolants (Omukai & Palla, 2001; Omukai & Yoshii, 2003). The resulting star formation is thus much different from the usual Pop III stellar formation (Johnson & Bromm, 2006; Hirano et al., 2015).

The other important effect is the final explosion of a massive first star (Woosley & Weaver, 1995; Heger & Woosley, 2002; Umeda & Nomoto, 2002, 2005). The supernova explosion spreads a large quantity of energy and metals out the ambient gases, both of which significantly affect the environment (e.g. Ferrara et al., 2000). Similar to supernovae in the local universe, supernovae in the early universe can be diverse. The main parameter of a massive star to determine the fate is the initial mass. A less massive first star of $\sim$ 9–10 $M_\odot$ may become a less energetic electron-capture supernova (Miyaji et al., 1980; Takahashi et al., 2013; Kitaura et al., 2006), a massive star of $\sim$ 10–25 $M_\odot$ will explode as a core-collapse supernova (CCSN) with the energy of $\sim 10^{51}$ erg, and a more massive 25–40 $M_\odot$ star may become a ten times more energetic supernova, so-called hypernova (Nomoto et al., 2006). Possibly not all of massive stars succeed to explode, but some part of them become faint- or failed-supernovae (Hamuy, 2003). Furthermore, an energetic explosion of pair-instability supernova (PISN) will arise from the very massive mass range of 145–260 $M_\odot$ (Heger & Woosley, 2002; Umeda & Nomoto, 2002). Type Ia supernova (SN Ia), which is resulting from thermonuclear explosion of a CO white dwarf, chiefly contributes to production of iron (Nomoto et al., 1984), hence it works to reduce other abundance ratios such as [O/Fe][1] (Kobayashi et al., 1998). Since SN Ia is estimated to have much longer lifetime of billions of years than supernovae from massive stars (based on a galactic chemical evolution, Yoshii et al. 1996; and

---

[1]Here $[A/B] \equiv \log_{10}(N_A/N_B) - \log_{10}(N_A/N_B)_\odot$, where the subscript $\odot$ denotes the solar value and N_A and N_B are the number abundances of elements A and B, respectively.

on a delay time distribution, Totani et al. 2008), the contribution to the metal pollution is believed to initiate from [Fe/H] $\gtrsim -1.0$ (Kobayashi et al., 2006).

In addition to the initial mass of the first star, stellar rotation is the second important parameter to determine the evolution of first stars (Meynet & Maeder, 1997). Calculations with solar metallicity have shown that inclusion of stellar rotation broadly impacts the outputs of stellar evolution, such as the stellar structure, the wind mass loss, the nucleosynthesis, and the fate (Meynet & Maeder, 2000; Heger et al., 2000). With a decreasing metallicities, the effects of rotation are found to be enhanced, since more effective rotationally induced mixing takes place in the more compact structure and the braking effect by the wind mass loss is reduced (Meynet & Maeder, 2002a; Yoon et al., 2006; Hirschi, 2007). Therefore, it is naturally expected that stellar rotation also has an impact on the evolution of first stars.

In the past decade, several works have been done to calculate the evolution of rotating first stars (Marigo et al., 2003; Ekström et al., 2008; Chatzopoulos & Wheeler, 2012; Yoon et al., 2012, 2015). Ekström et al. (2008) have calculated the evolution of rotating first stars with masses between 9 and 200 $M_\odot$ until depletion of the central silicons. They have found that the rotationally induced mixing triggers high nitrogen production in the first stars, while the suggested enhancement of mass loss has found not to take place (Meynet et al., 2006). Yoon et al. (2012) have calculated a grid of massive Pop III models, covering the range of mass from 10 to 1000 $M_\odot$ and the range of rotational velocity from zero to 100% of the critical rotation. The exciting result they have obtained is the realization of the chemically-homogeneous-evolution (CHE) (Maeder, 1987) in their fastest rotating models. As a large quantity of angular momentum can be preserved in the homogeneous star, the CHE is considered to be the key evolution path to trigger a long-GRB jet (Yoon & Langer, 2005; Woosley & Heger, 2006). While those previous works reveal properties of divergent evolution of rotating first stars, the supernova nucleosynthesis have not yet calculated.

In spite of extensive investigations over many years, accurate simulation of supernova explosion is still a numerically challenging task (e.g., Janka, 2012; Kotake et al., 2012; Bruenn et al., 2013; Burrows, 2013). Therefore, many investigations on yields of Pop III supernovae have conducted simulations by much simplified manners. Often the engine of the explosion is approximated by injecting an energy into the central region of the star in terms of the thermal energy (the *thermal-bomb* model, Hashimoto et al., 1989), the kinetic energy (the *piston* model, Woosley & Weaver, 1986), and combination between them. Moreover, in order to mimic the multi-dimensional nature during the matter ejection, the so-called *mixing-fallback* model has been introduced by Umeda & Nomoto (2002). In the model, an explosion is assumed not to eject the whole stellar mass, but some fraction of mixed inner material falls back onto the central remnant. Accordingly, this model has three basic parameters, the inner boundary of the mixing region corresponding to the initial mass of the compact remnant, $M_{\rm cut}$, the outer boundary of the mixing region, $M_{\rm mix}$, and the escape fraction with which the matter in the mixing region is ejected, $f_{\rm esc}$ (Tominaga et al., 2007a). Two schematic illustrations are discussed to account for the mixing-fallback process. The first one is a low energy supernova.

At the boundary region of a stellar core, deceleration by the reverse shock takes place (e.g., Hachisu et al., 1990; Kifonidis et al., 2003). The deceleration accounts for the large fallback of inner matter, simultaneously explaining the mixing by the growth of the Rayleigh-Taylor instabilities. The other one is a jet-like explosion (Tominaga et al., 2007b; Tominaga, 2009), in which large fallback is attributed to the accretion of off-axis matter.

1.3   Metal poor stars

The oldest and most metal-poor stars in the local universe contain invaluable information of nucleosynthesis in the early universe in their primitive chemical abundances (e.g., Frebel & Norris, 2015; Nomoto et al., 2013). Recent cosmological simulations estimate that the first metal enrichment can be as high as $Z \sim 10^{-3}$ $Z_\odot$ (Greif et al., 2010; Smith et al., 2015; Ritter et al., 2012, 2016). Besides, due to the pre-existing small amount of metals, even a single metal ejection can dominate the primitive chemical abundance of ambient gases (Audouze & Silk, 1995; Ryan et al., 1996). Since the second-generation stars should be born from such chemically primitive gases, an anticipation exists that the most metal-poor stars observed in the local universe may actually be the second-generation stars, based on their extremely metal poor abundances and the intrinsically large scatters observed in many elemental abundances (e.g. Umeda & Nomoto, 2003).

Recently, growing number of such objects has been discovered and observed by several surveys. Some of them facilitate a low-resolution prism spectroscopy with a wide viewing angle to find an indicative CaII K line, which provides a first estimate of the stellar metallicity (e.g., HK survey: Beers et al. 1992; Hamburg/ESO survey: Christlieb 2003). Some others utilize a big medium-resolution spectroscopic data to find metal-poor signatures (e.g., SEGUE survey: Yanny et al. 2009; LAMOST survey: Deng et al. 2012). The SkyMapper Southern Sky Survey (SMSS survey: Keller et al. 2007), by which the most iron-poor star, SMSS 0313-6708 of [Fe/H] < -7.3, has been discovered (Keller et al., 2014), is a photometric survey, which uses the UV excess as the metallicity estimate.

Among the metal-poor stars, stars showing smaller metallicity of $-4.0 \leq$ [Fe/H] < -3.0 are called extremely-metal-poor (EMP) stars. Similarly, stars of $-5.0 \leq$ [Fe/H] < -4.0, $-6.0 \leq$ [Fe/H] < -5.0, and [Fe/H] < -6.0 are respectively named ultra-metal-poor (UMP), hyper-metal-poor (HMP), and mega-metal-poor stars (Beers & Christlieb, 2005). More metal-poor stars are much rarer (Yong et al., 2013b). Currently ~ 20 stars have been discovered having [Fe/H] < -4.0 in our Galaxy, and the number reduces to 6 with [Fe/H] < -5.0 (Christlieb et al., 2002; Frebel et al., 2005; Caffau et al., 2011a; Keller et al., 2014; Bonifacio et al., 2015; Frebel et al., 2015). Peculiar characteristics of the abundance patterns are not only the low iron abundance. Interestingly, all of the six most-iron-poor stars except Caffau star show an over abundance of carbon relative to iron, [C/Fe] $\gtrsim$ -3. It is also noteworthy that the enhancement of intermediate mass elements, such as carbon, nitrogen, oxygen, sodium, magnesium, and aliminum is frequently observed from the most iron-poor stars (Norris et al., 2013).

Although abundances of metal-poor stars show intrinsically large scatters, some trends have been found in their averaged abundances. For example, $[\alpha/\text{Fe}]$ is known to reach a constant value of ~ 0.5 at $[\text{Fe/H}] < -1.0$ and abundance ratios of odd elements such as [Na, Al, Cu/Fe] decrease toward low $[\text{Fe/H}]$. Also iron-peak elements show decreasing [Cr, Mn/Fe] and increasing [Co, Zn/Fe] trends with decreasing $[\text{Fe/H}]$ (McWilliam et al., 1995). Considering a galactic chemical evolution model, in which interaction between chemical enrichment by several processes and next generation star formation is simulated, many of these trends have been explained (e.g., Timmes et al., 1995; Kobayashi et al., 2006). On the other hand, still significant underproductions are found in some of odd- or iron-peak elements, such as [K, Sc, Ti, V/Fe] (Nomoto et al., 2013).

Metal-poor stars with large carbon excess of $[\text{C/Fe}] > 0.7^2$ are called carbon-enhanced-metal-poor (CEMP) stars (Aoki et al., 2007). The fraction of CEMP stars increases with decreasing metallicity (e.g., Beers et al., 1992; Aoki et al., 2007). Moreover, the bimodal distribution of carbon abundances has been discovered in CEMP stars (Bonifacio et al., 2015). Based on the abundances of neutron-rich isotopes, CEMP stars are further classified into four subclasses (Beers & Christlieb, 2005); CEMP-s stars showing s-process element enhancement, CEMP-r stars with r-process element enhancement, CEMP-r/s stars with both s- and r-elements enhancements, and CEMP-no stars with no neutron rich element enhancements. Among them, CEMP-s stars dominate the large fraction of the CEMP stars. As majorities of CEMP-s (Johnson & Bolte, 2002), CEMP-r, and CEMP-r/s stars have metallicities of $[\text{Fe/H}] \gtrsim -3.0$, CEMP stars of $[\text{Fe/H}] < -3.0$ are expected to be dominated by CEMP-no stars.

Origins of carbon enhancement will be different for each classes. Based on the high binary frequency, the origin of the carbon enhancement in CEMP-s stars has been elucidated as the mass transfer from the former AGB binary (Suda et al., 2004; Lucatello et al., 2005). On the other hand, origins of carbon enhancements in CEMP-r, CEMP-r/s, and CEMP-no stars are unclear. Besides the AGB mass transfer model, other models, such as the faint supernova model (e.g. Umeda & Nomoto, 2003; Iwamoto et al., 2005), superposition of two supernovae (Limongi et al., 2003), the spin-star model (Meynet et al., 2006), and the self-enrichment model (Fujimoto et al., 2000), have been proposed to explain the carbon enhancement.

1.4 Goal and purposes of this thesis

The final goal of this work is to reveal and to understand the properties of first stars existed in the early universe. Because it is extremely challenging to directly observe such high-z objects by present telescopes, I decide to take more indirect but reasonable strategy, by conducting the so-called *abundance profiling* method (Nomoto et al., 2013). The key idea is that chemically primitive abundances observed from metal-poor stars in the local universe may preserve nucleosynthetic signatures occurred in the early universe. Assuming in this way, I try to make

---

^{2}Sometimes > 1.0 is used; Beers & Christlieb 2005.

a link between the theoretically calculated yields of first supernovae in the early universe and the observationally collected abundances of metal-poor stars in the local universe.

In this thesis, I purpose to constrain the properties of first stars, such as the initial masses and the rotational properties. By conducting the abundance profiling, information of what kind of first stars at least existed in the early universe can be deduced. Demand for this kind of constraint has been increasing to examine theoretically estimated characteristics of first stars. Recent simulations estimate that first stars will show a wide initial mass distribution of $\sim$ 10–1000 $M_\odot$ (Hirano et al., 2014, 2015; Susa et al., 2014). Besides, first stars are suggested to have a fast rotation velocity at their birth (Stacy et al., 2011, 2013).

Theoretical calculations are done by the stellar evolution code and the hydrodynamic code. Descriptions of these codes and discussions on the input physics are given in Chapter 2.

In order to infer progenitor's properties from abundance comparisons, one needs to know how characteristic chemical signatures are resulted from the specific progenitor in advance. Therefore, to begin with, I aim to find such characteristic nucleosynthesis patterns for Pop III core-collapse supernova (CCSN) yields in Chapter 3. I conduct evolution calculations of 12–140 $M_\odot$ progenitors, with and without taking the effects of rotation into account. The supernova yields are calculated by applying a simple but pragmatic model of the weak explosion model, which will provide suitable stellar yields for CEMP stars. In the next Chapter 4, I confirm that more massive 145–260 $M_\odot$ stars explode as pair-instability supernovae (PISNe). I conduct a systematic calculation of PISN explosions and nucleosynthesis, in order to determine characteristic abundance patterns that can be used to distinguish the PISN yields from the other.

Eventually, I conduct abundance comparisons between the theoretical yields and observations in Chapter 5. As a demonstration of the weak supernova model, I compare the theoretical yields with the three most-iron-poor stars discovered so far, to constrain the initial masses and rotational properties of source stars of the metal pollution. PISN yields are compared with a large abundance data compiled in *SAGA* database (Suda et al., 2008, 2011; Yamada et al., 2013). I try to find candidates of PISN children from the large sample, and validate the applicability of characteristic abundance patterns proposed in Chapter 4 for efficient search.

Summary and conclusion, as well as a short discussion on future prospects, are presented in Chapter 6.

Chapter 2

Computational methods

2.1 Abundance references

The primordial abundance by Steigman (2007) is adopted for stellar evolution calculations. As the reference of the solar composition, the elemental abundance ratio by Asplund et al. (2009) and the isotopic ratio by Lodders et al. (2009) are used.

2.2 Stellar evolution code

A hydrostatic evolution of a spherical gas object, which is confined by the self-gravity, is calculated by the stellar evolution code. The energy of the star is continually radiated by photon radiation at the surface and by neutrino emission at the central region. The lost energy is compensated by nuclear reactions, and the supplied energy is redistributed among the stellar matter by energy transfer. A star reaches a thermally equilibrating phase when the energy loss and the energy supply balances. During the phase, composition change by nuclear reactions slowly modifies the stellar structure. When the equilibrium breaks, the star contracts, increasing the inner temperature until the next nuclear burning takes place.

The stellar evolution code solves the equations of stellar structure together with the nuclear reactions occurring inside the star. Because of the slow evolution compared to the hydrodynamic time, the structure equations forms a system of hyperbolic partial differential equations. Therefore, the evolution code iteratively solves the structure equations by a time-implicit manner, so-called the *Henyey method*[1]. Also, the code adopts the Lagrangian coordinate system, in which the radial mesh moves with time, tracing the movement of the fluid. The Lagrangian coordinate has a merit to numerically ensure the conservation of chemical species.

The stellar structure and the chemical distribution are split in time integration. The equations of stellar structure have four dependent variables, the radius r, the luminosity L, the pressure p, and the temperature T, which are defined at the mass coordinate M. The evolution of the chemical distribution is further split into the

---

[1]The method can actually be formulated as a Newton-Raphson's scheme solved by a block-tridiagonal matrix method.

reaction equation and the transfer equation, in which a dependent variable of Y_i, the number fractions of chemical species, is treated. Stellar structure with given chemical distribution is solved at first, then, according to the solution of the stellar structure, the evolution of the chemical distribution is calculated.

2.2.1 Basic equations: Equations of stellar structure

Basic equations of stellar structure are obtained from equations of hydrodynamics with self-gravity and energy transfer:

$$\left(\frac{\partial}{\partial t} + (\vec{v} \cdot \nabla)\right)\vec{v} = -\frac{1}{\rho}\nabla p - \nabla \phi \tag{2.1}$$

$$\left(\frac{\partial}{\partial t} + (\vec{v} \cdot \nabla)\right)e = -p\left(\frac{\partial}{\partial t} + (\vec{v} \cdot \nabla)\right)\left(\frac{1}{\rho}\right) - \frac{1}{\rho}(\nabla \cdot \vec{\theta}) + \epsilon \tag{2.2}$$

$$\nabla^2 \phi = 4\pi G\rho \tag{2.3}$$

$$\frac{\partial \rho}{\partial t} + \nabla \cdot (\rho\vec{v}) = 0 \tag{2.4}$$

$$\vec{\theta} = \text{(energy flux)}, \tag{2.5}$$

where p, ρ, e, $\vec{v}$ are the pressure, the density, the internal energy, and the velocity of the fluid, ϕ is the gravitational potential, $\vec{\theta}$ and ϵ are the energy flux and the energy source term, respectively. The first equation is the Euler equation of the flow, the second is the energy conservation law, the third is the Poisson equation, the fourth is the continuity equation, and the last shows an governing equation of the energy flux. Under the assumption of the spherical symmetry of the object, these equations reduce to

$$\frac{Dv}{Dt} = -\frac{1}{\rho}\frac{\partial p}{\partial r} - \frac{\partial \phi}{\partial r} \tag{2.6}$$

$$\frac{De}{Dt} = -p\frac{D(1/\rho)}{Dt} - \frac{1}{\rho}\left(\frac{1}{4\pi r^2}\frac{\partial}{\partial r}(4\pi r^2\theta)\right) + \epsilon \tag{2.7}$$

$$4\pi G\rho = \frac{1}{r^2}\frac{\partial}{\partial r}\left(r^2\frac{\partial \phi}{\partial r}\right) \tag{2.8}$$

$$0 = \frac{\partial \rho}{\partial t} + \frac{1}{r^2}\frac{\partial}{\partial r}\left(r^2\rho v\right) \tag{2.9}$$

$$4\pi r^2\theta = \text{(luminosity)}, \tag{2.10}$$

here, the derivative $D/Dt \equiv (\partial/\partial t) + v(\partial/\partial r)$ is used.

The enclosed mass is then defined as a function of time and radius,

$$M(t,r) \equiv \int_0^r 4\pi r^2\rho dr. \tag{2.11}$$

The enclosed mass has several merit to be handled. Firstly, since the gravity, $-\partial\phi/\partial r$, should be zero at the center of the spherical potential, it gives the first integral of the Poisson equation,

$$\frac{\partial \phi}{\partial r} = \frac{GM}{r^2}. \tag{2.12}$$

9

Moreover, the basic equations are further reduced by the variable transformation from (t, r) to (t, M). With the help of the continuity equation, the partial derivatives of $M(t, r)$ becomes

$$\frac{\partial M}{\partial t} = -4\pi r^2 \rho v \tag{2.13}$$

$$\frac{\partial M}{\partial r} = 4\pi r^2 \rho, \tag{2.14}$$

and thus the variable transformation is done with

$$\left.\frac{\partial}{\partial t}\right|_r + v\left.\frac{\partial}{\partial r}\right|_t \rightarrow \left.\frac{\partial}{\partial t}\right|_M \tag{2.15}$$

$$\frac{1}{4\pi r^2 \rho}\left.\frac{\partial}{\partial r}\right|_t \rightarrow \left.\frac{\partial}{\partial M}\right|_t. \tag{2.16}$$

According to this variable transformation, time derivative of $r(t, M)$ equates with v. This fact shows that the co-moving frame with the flow, which is called the Lagrangian coordinate, is realized by taking the (t, M) coordinate. Hereafter, the partial derivatives are taken under the Lagrangian (t, M) expression.

The basic equations of stellar structure can be summarized as;

1. Definition of the enclosed mass, or the mass coordinate:

$$\frac{\partial r}{\partial M} = \frac{1}{4\pi r^2 \rho}, \tag{2.17}$$

2. Velocity equation:

$$v = \frac{\partial r}{\partial t}, \tag{2.18}$$

3. Hydrostatic equation:

$$\frac{\partial p}{\partial M} = -\frac{GM}{4\pi r^4} + \frac{1}{4\pi r^2}\frac{\partial v}{\partial t}, \tag{2.19}$$

4. Energy equation:

$$\frac{\partial e}{\partial t} = -p\frac{\partial(1/\rho)}{\partial t} - \frac{\partial L}{\partial M} + \epsilon, \tag{2.20}$$

5. Equation of the luminosity,

$$L = L_{\mathrm{rad}} + L_{\mathrm{conv}}. \tag{2.21}$$

The effect of the so-called inertia term, the last term in the hydrostatic equation, is only effective when the timescale of the evolution gets short enough.

The basic equations require four boundary conditions for closure. At the center of the star, equations

$$r|_{M=0} = 0 \tag{2.22}$$
$$L|_{M=0} = 0 \tag{2.23}$$

are imposed, and at the surface of the star,

$$p|_{\mathrm{surface}} = \frac{GM}{\kappa r^2}\tau_s \tag{2.24}$$
$$L|_{\mathrm{surface}} = 4\pi r^2 \sigma T^4 \tag{2.25}$$

are solved, where κ, σ, and τ_s are the opacity at the surface, the Stefan-Boltzman constant, and the surface optical depth, which is an $\sim O(1)$ parameter typically set to be $2/3$, respectively.

2.2.2 Basic equations: Equation of chemical distribution

The basic equation of chemical distribution is written as

$$\frac{\partial Y_i}{\partial t} = \dot{Y}_i - \frac{\partial J_i}{\partial M} \tag{2.26}$$
$$J_i = -(4\pi r^2 \rho)^2 D_{\mathrm{eff}} \frac{\partial Y_i}{\partial M}, \tag{2.27}$$

where Y_i is the number fraction of species i, $\dot{Y}_i$ is the source term showing the effects of nuclear reactions, J_i is the flux integrated over the surface of r, and D_{eff} is the effective diffusion coefficient. A straightforward derivation of the governing equation of chemical distribution is difficult, since it includes an ad-hoc transfer term.

In the code, the time integration is firstly done for the nuclear reactions. The nuclear reaction network,

$$\frac{\partial Y_i}{\partial t} = \dot{Y}_i(T, \rho, Y_j) \tag{2.28}$$
$$= -\lambda_{i \to j} Y_i + \lambda_{j \to i} Y_j - \sum_{j,k} \lambda_{ij \to k} Y_i Y_j + \sum_{j,k} \lambda_{jk \to i} Y_j Y_k \cdots, \tag{2.29}$$

where λ's represent the reaction rates, is solved by the Newton-Raphson method. While the same module is used for the iteration (Yoshida & Umeda, 2011; Umeda et al., 2012), different number of isotopes, and thus of reactions, are set depending on calculations. In this work, 260 isotopes in the evolution calculations, 153 in the explosion calculations, and 300 in the post-process calculations are considered (Tab. 2.1). Reaction rates used in the network calculation are summarized in Tab. 2.2. Besides them, electron screening formulae are collected from Graboske et al. (1973) for the weak and intermediate screening and from Itoh et al. (1990) for the strong screening.

Table 2.1: Isotopes in the nuclear reaction network

Element	A			Element	A		
n	1	1	1	Ar	33–42	34–40	34–43
H	1–3	1–3	1–3	K	36–43	37–41	36–45
He	3–4	3–4	3–4	Ca	37–48	38–43	38–48
Li	6–7	6–7	6–7	Sc	40–49	41–45	40–49
Be	7–9	7–9	7–9	Ti	41–51	43–48	42–51
B	8–11	8–11	8–11	V	44–52	45–51	44–53
C	11–14	12–13	11–16	Cr	46–55	47–54	46–55
N	12–15	13–15	13–18	Mn	48–56	49–55	48–57
O	13–20	14–18	14–20	Fe	50–61	51–58	50–61
F	17–21	17–19	17–22	Co	54–62	53–59	51–62
Ne	18–24	18–22	18–24	Ni	56–66	55–62	54–66
Na	20–25	21–23	21–26	Cu	59–67	57–63	56–68
Mg	21–27	22–26	22–28	Zn	62–70	60–64	59–71
Al	23–29	25–27	25–30	Ga	65–73	—	61–73
Si	24–32	26–32	26–32	Ge	69–76	—	63–75
P	27–34	29–33	27–34	As	71–77	—	65–76
S	29–36	30–36	30–37	Se	73–79	—	67–78
Cl	31–38	33-37	32–38	Br	76–80	—	69–79

Notes. Isotopes included in the nuclear reaction network for stellar evolution calculations (260 isotopes, left), for explosion calculations (153 isotopes, middle), and for post processing calculations (300 isotopes, right).

Then the rest is solved as a diffusion equation,

$$\frac{\partial Y_i}{\partial t} = \frac{\partial}{\partial M}\left((4\pi r^2 \rho)^2 D_{\mathrm{eff}} \frac{\partial Y_i}{\partial M}\right). \tag{2.30}$$

The effective diffusion coefficient consists of the convective component and the component of rotationally induced mixing,

$$D_{\mathrm{eff}} = D_{\mathrm{conv}} + D_{\mathrm{rot}}. \tag{2.31}$$

How to determine the two components are described later.

2.2.3 Input physics

The equation of states of the stellar matter consists of four species of particles, photon, nuclei, electron, and positron, which share the same equilibrating temperature. Photon is expressed as a black body radiation, nuclei are approximated as ideal gases that obey the Maxwell-Boltzmann statistics, and Electron and positron are expressed as ideal Fermi gases (Blinnikov et al., 1996). The emergence of positron is governed by the equation,

$$0 = \mu_{e^-} + \mu_{e^+}, \tag{2.32}$$

which shows the reaction equilibrium between electron-positron pair and the blackbody radiation. The free energy of the matter is firstly defined as

$$F(T, V, N_i) = F_{\mathrm{ph}} + F_{\mathrm{nuc}} + F_{\mathrm{e^-}} + F_{\mathrm{e^+}} + F_{\mathrm{coul}}, \tag{2.33}$$

Table 2.2: References of reaction rates

		reference
Mass excess		Audi (2003)
Thermonuclear reaction rate and thermal enhancement factor		JINA Reaclib (Cyburt et al., 2010)
Weak interaction rate	(A = 17–39)	Oda et al. (1994)
	(A = 23, 25, 27)	Toki et al. (2013)
	(A = 40–44)	Fuller et al. (1982)
	(A = 45–65)	Langanke & Martínez-Pinedo (2001)
	(A > 65)	Takahashi & Yokoi (1987)
	(others)	Horiguchi et al. (2000)

in which F_{ph}, F_{nuc}, F_{e^-}, F_{e^+} are the free energies of photon, nuclei, electron, and positron, respectively, and F_{coul} is the free energy of the Coulomb interaction (Salpeter & van Horn, 1969; Slattery et al., 1982). Then other thermodynamic quantities are defined as derivatives of the free energy,

$$S = \left(\frac{\partial F}{\partial T}\right)_{V,N_i} \tag{2.34}$$

$$p = \left(\frac{\partial F}{\partial V}\right)_{T,N_i} \tag{2.35}$$

$$\mu_i = \left(\frac{\partial F}{\partial N_i}\right)_{T,V,N_j}, \tag{2.36}$$

or as a result of the Legendre transformation for the internal energy,

$$U = F - TS. \tag{2.37}$$

In the stellar calculation, the specific forms of the thermodynamic quantities, $s \equiv S/M_b$, $e \equiv U/M_b$, p, and μ_i are directly calculated and used as functions of the density, the temperature, and the composition, where $M_b \equiv m_u N_b$ is the baryon mass in the region of V (see Appendix A).

The energy source term, ϵ, is further divided into the energy generation term by nuclear reactions, ϵ_{nuc}, and the energy loss term by neutrino emission, ϵ_ν. Equating with the first law of the thermodynamics,

$$de = -pd\left(\frac{1}{\rho}\right) + Tds + \frac{1}{m_u}\sum_i \mu_i dY_i, \tag{2.38}$$

which is directly derived for the free-energy-based equation of states, the energy equation is further modified into the entropy equation,

$$T\frac{\partial s}{\partial t} = -\frac{\partial L}{\partial M} - \frac{1}{m_u}\left[\sum_{\mathrm{nuclei}} \mu_i \dot{Y}_i + \mu_e \dot{Y}_e\right] - \epsilon_\nu, \tag{2.39}$$

where μ_i and μ_e are the special-relativistic chemical potentials including the rest masses for nuclei and electron. One may define ϵ_{nuc} as

$$\epsilon_{\mathrm{nuc}} = -\frac{1}{m_u}\left[\sum_{\mathrm{nuclei}} \mu_i \dot{Y}_i + \mu_e \dot{Y}_e\right] \tag{2.40}$$

13

in this entropy equation. The thermal contribution of the neutrino cooling rate is calculated according to Itoh et al. (1989, 1996), which includes pair, photo-, plasma, and bremsstrahlung processes. In addition to those thermal neutrinos, neutrinos emitted by weak nuclear reactions, such as electron captures and beta decays, also composes ϵ_ν.

One important input physics in the stellar code is the opacity of the matter. Since stellar matter, except near the surface, is in the radiative equilibrium, the Rosseland mean opacity

$$\frac{1}{\kappa} \equiv \frac{\int_0^\infty \kappa_\nu^{-1} u_\nu d\nu}{\int_0^\infty u_\nu d\nu} \tag{2.41}$$

is useful to be used in the simulation. Using the mean opacity, the radiative luminosity can be determined as

$$L_{\rm rad} = \frac{\frac{4}{3}aT^4}{p} \frac{4\pi cGM}{\kappa} \frac{d{\rm log}T}{d{\rm log}P}. \tag{2.42}$$

We utilize the tabulated opacity data by the *OPAL* project (Iglesias & Rogers, 1996) together with the conductive opacity by Potekhin et al. (2006) and the molecular opacity by Ferguson et al. (2005).

Convection is assumed to take place in a dynamically unstable region of

$$\nabla_{\rm rad} > \nabla_{\rm ad} + \frac{\varphi}{\delta}\nabla_\mu, \tag{2.43}$$

where $\varphi \equiv (\partial{\rm ln}\rho/\partial{\rm ln}\mu)$ and $\delta \equiv -(\partial{\rm ln}\rho/\partial{\rm ln}T)$ are thermodynamic functions, $\nabla_\mu \equiv d\log\mu/d\log p$ is the μ-gradient, and $\nabla_{\rm rad}$ and $\nabla_{\rm ad}$ are the radiative and adiabatic temperature gradients. In the convective region, the convective luminosity, $L_{\rm conv}$, is calculated according to the mixing length theory (Böhm-Vitense, 1958), otherwise it is set to be zero. The velocity of the convective blob, $v_{\rm conv}$, and the mixing length, $l_{\rm mix} \equiv \alpha_{\rm mix}H_p$, are used to estimate the diffusion coefficient by convection,

$$D_{\rm conv} = \frac{1}{3}v_{\rm conv}l_{\rm mix}. \tag{2.44}$$

In addition, overshooting of the convective motion from the edge of the dynamically unstable regions is treated during core hydrogen and core helium burning phases. An exponentially decaying formula,

$$D_{\rm conv,ov} = D_{\rm conv,0}{\rm exp}\left(-2\frac{\Delta r}{f_{\rm ov}H_{p,0}}\right) \tag{2.45}$$

is applied, where $f_{\rm ov}$ is an adjustable parameter, $D_{\rm conv,0}$ and $H_{p,0}$ are the convective mixing coefficient and the pressure height at the edge of the convective region, and Δr is a distance from the edge. Finally, the vibrational instability is assumed to grow in a region of

$$\nabla_{\rm ad} + \frac{\varphi}{\delta}\nabla_\mu \geq \nabla_{\rm rad} > \nabla_{\rm ad}. \tag{2.46}$$

Mixing by the instability is treated by applying a diffusion coefficient of Spruit (1992) with a parameter of f_{sc}=0.3.

Although wind mass loss constitutes a highly influential input physics in evolution of a massive metal-rich star, I apply a small constant mass loss rate of $\dot{M} = 10^{-14}$ $M_\odot$ yr^{-1} for metal-free calculations. This reflects the fact that the surface of a metal-free star is lacking a photon absorber, such as iron ions, which account for the wind acceleration of hot metal-rich stars. Owing to the small rate, mass loss in the metal-free models presented in this work is practically negligible, unless mechanical mass loss by fast rotation sets in. However, still many possibilities exist concerning the mass loss rate of massive stars. There is a discussion that light elements synthesized in an early stage of the stellar life may be mixed up to the surface and contribute to the wind acceleration (Meynet et al., 2006; Ekström et al., 2008). Photon absorption by CNO elements might be of the prime importance to be investigated, but calculation by Krtička & Kubát (2009) in this case shows that they are not enough to drive an effective wind mass loss. Pulsational mass loss (Baraffe et al., 2001; Sonoi & Umeda, 2012; Moriya & Langer, 2015) may account for the mass loss in the metal-less environment. Moreover, as the mechanism of red giant mass loss has not been determined yet even for metal-rich stars, there is no grounds to omit the red giant mass loss for metal-free models. The assumption of no mass loss for metal-free models, thus, should be regarded as one extreme possibility to be investigated.

2.2.4 Stellar rotation

Stellar rotation can be modeled as a large-scale steady flow circulating around the rotation axis. It is, thus, fundamentally a multi-dimensional phenomenon, the description of which requires at least axially symmetric equations. However, although there are some efforts to conduct a two-dimensional calculation incorporating the evolution of flows in the meridional plane (e.g., Deupree, 1990; Espinosa Lara & Rieutord, 2007; Yasutake et al., 2015), simulating the full evolution is still a computationally unreachable task. One possibility is to somehow subtract a one-dimensional relation from the multi-dimensional problem, and expresses the meridional flow as an effective transfer phenomenon between the one-dimensional regions.

For example, if the rotational flow is a potential flow, i.e., the angular velocity of the flow only depends on the distance from the rotation axis, the constant pressure surface coincides with the constant density surface (e.g. Eriguchi & Mueller, 1985). In this case, the pressure structure can be described by a one-dimensional equation (Kippenhahn & Thomas, 1970). Similar type of a one-dimensional pressure equation can be formulated, if the angular velocity of the rotational flow becomes constant on the isobar (Meynet & Maeder, 1997). This so-called shellular rotation law is firstly introduced by Zahn (1992) as a result of the effective angular momentum transfer by the hypothetical horizontal turbulence, and it constitutes the most fundamental assumption in modern 1D evolution codes for calculating the evolution of a rotating star (e.g., Meynet & Maeder, 2000; Heger et al., 2000; Yoon & Langer, 2005; Chieffi & Limongi, 2013; Paxton et al., 2013; Takahashi

et al., 2014).

Three effects of stellar rotation are incorporated in our code.

1. Due to the centrifugal force, the star is deformed and the pressure balance is changed.

2. Chemical composition is mixed owing to the meridional circulation and the meridional turbulence driven by rotational instabilities.

3. The surface material is easier to be ejected with the help of the centrifugal force.

Those effects are respectively taken into account in the equations of pressure and temperature gradients, in the diffusion equation of chemical species, and in the formula of the mass loss.

At first, definitions of the mass coordinate and the radius are extended. The mass coordinate, M_p, is defined as the enclosed mass inside the isobar of the pressure p. Accordingly, the radius, r_p, is defined as the effective radius of the volume inside the isobar, $V_p \equiv 4\pi r_p^3/3$. Due to the centrifugal force, the constant pressure surface is assumed to form a spheroid of

$$r(\cos\theta) = a[1 - \epsilon P_2(\cos\theta)], \tag{2.47}$$

in which P_2 is the second-order Legendre polynomial (Denissenkov & VandenBerg, 2003). The scaling radius a and the degree of rotation ϵ are related to r_p as

$$r_p = a\left(1 + \frac{3}{5}\epsilon^2 - \frac{2}{35}\epsilon^3\right)^{1/3}, \tag{2.48}$$

$$\epsilon = \frac{\omega_p^2 r_p^3}{3GM_p}\left(\frac{a}{r_p}\right)^3, \tag{2.49}$$

where ω_p is the angular velocity of the isobar.

The equations of pressure balance and radiative luminosity are modified as

$$\frac{\partial p}{\partial M_p} = -\frac{GM_p}{4\pi r_p^4}f_p, \tag{2.50}$$

$$L_{\rm rad} = \frac{\frac{4}{3}aT^4}{p}\frac{4\pi cGM_p}{\kappa}\frac{d\log T}{d\log p}\frac{f_p}{f_T}. \tag{2.51}$$

Modification factors, f_p and f_T, are calculated as

$$f_p = \frac{4\pi r_p^4}{GM_p S_p}\frac{1}{\langle g_{\rm eff}^{-1}\rangle} \tag{2.52}$$

$$f_T = \left(\frac{4\pi r_p^2}{S_p}\right)^2\frac{1}{\langle g_{\rm eff}\rangle\langle g_{\rm eff}^{-1}\rangle}, \tag{2.53}$$

where S_p is the surface area of the isobar, and $\langle\rangle$ represents the averaged quantity,

$$\langle q\rangle = \frac{1}{S_P}\int_{\rm isobar} qd\sigma. \tag{2.54}$$

16

In the calculation of $\langle g_{\mathrm{eff}} \rangle$, the norm is calculated from

$$g_{\mathrm{eff,r}} = \frac{\partial \phi}{\partial r} + \omega_p^2 r \sin^2 \theta \qquad (2.55)$$

$$g_{\mathrm{eff},\theta} = \frac{1}{r}\frac{\partial \phi}{\partial \theta} + \omega_p^2 r \sin \theta \cos \theta, \qquad (2.56)$$

with the Roche approximation for the gravity,

$$\frac{\partial \phi}{\partial r} = -\frac{GM_p}{r_p^2} \qquad (2.57)$$

$$\frac{1}{r}\frac{\partial \phi}{\partial \theta} = 0. \qquad (2.58)$$

Several instabilities, as well as meridional circulation, constitute the coefficient of the rotationally induced mixing (Endal & Sofia, 1978; Pinsonneault et al., 1989; Heger et al., 2000, 2005):

$$D_{\mathrm{rot}} = f_{\mathrm{c}} \times (\nu_{\mathrm{ES}} + \nu_{\mathrm{GSF}} + \nu_{\mathrm{SH}} + \nu_{\mathrm{DS}} + \nu_{\mathrm{SS}}) + D_{\mathrm{TS}}. \qquad (2.59)$$

The considered instabilities are meridional circulation (also known as the Eddington-Sweet circulation), the Goldreich-Schubert-Fricke instability, the Solberg-Høiland instability, the dynamical and secular shear instabilities, and the Tayler-Spruit dynamo (Spruit, 2002). According to Heger et al. (2000), corresponding viscosities are estimated as ν_{ES}, ν_{GSF}, ν_{SH}, ν_{DS}, and ν_{SS}, and summed up using a free parameter f_{c}. This parameter f_{c} accounts for the possible difference between the efficiencies of angular momentum transport and matter mixing. In addition, diffusion coefficient by the Tayler-Spruit dynamo D_{TS} is added.

For instance, the way to calculate the viscosity of the meridional circulation is shown. Firstly, typical velocities of meridional circulation and μ-currents, by which the meridional circulation is stabilized, are calculated (Kippenhahn & Moellenhoff, 1974; Kippenhahn, 1974),

$$v_e = \frac{1}{g\delta}\frac{\nabla_{\mathrm{ad}}}{\nabla_{\mathrm{ad}} - \nabla}\left(\frac{\omega^2 r^3}{GM}\right)\frac{L}{M}\left[\frac{2M(\epsilon_{\mathrm{nuc}} - \epsilon_\nu)}{L} - 2 - \frac{M}{4\pi\rho r^3/3}\right] \qquad (2.60)$$

$$v_\mu = f_\mu \frac{\frac{\varphi}{\delta}\nabla_\mu}{\nabla_{\mathrm{ad}} - \nabla}\frac{H_p}{\tau_{\mathrm{KH}}^\star}, \qquad (2.61)$$

in which f_μ is another free parameter that shows the reduction efficiency of the μ-barrier, and $\tau_{KH}^\star \equiv \frac{GM^2}{r(L+M\epsilon_\nu)}$ is the local Kelvin-Helmholtz timescale. Next, the effective circulation velocity is defined as the difference between the absolute values of the two velocities. Only if the effective velocity becomes positive, the rotationally induced mixing is assumed to take place by the meridional circulation. Thus, using the effective circulation velocity, $v_{\mathrm{ES}} = \max[|v_e| - |v_\mu|, 0]$, and the length scale of meridional circulation l_{ES}, the viscosity is estimated as

$$\nu_{\mathrm{ES}} = v_{\mathrm{ES}}l_{\mathrm{ES}}. \qquad (2.62)$$

Note that we use the pressure scale hight as the trial length scale of meridional circulation,

$$l_{\mathrm{ES}} = H_p, \tag{2.63}$$

rather than more complicated definitions in literature (e.g. Endal & Sofia, 1978). This is because the computational cost is much less but calculated results by adopting either definitions are quite similar.

Similar to matter mixing, the angular momentum transport is expressed by a diffusion equation (Pinsonneault et al., 1989):

$$\frac{\partial \omega}{\partial t} = \frac{1}{I} \frac{\partial}{\partial M} \left((4\pi r^2 \rho)^2 I \nu_{\mathrm{eff}} \frac{\partial \omega}{\partial M} \right) - \frac{\omega}{r} \left(\frac{\partial r}{\partial t} \right) \left(\frac{\partial \ln I}{\partial \ln r} \right), \tag{2.64}$$

in which I and ν_{eff} are, respectively, the specific moment of inertia and the effective viscosity. The first term in the r.h.s. represents the angular momentum transport by matter mixing, and the second term emerges from the local angular momentum conservation (Heger et al., 2000). For the effective viscosity, all the viscosities listed above are summed up:

$$\nu_{\mathrm{eff}} = \nu_{\mathrm{ES}} + \nu_{\mathrm{GSF}} + \nu_{\mathrm{SH}} + \nu_{\mathrm{DS}} + \nu_{\mathrm{SS}} + \nu_{\mathrm{TS}}. \tag{2.65}$$

The last effect of stellar rotation is the rotationally induced enhancement of mass loss (the $\Omega\Gamma$-limit, Langer, 1998; Maeder & Meynet, 2000; Kudritzki, 2002). According to Yoon et al. (2010, 2012), the enhancement of the mass loss rate is calculated as

$$\dot{M} = -\min\left[|\dot{M}(v_{rot} = 0)| \times \left(1 - \frac{v_{\mathrm{rot}}}{v_{\mathrm{crit}}} \right)^{-0.43}, 0.3 \frac{M}{\tau_{\mathrm{KH}}} \right], \tag{2.66}$$

where $v_{\mathrm{crit}} = \sqrt{GM(1 - \frac{L}{L_{\mathrm{Edd}}})/R}$ is the critical rotation velocity at the surface of the star, L_{Edd} is the Eddington luminosity, and τ_{KH} is the Kelvin-Helmholtz timescale.

2.2.5 Calibration of the code

The same calibration to the recent grids calculations with *GENEC* has been done (Ekström et al., 2012; Georgy et al., 2012, 2013). A solar-metallicity 15 M$_\odot$ star rotating with ~ 200 km s^{-1} during main sequence has been specified as the reference model. Two observational constraints are used. The first is the main sequence width in the HR diagram. The second is the surface nitrogen enhancement during main sequence, which is set to be in the range from $+0.5$ to $+0.7$ at the terminal-age main sequence (TAMS) phase (Gies & Lambert, 1992; Morel et al., 2008; Hunter et al., 2009).

Taking the constant $f_{\mathrm{c}} = 1/24$, the overshoot parameter, f_{ov}, and the parameter showing the reduction efficiency of μ-barrier, f_{μ} are calibrated. Effective temperature decreases by increasing f_{ov}, and both effective temperature and [N/H] increases by decreasing f_{μ}, thus by increasing the efficiency of rotation induced mixing. The evolution of surface quantities are shown in Fig.2.1. According to the calibration, two parameters are specified as $f_{\mu} = 0.015$ and $f_{\mathrm{ov}} = 0.07$.
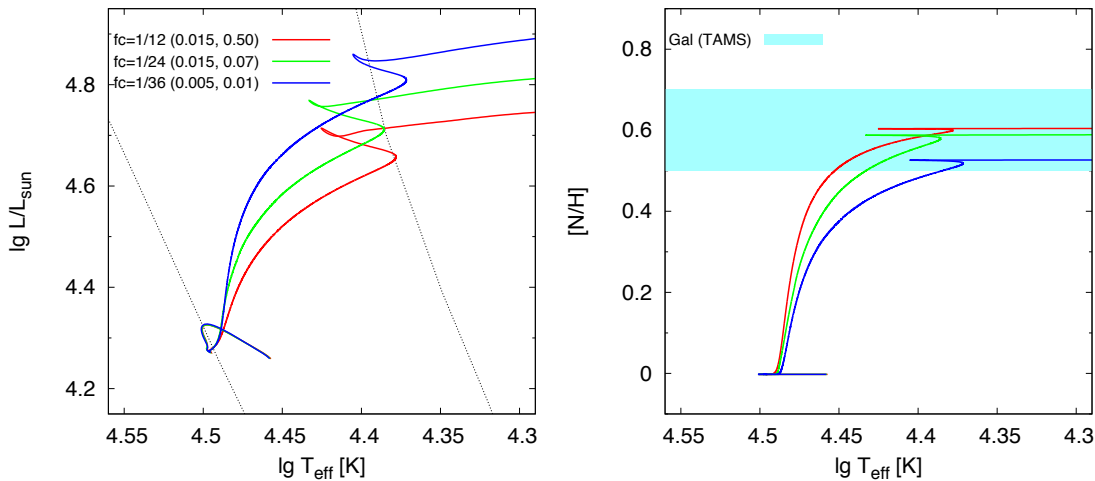
Figure 2.1: HR diagram (left) and [N/H] vs effective temperature diagram (right) for 15 M$_\odot$ models. Dotted lines in the HR diagram show the observed width of massive main sequence stars in our Galaxy (Ekström, 2015, private communication). Parameter sets applied for the calculations are shown in the legends as (f_μ, f_{ov}).

2.3 Hydrodynamic code

I utilize a 1D-spherical general-relativistic Lagrangian hydrodynamic code developed by Yamada (1997) for hydrodynamic simulations. The code integrates the time in an implicit manner, iteratively solving equations of the metric and the hydrodynamics. As the code had originally been developed to simulate evolution of very inner region of a collapsing core, I introduce some input physics for more general purpose simulations. They are the reaction network and the non-NSE EOS, which are imported from the stellar evolution code. Although the hydrodynamic code is capable directly solving the Boltzmann equation for the neutrino transfer (Yamada et al., 1999; Sumiyoshi et al., 2000), the thermal neutrino energy loss rate, which is also imported from the stellar evolution code, is locally estimated in the work presented here without treating the complicated neutrino transfer.

2.3.1 Basic equations

According to Misner & Sharp (1964), a Lagrangian spherical metric is applied in the code:

$$ds^2 = e^{2\phi}dt^2 - e^{2\lambda}\Big(\frac{G}{c^2}\Big)^2 dm^2 - r^2(d\theta^2 + \sin^2\theta d\varphi^2), \qquad (2.67)$$

where the metric is identified by functions of $\phi(t,m)$, $\lambda(t,m)$, and $r(t,m)$. The gravitational constant, G, and the speed of light, c, are taken to be unity in the

following equations. The energy-momentum tensor, $T^{\mu\nu}$, of the fluid is written as

$$T^{\mu\nu} = [\rho_b(1 + \epsilon) + p]u^\mu u^\nu - pg^{\mu\nu}, \tag{2.68}$$

where $g^{\mu\nu}$ is the inverse of the metric tensor $g_{\mu\nu}$. As the metric is designed to be a co-moving frame of the fluid, the 4-velocity of the fluid u^μ becomes $u^t = e^{-\phi}$ and $u^i = 0$ ($i = r, \theta, \varphi$). The baryon mass density of the fluid, ρ_b, relates with the baryon number density, n_b, as

$$\rho_b = m_u n_b. \tag{2.69}$$

The basic equations of the system are obtained from the baryon number conservation

$$\nabla_\mu(n_b u^\mu) = 0, \tag{2.70}$$

the energy and momentum conservation

$$\nabla_\mu T^{\mu\nu} = 0, \tag{2.71}$$

and the Einstein equation

$$G^{\mu\nu} = 8\pi T^{\mu\nu}, \tag{2.72}$$

where $G^{\mu\nu}$ is the Einstein tensor. Not all of them are actually independent. Together with the equation of states, they are used to describe the evolution of the six dependent variables, ϕ, λ, r, ρ_b, p, and ϵ, thus five independent equations are to be deduced.

First, from the energy and momentum conservation, two equations are obtained;

$$e^{-\phi}\frac{\partial \epsilon}{\partial t} = -e^{-\phi}p\frac{\partial \tau}{\partial t} \tag{2.73}$$

$$h\frac{\partial \phi}{\partial m} = -\tau\frac{\partial p}{\partial m}, \tag{2.74}$$

in which $\tau \equiv 1/\rho_b$ and $h \equiv 1 + \epsilon + p\tau$ are the specific volume and the specific enthalpy of the fluid, respectively. The first equation shows the first law of thermodynamics, and the second is the Euler equation of the flow. Then, metric equations are obtained from the Einstein equation as

$$e^{-\phi}\frac{\partial U}{\partial t} = -\frac{\Gamma}{h}4\pi r^2\frac{\partial p}{\partial m} - \frac{\tilde{m}}{r^2} - 4\pi rp \tag{2.75}$$

$$\frac{\partial \tilde{m}}{\partial t} = -p\frac{\partial}{\partial t}\left(\frac{4\pi}{3}r^3\right), \tag{2.76}$$

in which new variables, the radial fluid velocity U, the gravitational mass $\tilde{m}$, and the general relativistic gamma factor Γ, are defined as

$$U = e^{-\phi}\frac{\partial r}{\partial t} \tag{2.77}$$

$$e^\lambda = \frac{1}{\Gamma}\frac{\partial r}{\partial m} \tag{2.78}$$

$$\Gamma^2 = 1 + U^2 - \frac{2\tilde{m}}{r}. \tag{2.79}$$

20

Finally, the continuity equation is obtained from the baryon number conservation,

$$e^{-\phi}\frac{\partial \tau}{\partial t} = -\frac{1}{\Gamma}\frac{\partial}{\partial m}(4\pi r^2 U). \qquad (2.80)$$

For the implicit calculations and for the better reproduction of the Rankine-Hugoniot relation, the above equations are further modified as a system of nine basic equations as

$$e^{-\phi}\frac{\partial \tau}{\partial t} = -\frac{1}{\Gamma}\frac{\partial}{\partial m}(4\pi r^2 U) \qquad (2.81)$$

$$e^{-\phi}\frac{\partial \epsilon}{\partial t} = -\frac{1}{\Gamma}\frac{\partial}{\partial m}(4\pi r^2 p U) - \frac{h}{\Gamma^2}e^{-\phi}\frac{\partial}{\partial t}\left(\frac{1}{2}U^2\right) + \frac{h}{\Gamma^2}\tilde{m}e^{-\phi}\frac{\partial}{\partial t}\left(\frac{1}{r}\right)$$

$$-\frac{h}{\Gamma^2}2\pi p e^{-\phi}\frac{\partial r^2}{\partial t} \qquad (2.82)$$

$$e^{-\phi}\frac{\partial U}{\partial t} = -\frac{\Gamma}{h}4\pi r^2\frac{\partial p}{\partial m} - \frac{\tilde{m}}{r^2} - 4\pi r p \qquad (2.83)$$

$$\frac{\partial \tilde{m}}{\partial t} = -p\frac{\partial}{\partial t}\left(\frac{4\pi}{3}r^3\right) \qquad (2.84)$$

$$h\frac{\partial \phi}{\partial m} = -\tau\frac{\partial p}{\partial m} \qquad (2.85)$$

$$\Gamma\tau = \frac{\partial(4\pi r^3/3)}{\partial m} \qquad (2.86)$$

$$h = 1 + \epsilon + p\tau \qquad (2.87)$$

$$e^{\lambda} = \frac{1}{\Gamma}\frac{\partial r}{\partial m} \qquad (2.88)$$

$$\Gamma^2 = 1 + U^2 - \frac{2\tilde{m}}{r}, \qquad (2.89)$$

which describes the evolution of the ten dependent variables of ϕ, λ, r, $\tilde{m}$, $\tau \equiv 1/\rho_b$, ϵ, p, h, U, and Γ, together with the equation of states. Note that the equation (2.86) is solved to determine r instead of the equation (2.77). All the dependent variables except r, ϕ, and $\tilde{m}$ are defined at the center of meshes, while the exceptions are defined at the cell interfaces.

2.3.2   Shock capturing method

The linearized Riemann problem is solved to determine the pressure and velocity at every cell interface. The method is a Lagrangian and general-relativistic generalization of a method in Roe (1981). Hereafter, a dependent variable defined at cell centers is denoted to have a subscript or i, instead a subscript I is used for variables defined at cell interfaces. Thus, the left and right constant states, which are characterized as (τ_L, U_L, p_L) and (τ_R, U_R, p_R), are determined by (τ_i, U_i, p_i) and $(\tau_{i+1}, U_{i+1}, p_{i+1})$, and quantities at the interface, (τ_I, U_I, p_I), are given as the solution of the evolution.

First, taking advection terms from the basic equations, an advection equation

$$\frac{\partial}{\partial t}\begin{pmatrix}\tau \\ U \\ p\end{pmatrix} = \begin{pmatrix} 0 & \frac{e^\phi}{\Gamma}4\pi r^2 & 0 \\ 0 & 0 & -\frac{e^\phi \Gamma}{h}4\pi r^2 \\ 0 & -\gamma\frac{p}{\tau}\frac{e^\phi}{\Gamma}4\pi r^2 & 0 \end{pmatrix}\frac{\partial}{\partial m}\begin{pmatrix}\tau \\ U \\ p\end{pmatrix} \tag{2.90}$$

is obtained, where

$$\gamma \equiv \left(\frac{\partial \ln p}{\partial \ln \rho_b}\right)_{ad} \tag{2.91}$$

is the adiabatic index. The Jacobian matrix has eigenvalues and eigenvectors of

$$\lambda_1 = -e^\phi 4\pi r^2 \rho_b c_s : \quad \mathbf{r}_1 = \begin{pmatrix}\tau \\ \Gamma c_s \\ -\gamma p\end{pmatrix}, \quad \mathbf{l}_1 = \begin{pmatrix}0 \\ 1/2\Gamma c_s \\ 1/2\gamma p\end{pmatrix}, \tag{2.92}$$

$$\lambda_2 = 0 : \quad \mathbf{r}_2 = \begin{pmatrix}1 \\ 0 \\ 0\end{pmatrix}, \quad \mathbf{l}_2 = \begin{pmatrix}1 \\ 0 \\ \tau/\gamma p\end{pmatrix}, \tag{2.93}$$

$$\lambda_3 = e^\phi 4\pi r^2 \rho_b c_s : \quad \mathbf{r}_3 = \begin{pmatrix}\tau \\ -\Gamma c_s \\ -\gamma p\end{pmatrix}, \quad \mathbf{l}_3 = \begin{pmatrix}0 \\ -1/2\Gamma c_s \\ -1/2\gamma p\end{pmatrix}, \tag{2.94}$$

where

$$c_s \equiv \sqrt{\gamma\frac{p}{\rho_b h}} \tag{2.95}$$

is the sound velocity. The first and the third modes correspond to the left- and right-going sound waves and the second represents the contact discontinuity, respectively.

Next, for the linearization, the Jacobian matrix is replaced by a constant matrix. In this procedure, variables are evaluated by simple arithmetic averages as $\rho_{bm} = (\rho_{bL} + \rho_{bR})/2$, $u_m = (u_L + u_R)/2$, and $\epsilon_m = (\epsilon_L + \epsilon_R)/2$, and other thermodynamic quantities are made from them using the equation state. It is known that the linearized Riemann problem is solved analytically. The solutions are

$$u_I = \frac{1}{2}(u_R + u_L) - \frac{c_{sm}}{2\gamma_m p_m}(p_R - p_L) \tag{2.96}$$

$$p_I = \frac{1}{2}(p_R + p_L) - \frac{\gamma_m p_m}{2c_{sm}}(u_R - u_L). \tag{2.97}$$

The second terms that are proportional to differences of the pressures and the velocities naturally introduce diffusion effects into the solution.

In order to achieve second order accuracy in the spacial resolution, the left and right constant states are estimated by the piecewise linear distribution. The slopes are made for variables of ρ_b, U, ϵ, and Γ as

$$S^j = \begin{cases} s_L^j & \text{for } \|s_L^j\| \le \|s_R^j\| \quad \text{and } s_L^j s_R^j > 0, \\ s_R^j & \text{for } \|s_L^j\| > \|s_R^j\| \quad \text{and } s_L^j s_R^j > 0, \\ 0 & \text{otherwise}, \end{cases} \tag{2.98}$$

where the superscript j indicates the dependent variables, and s_L and s_R denote the left- and right-hand slopes respectively. Thus the interpolated values of velocity, for example, are determined as

$$
\begin{aligned}
u_L &= U_i + S_i^U(r_I - \bar{r}_i) & (2.99) \\
u_R &= U_{i+1} + S_{i+1}^U(r_I - \bar{r}_{i+1}), & (2.100)
\end{aligned}
$$

where $\bar{r}_i \equiv \sqrt[3]{(r_{I-1}^3 + r_I^3)/2}$ is the averaged radius at the cell center.

Chapter 3

Yields of Pop III weak supernovae

In this chapter, I perform stellar evolution simulation of first stars and calculate stellar yields from the first supernovae[1].

Similar attempts have been made by a number of previous works (e.g., Umeda & Nomoto, 2002, 2005; Tominaga et al., 2007a, 2014; Heger & Woosley, 2010). Among them, Japanese researchers have shown that abundance trends seen in EMP stars can be explained by theoretical yield calculations applying a so-called mixing-fallback model (Umeda & Nomoto, 2005). The mixing-fallback model is a one-dimensional effective model which mimics the three dimensional flows, represented by mixing and fallback (Tominaga et al., 2007a). They attribute the increasing trend of [Co, Zn/Fe] with decreasing [Fe/H] to Pop III CCSNe exploding with large explosion energies (Kobayashi et al., 2006; Nomoto et al., 2013). However, properties of the progenitor star, such as the initial mass or the rotation rate, have not been constrained. The reason is that inner abundance ratios that those authors have mainly focused are similar among the massive stars in the mixing-fallback model. One representative study is done by Tominaga et al. (2014), in which abundance patterns of 48 EMP stars are fitted by the mixing-fallback model to discuss the explosion properties, using only one 25 $M_\odot$ progenitor. Heger & Woosley (2010) calculate hydrostatic and explosive nucleosynthesis by a one-dimensional hydrodynamic code, and compare the results with some EMP stars. Although their calculation fills the wide parameter ranges of the initial mass and the explosion energy, stellar rotation is not considered in this work. In addition, as they choose the "best-fit" models by running an automated fitting algorithm, it has not been investigated on what basis the initial mass of the progenitor can be constrained through the abundance profiling.

Therefore, the main purpose of this chapter is to obtain new knowledge of abundance yields of Pop III supernovae that can be used to constrain the characteristics of Pop III stars. Calculated models have a wide initial mass range of 12–140 $M_\odot$, which is a likely mass range for core-collapse supernovae. Additionally, in order to find a signature of stellar rotation, evolution of rotating stars is calculated. The supernova yields are calculated by the *weak explosion* model, which will provide appropriate abundance patterns of CEMP stars. So far, several works show that

---

[1]The evolution and yield calculations have been reported in Takahashi et al. (2014).

stellar rotation affects all results of stellar evolution (e.g., Meynet & Maeder, 2000; Heger et al., 2000). Hence stellar rotation in Pop III stars is also expected to have an important consequence on the yields. Indeed, it has been already shown that stellar rotation at small metallicities significantly affects the stellar nucleosynthesis, especially nitrogen production, which can explain a N/O plateau observed in metal poor host stars (Meynet & Maeder, 2002a,b; Chiappini et al., 2006; Hirschi, 2007; Meynet et al., 2010). Note that our calculation is limited to the case of single stellar evolutions. Fragmentation during first star formation may result in a high fraction of binaries and/or multiple systems, and the binarity could affect the evolution and thus the nucleosynthesis results of the first stars (e.g., Stacy & Bromm, 2013). Effects of binarity will be investigated in the future.

3.1 Computational settings

3.1.1 Stellar evolution calculation

Stellar evolution of 24 progenitor models is calculated for a wide initial parameter range. Metallicity is set to be zero, and two initial parameters are used to specify the progenitor. The first one is the initial mass of the model, which is taken from 12 $M_\odot$ to 140 $M_\odot$. The wide range covers the likely initial mass for core-collapse supernovae to take place. The next one is the initial rotation. For a rotating model, initial rotation is set to be a uniform rotation with a moderate velocity of $v_{\rm rot}/v_{\rm k} \sim 0.15$ at its ZAMS, where $v_{\rm k} \equiv \sqrt{GM/R}$ is the Keplerian velocity at the surface. These massive first stars have surface rotation velocities of $\sim$ 200–300 km sec^{-1} at their ZAMS phase, which is comparable to rotation speeds of observed OB stars (e.g., for our Galaxy, Fukuda 1982, and for LMC and SMC, Hunter et al. 2008). More slowly rotating models of half- and quarter-rotation are additionally calculated for 20, 30, and 40 $M_\odot$ cases.

Stellar evolution calculations are followed from deuterium burning phases until central temperatures reach 10^{10} K during the last collapse. Calculated models are summarized in Table 3.1. The mass of the iron core, $M_{\rm Fe}$, is defined as the mass coordinate of the local peak of energy generation by silicon burning. The CO core mass $M_{\rm CO}$, or mass of the base of a helium layer, is taken to be the mass coordinate at which the mass fraction of helium reaches 0.1. Similarly, the top of the helium layer, $M_{\rm CO} + \Delta M_{\rm He}$, is defined as the mass coordinate where the mass fraction of hydrogen becomes 0.01.

Although there have been a lot of works on the structure of rotating stars, how to construct a proper model is still under debate. Internal mixing in a rotating star will be the most influential physics for the evolution, but precise treatment of rotational mixing is difficult so far. This is why we basically take only one rotating model for each mass in the calculation, except for the additional 20–40 $M_\odot$ models. The presented rotating models show varieties of nucleosynthesis due to efficient internal mixing. Our rotating models can thus be regarded as the representative results of efficient internal mixing by rotation.

Finally, let me note here that no arguments has been known for the justification

Table 3.1: Properties of massive Pop III models

M_{ini}	M_{fin}	v_{rot}	v_{rot}/v_k	τ_H	τ_{fin}	M_{Fe}	M_{CO}	ΔM_{He}	$\log T_{base,He}$	$\log T_{base,H}$
12	12	0	0	12.46	14.80	1.508	2.516	0.897	8.569	7.729
15	15	0	0	9.94	12.62	1.419	3.596	0.145	8.151	7.660
20	20	0	0	7.86	9.40	1.644	5.730	0.126	8.232	7.832
30	30	0	0	5.62	6.52	1.845	10.28	0.252	8.461	8.171
40	40	0	0	4.39	5.02	2.206	15.07	1.571	8.564	8.303
50	50	0	0	3.70	4.26	2.454	19.35	1.537	8.639	8.422
60	60	0	0	3.22	3.75	2.631	23.63	2.224	8.746	8.484
70	70	0	0	3.04	3.46	2.755	28.95	1.897	8.706	8.520
80	80	0	0	2.86	3.25	3.799	33.81	2.111	8.811	8.617
100	100	0	0	2.60	2.94	4.748	43.60	2.608	8.840	8.651
120	120	0	0	2.44	2.75	4.353	53.33	2.976	8.816	8.631
140	140	0	0	2.31	2.62	12.46	63.18	3.339	8.951	8.766
12	12	210	0.15	13.05	14.61	1.452	2.448	1.374	8.475	7.281
15	15	220	0.15	10.64	11.90	1.520	3.674	1.512	8.221	6.636
20	20	230	0.15	8.63	9.49	1.541	6.191	1.628	8.030	6.210
30	30	250	0.15	5.72	6.42	2.001	11.10	1.955	8.435	7.742
40	39.74	250	0.15	5.07	5.87	2.604	16.45	2.387	8.776	8.159
50	49.28	270	0.15	4.44	5.14	3.698	23.90	2.790	8.832	8.209
60	58.84	270	0.14	3.92	4.46	4.084	28.58	3.388	8.844	8.240
70	68.57	280	0.14	4.04	4.58	4.648	33.74	4.004	8.851	8.230
80	77.39	280	0.14	3.80	4.36	6.017	42.48	4.249	8.872	8.266
100	95.94	280	0.13	3.09	3.59	7.644	50.43	5.833	8.910	8.371
120	114.89	280	0.13	2.88	3.27	16.62	59.58	6.151	8.980	8.478
140	134.38	270	0.12	2.58	2.94	21.77	70.13	7.602	9.011	8.468
20	20	59	0.04	7.96	8.92	1.473	6.069	1.433	7.962	6.247
30	30	64	0.04	5.41	6.35	2.049	10.84	1.953	8.469	7.437
40	40	66	0.04	4.33	4.88	2.539	15.31	2.002	8.590	8.186
20	20	120	0.08	7.99	8.90	1.499	5.808	1.618	8.065	6.214
30	30	130	0.08	5.84	6.49	1.572	10.60	1.788	8.369	7.791
40	40	130	0.08	4.65	5.38	2.287	16.79	1.990	8.634	8.106

Notes. M_{ini} and M_{fin} are the initial and final masses; v_{rot} and $v_k \equiv \sqrt{GM/R}$ are the surface rotation velocity and the surface Kepler velocity at the zero age main sequence; τ_H and τ_{fin} are the hydrogen burning duration and the lifetime; M_{Fe}, M_{CO} and ΔM_{He} are the iron core mass, the carbon-oxygen core mass, and the helium shell mass at the end of the calculation; and $T_{base,He}$ and $T_{base,H}$ are the base temperatures of the helium shell and the hydrogen envelope at the end of the calculation. Masses are in $M_\odot$, velocities are in km sec^{-1}, times are in 10^6 yr, and temperatures are in K.

of the assumption of the uniform rotation at the stellar birth. Uniform rotation may realize if highly efficient viscosity develops inside a still accreting pre-main-sequence star, otherwise differential rotation will establish. Depending on the initial condition, the rotation profile evolves differently and thus different feedback is given to the stellar evolution. The difficulty here is that the evolution of rotation profile depends not only on the initial condition but also on the assumptions of the rotationally induced mixing. As discussed in Song et al. (2016), effective matter mixing occurs under the strong differential rotation, if shear instabilities are assumed to be effective. Contrastingly, mixing due to meridional circulation mainly depends on the speed of the rotation. Problems on the initial condition and the rotational mixing are strongly entangled.

3.1.2 Assumption of the *weak supernova*

Stellar matter is somehow ejected by supernova explosions. A precise treatment of matter ejection will be needed for accurate estimate of the supernova yields, which ideally includes three-dimensional hydrodynamics, inner explosion engine, higher order shock capturing and accompanying nucleosynthesis, and so on. The enormous computational cost will interrupt the systematic calculations, and moreover, large uncertainties still exist in understanding the mechanisms of explosions and matter ejections (e.g., Janka, 2012; Wongwathanarat et al., 2015). In order to avoid handling the complicated uncertainties, instead, I decide to take more pragmatic way to calculate stellar yields in this work.

Thus I assume a *weak explosion* for every yield calculation. This means that, explosive nucleosynthesis by shock heating is too weak to change the abundance distribution in the progenitor star. This first assumption will be appropriate especially for the outer region of a star. Indeed, for a calculation of explosive nucleosynthesis with a typical explosion energy of 10^{51} erg, the outer abundance distribution from the carbon convective region is not much affected by shock heating. Secondly, I assume that the weak explosion only expels such an unmodified outer stellar matter, which is loosely bound by the gravity. Such a weak supernova explosion has been proposed as a metal pollution mechanism to explain characteristic abundance patterns of CEMP stars. This is because, a highly effective fallback, which is required to account for the high abundance ratio between lighter elements and iron-peak elements observed in CEMP stars, can be naturally expected from the less energetic explosion. Actually, recent 2D hydrodynamical simulation by Chen et al. (2016) provides very consistent picture. They calculate hydrodynamical evolution of two low-energy Pop III CCSNe, injecting 0.6×10^{51} erg for the 12 $M_\odot$ model and 1.8×10^{51} erg for the 60 $M_\odot$ model. While only small amount of $Z > 20$ elements is mixed up and ejected, most of the material from the innermost region falls back to the central remnant.

Since only unmodified outer materials are assumed to be ejected in this model, simple integration gives a consistent supernova yield, even though the explosive nucleosynthesis is not followed in the procedure. Ejected mass of an element i,

M_i, is calculated as a function of $M_{\rm ej}$,

$$M_i(M_{\rm ej}) = \int_{M_{\rm ej}}^{\rm M_{surface}} X_i(M)dM, \qquad (3.1)$$

where $M_{\rm ej}$ is the inner boundary of the ejection and X_i is an abundance distribution of i in terms of mass fraction. The inner boundary $M_{\rm ej}$ is arbitrarily taken, though it may relate to the explosion energy in reality. In our model, material that distributes below $M_{\rm ej}$ is assumed to be completely captured by the central remnant, and does not contribute to the yield. Compared with the mixing-fallback model, results of the weak supernova model will agree with them, if the mixing-fallback parameters of outer boundary of the mixing region, $M_{\rm mix}$, and the ejection fraction, f, are respectively specified to $M_{\rm ej}$ and zero. Thus, mixing process during the explosion is not important ingredient in our model, while mixing process during the stellar evolution is of importance.

Two different mechanisms are considered to account for the weak explosion. Firstly, mass ejection from a weak CCSN will be well represented by the weak supernova model. In addition to the weak CCSN, the *failed supernova* model, which ejects their outer layer due to the reduction of the gravitational mass by neutrino emission (Nadezhin, 1980; Lovegrove & Woosley, 2013), may also be compatible with the weak explosion. In any case, considering that the fallback is driven by the reverse shock developing at the core/envelope boundary (e.g., Hachisu et al., 1990; Kifonidis et al., 2003), the typical ejection mass $M_{\rm ej}$ will be comparable to the CO core mass $M_{\rm CO}$ of the progenitor. Thus I define a dimension-less parameter $f_{\rm ej} \equiv M_{\rm ej}/M_{\rm CO}$ for the function of the ejected mass.

3.2 Hydrostatic evolution

3.2.1 Hydrogen burning phase

A massive first star is known to have a high equilibrium temperature at the core center during its hydrogen burning stage. Figure 3.1 shows the evolution of the central temperature and the central carbon mass fraction of rotating and non-rotating Pop III models of 12, 20, 40, 80, and 120 $M_\odot$. The central temperature becomes 1.0–1.25×10^8 K for 12–140 $M_\odot$ models. This is due to lack of the CNO-elements at the formation of the first star.

Before a massive Pop III star reaches the equilibrium state, it firstly burns hydrogen by the *pp-chain*. However, if the star is more massive than 20 $M_\odot$, the reaction rate is insufficient to balance with the surface luminosity. The star keeps contracting even after the hydrogen ignition. Contraction stops when the central temperature rises enough to ignite helium by the *triple-α* reaction. By this new reaction, small amount of ^{12}C and ^{16}O are synthesized at the center of the star. These helium burning products, then, act as catalysts of the much effective hydrogen burning process, the *CNO-cycle*. The energy release by the hydrogen burning stabilizes the star, and the star finally reaches the zero-age-main-sequence (ZAMS). The required mass fractions of CNO-elements are small; depending on
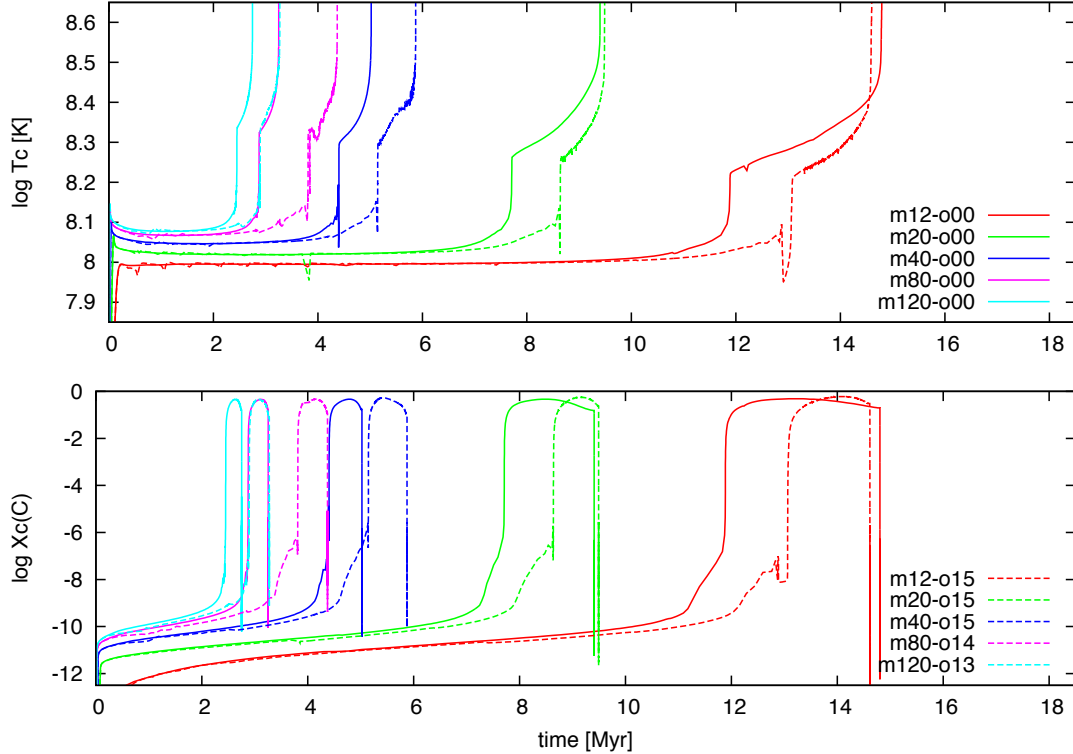
Figure 3.1: Evolution of central temperatures (top) and central carbon mass fraction (bottom) with time are shown for 12, 15, 20, 40, 80, 120 $M_\odot$, non-rotating and rotating Pop III models. Non-rotating and rotating models are respectively shown by solid or dashed lines. Each model name, m(*mass*)-o(*rotation*), indicates the initial mass of (*mass*) $M_\odot$ and the initial rotation of (*rotation*) $\times 10\ v_{\rm ini}/v_{\rm k}$.

the stellar mass, even 10^{-12}–10^{-10} CNO elements are enough for the stabilization. Therefore, the contraction stops as soon as the helium burning takes place. The least massive 12 $M_\odot$ models are already stabilized by the pp-chain, and enter the zero-age-main-sequence (ZAMS) phase. This can be seen as a lack of the first rise of the temperature in the Fig. 3.1. The critical initial mass of 20 $M_\odot$ to have a CNO-cycle at its ZAMS is well coincide with the previous works (Marigo et al., 2003; Ekström et al., 2008; Yoon et al., 2012).

Then a star enters the long equilibrium phase of stable core hydrogen burning. Due to the much contracting initial structure, as well as to the small opacity of the zero-metallicity gas, the Pop III star develops a compact structure in this phase. The compact stars accordingly have blue surfaces with the high surface temperatures. The Hertzsprung-Russell diagram of these models are plotted in Fig. 3.2. Comparing with the black dashed line, which shows the ZAMS in our Galaxy (Ekström, 2015, private communication), it is inferred that Pop III models have ∼ 0.3 dex higher surface temperature than the solar metallicity stars. The
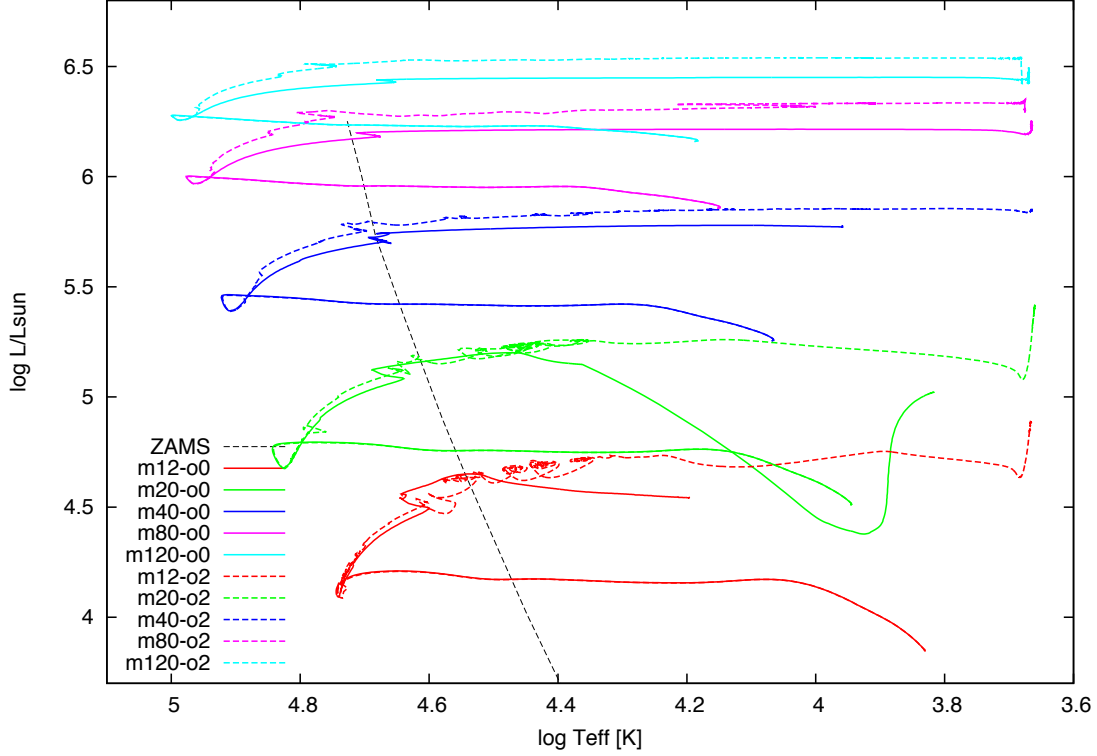
Figure 3.2: Surface evolutions of 12, 20, 40, 80, 120 $M_\odot$, non-rotating and rotating Pop III models are shown. Non-rotating and rotating models are respectively shown by solid or dashed lines. The black dotted line shows the ZAMS observation in our Galaxy.

high surface temperature is especially important for the re-ionization by Pop III stars.

During the hydrogen burning phase, a star burns its hydrogen into helium, forming an inert helium core at its center. The size of the helium core is mainly determined by the convection driven by the core hydrogen burning. Then it is enlarged by other mixing processes of the rotation induced mixing as well as the convective overshooting. As a result of the core extension, a redder and more luminous evolution of the main sequence can be seen in the HR diagram. Moreover, those additional mixing supply fresh hydrogen from outside to inside the convective core. The continuous fuel supply extends the lifetime of the core hydrogen burning phase. The lifetimes of rotating and non-rotating models are compared in Fig 3.1. The lifetime of the main-sequence phase significantly decreases with increasing the initial mass, spanning 12.4 Myr (12 $M_\odot$) to 2.3 Myr (140 $M_\odot$) for non-rotating models, but at the same time, $\sim$ 10% extension can be done by the rotation induced mixing, spanning 13.0 Myr (12 $M_\odot$) to 2.6 Myr (140 $M_\odot$) for rotating models. Comparing the lifetimes to the previous works, I also find the reasonable

Table 3.2: Comparison of stellar lifetimes

M_{ini}	Ekström et al. (2008)			Yoon et al. (2012)			This work		
	v_{rot}	τ_{H}	τ_{fin}	v_{rot}	τ_{H}	τ_{fin}	v_{rot}	τ_{H}	τ_{fin}
15	0	10.60	11.6	0	13.64	14.35	0	9.94	12.62
15	800	13.20	14.4	325.5	14.58	15.28	220	10.64	11.90
60	0	3.60	3.96	0	3.88	4.22	0	3.22	3.75
60	800	4.20	4.57	631.3	4.45	4.76	270	3.92	4.46

Notes. M_{ini}, v_{rot}, τ_{H}, and τ_{fin} are the initial mass, the surface rotation velocity, the hydrogen burning duration, and the lifetime, respectively. Masses are in $M_{\odot}$, velocities are in km sec^{-1}, and times are in 10^6 yr.

agreement among the theoretical calculations (Table 3.2). Longer lifetimes in Yoon et al. are resulted from the more efficient overshooting in their calculations (Yoon et al., 2012). Scatter of lifetimes will be due to different efficiencies of both convective overshooting and rotational mixing.

3.2.2 Helium burning phase

A star re-starts to contract after the core hydrogen depletion. It is this moment when an envelope of a metal-rich counterpart suddenly inflates and the star enters the red-giant branch. The similar inflation also takes place for metal-free first stars, but it is limited to occur only in massive models of > 70 M$_{\odot}$ for the non-rotating cases. The lack of the inflation is especially important if the Pop III star is in a close binary system, because the change of the radius determines the final fate of the system (Kinugawa et al., 2014). In the case of a metal-rich star, the internal luminosity steeply increases as the hydrogen shell burning activates during the core contraction phase. The luminosity then supplies the work to expand the envelope. On the other hand, in a metal-free star, the luminosity increases more mildly and this delays the envelope inflation. Firstly this is because a metal-free star, which has a higher core temperature of hydrogen burning, need not to contract so much to ignite helium. The temperature and thus the energy liberation of the hydrogen shell burning, in turn, does not increase as much by the core contraction. Secondly, since mass fractions of the CNO-elements are very small at this region, the shell burning takes place only less effectively.

Similar to the hydrogen burning phase, core convection and the convective overshooting around the core determines the size of the CO core and the lifetime of the helium burning phase. With increasing the initial mass or the He core mass of the star, the lifetime of the helium burning phase decreases. The 12 M$_{\odot}$ models show longer lifetimes of 2.4 Myr (non-rotating) and 1.6 Myr (rotating) than that of 140 M$_{\odot}$ models of 0.31 Myr (non-rotating) and 0.36 Myr (rotating). For non-rotating cases, the large fraction of the Helium core is then occupied by the forming CO core. This, in turn, results in a relatively thin helium layer at the end of the helium burning phase.

Rotationally induced mixing during the core helium burning phase can have

important effects on the Pop III stellar evolution, as it accompanies with an additional nuclear burning and nucleosynthesis. The mixing takes place around the convective region inside the helium core. The inner processed material is mixed up by the mixing, as a result, the remaining hydrogen in the outer helium layer encounters the helium burning products, carbon and oxygen. This leads to very efficient hydrogen burning via the CNO-cycle, making several impacts on the stellar evolution. First, the large energy generation increases the stellar luminosity, modifying the star as a red giant. As discussed earlier, Pop III massive stars tend to evolve compact. However, *all* rotating models calculated in this work evolve to red giants due to the effective shell hydrogen burning. This also indicates that a steep entropy jump is formed at the hydrogen/helium boundary in a rotating Pop III star. Second, since a large quantity of hydrogen burning products accretes onto the helium core, a rotating model forms a larger CO core and thicker helium layer than the non-rotating counterpart. Finally, the CNO cycle leaves a satisfactory amount of processed nitrogen behind in the outer helium layer. Part of them are farther mixed into the hydrogen envelope. The nitrogen production in a rotating model is an important outcome in stellar nucleosynthesis, and to be discussed in much detail later.

3.2.3 Later phases

After the formation of a CO core, the timescale of evolution suddenly decreases. This is owing to the initiation of efficient energy loss by neutrino emission. In a core of high temperature, neutrinos are created by thermal processes, especially due to the pair creation process (Itoh et al., 1989, 1996). The higher the core temperature is, the more efficient the neutrino emission rate becomes. Hence, as the neutrino energy loss dominates the cooling of the core, it accelerates the core contraction.

In a contracting core, small scale burnings of carbon, neon, oxygen, and silicon successively take place within a short lifetime. The reason of the small scale in mass is again due to the neutrino energy loss. Since the greater part of the energy generated by a nuclear burning is lost by the neutrino emission in these advanced stages, the energy need to drive a large convection becomes insufficient. This remarkably affects core carbon burning in metal-free stars. That is, in models more massive than 12 $M_\odot$ for non-rotating or 15 $M_\odot$ for rotating cases, convection is not activated by core carbon burning in its early phase. Evolution of convective regions is shown in Appendix B, in which green hatched regions show the convective regions in a star.

Some models in $\sim$ 15–30 $M_\odot$ in our model grid are affected by the *hydrogen ingestion* in this advanced phases. A convective shell exists in a helium layer in such a model. The convection develops when the central core contracts and the base temperature of the helium layer increases. Suddenly the shell convection penetrates the μ- and entropy-barrier at the border between the helium/hydrogen layer. As a results, small fraction of hydrogen are mixed into the inner high temperature helium layer, and rapidly reacts generating energy in a very short timescale. The envelope inflates responding to the energy generation, and some

peculiar nucleosyntheses result in. Although such a strange phenomenon has been known to occur in massive (15–40 $M_\odot$) low metallicity stars (e.g., Fujimoto et al., 1990; Ekström et al., 2008; Heger & Woosley, 2010; Limongi & Chieffi, 2012; Yoon et al., 2012), the mechanism of the convective penetration, which takes place only for models within the relatively small parameter range, is not clearly understood.

During the successive burning phases, a core of iron is developed for less massive stars of $\lesssim 140\ M_\odot$. Several mechanisms account for the contraction of the iron core. The first is the silicon shell burning, which increases the mass of the central iron core. The second is the neutrino cooling, by which the entropy of the core is reduced. Finally, electron capture reactions by silicon burning products reduces Y_e and the electron pressure of the core. The iron core finally collapses, closing the hydrostatic phase of evolution. On the other hand, if the star is more massive, the hydrodynamic collapse initiates after the core helium burning phase. This is due to the strong electron-positron-pair-creation instability, which is discussed later in detail.

Let me shortly discuss here about the problem of chaotic (non-convergent) results of the 1D stellar evolution. The problem has become well known after Ugliano et al. (2012) have shown the non-monotonic behavior of the compactness parameter, which correlates well with the explosionability of the progenitor model, against the initial mass (see also Sukhbold & Woosley, 2014). One may consider that this problem indicates the unreliability of the stellar evolution calculations, since such a non-monotonic result is hardly expected from a simple initial-value problem. But in reality, this reflects the fact that the stellar phenomena are highly non-linear and it is a too simplistic prospect to expect every outcome of the stellar simulations will correlate with the initial mass. In the stellar community, it has been recognized that even a small difference in the initial mass can result in a large difference in the iron core mass. The mechanism of the growth of the small fluctuation can be understood as follows. Firstly, because a stellar core formed in later phases is mainly supported by degenerate electrons, the core temperature is not sensitive to the pressure structure. On the other hand, both nuclear energy generation rate and energy loss rate by neutrino emission are highly dependent on the temperature. Thus energy generation in a core with slightly different temperature can be different. The generating energy is consumed to activate a core convection and heat up the region. The size of the convection is determined by the balance between the energy generation and the energy loss, hence the width of the convection is severely affected by the difference between them. The width of the convection determines the size of the next burning core. Since the past history remains as the difference in the core size, the first fluctuation in temperature can severely affect the final size of the iron core.

3.2.4 Iron core collapse

As the iron core contracts, the core temperature increases. Accordingly, a hydro-dynamical instability sets in the core, and a runaway collapse takes place. The iron core collapse divides the hydrostatic and hydrodynamic evolution of the star. The evolution of central temperature and density is shown by Fig. 3.3. In the
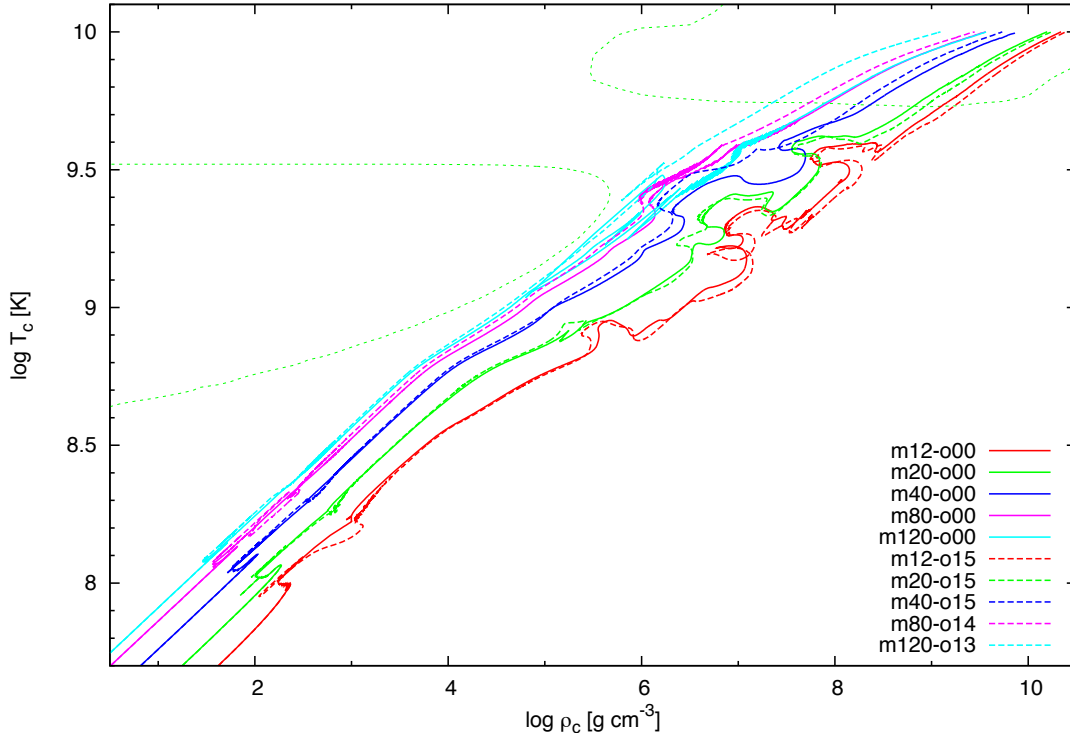
Figure 3.3: Evolutions of 12, 20, 40, 80, 120 $M_\odot$ non-rotating and rotating Pop III models are shown in the central density-temperature plane. Rotating and non-rotating models are respectively shown by solid or dashed lines Green dotted lines show the boundary of the hydrodynamically unstable regions of $\gamma < 4/3$.

figure, the hydrodynamically unstable regions are outlined by green-dotted lines.

In general, a gas having the adiabatic index $\gamma \equiv d\log p/d\log\rho|_{ad} < 4/3$ becomes hydrodynamically unstable when it forms a spherical Newtonian self gravitating system. This can be understood by carrying out a simple dimensional analysis on hydrostatic equations. The equation of the pressure balance leads to

$$4\pi R^3 p \sim \frac{GM^2}{R}, \tag{3.2}$$

which shows the balance between the thermal energy and the gravitational energy of the system. This relation further shows that the pressure of the system, p, should increase more rapidly than $p \propto R^{-4}$ to keep the stability when the system shrinks and the radius R decreases. Since the mass of the system can be regarded as a conservative value, the density of the system, ρ, increases as $\rho \propto R^{-3}$ during the contraction. Therefore, the hydrodynamical instability takes place when the increase of the gas pressure is below the required value of $p \propto \rho^{4/3}$ under an adiabatic contraction.

Two kinds of gases mainly contribute to the pressure of the iron core, the
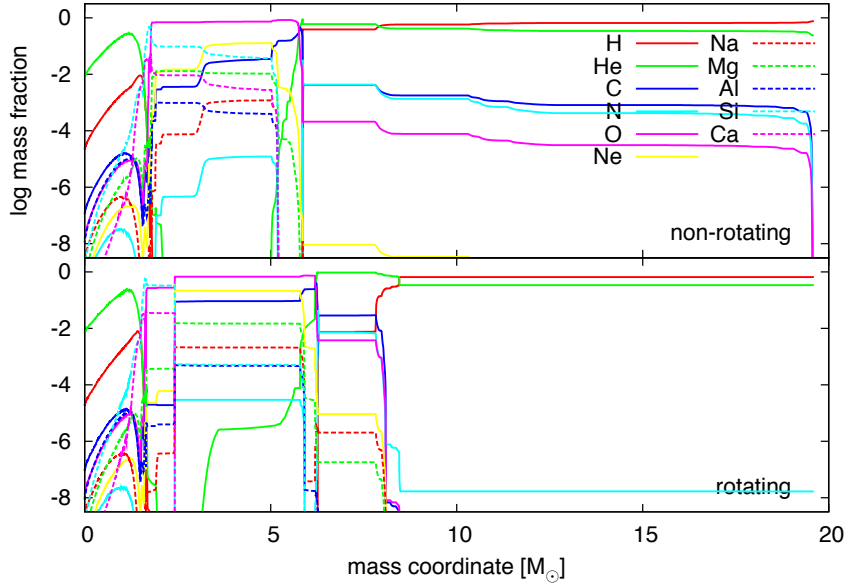
Figure 3.4: Mass fraction distributions of 20 $M_\odot$ models. The top panel corresponds to the non-rotating case, while the bottom to the rotating one. For the non-rotating model, M_{CO} and ΔM_{He} are 5.730 $M_\odot$ and 0.126 $M_\odot$, while for the rotating model, these values become 6.191 $M_\odot$ and 1.628 $M_\odot$. Abundant hydrogen in the helium layer of the non-rotating model results from proton ingestion during core carbon burning phase.

electron-positron gas and the ionic gas. Since the electron-positron gas has the marginally critical adiabatic index of $\gamma_{elec} \simeq 4/3$ in this high temperature and density environment, the ionic gas should support the star by having a larger adiabatic index $\gamma_{ion} > 4/3$. However, under the high temperature condition, nuclear reactions take place with fast enough speeds to allow the reaction equilibrium, so called the nuclear-statistical-equilibrium (NSE), to be achieved. As the temperature reaches the critical value of $\sim 10^{9.8}$ K, photo-dissociation takes place on iron elements to form free protons, neutrons, and α-particles. Due to this transformation, the internal energy of the matter is changed to the rest mass energy. Accordingly, the pressure is reduced and the adiabatic index of the gas becomes lower than the critical, $\gamma < 4/3$.

3.3 Yields of weak supernovae

As a result of stellar evolution calculations, abundance distributions of various progenitors are obtained (Fig. 3.4–3.7). I find that diverse nucleosynthesis take place in a helium layer, in which a condition for nucleosynthesis, such as the density, the temperature, and the composition, largely depends on the initial mass and the rotation velocity. To illustrate the variations in helium layers, abundance distributions of non-rotating and rotating 40 $M_\odot$ models are shown by Fig. 3.5. In the helium layers, mass fractions of ^{12}C and ^{16}O do not show much differences. On the other hand, intermediate mass elements of ^{23}Na, ^{24}Mg, and ^{27}Al are produced

35
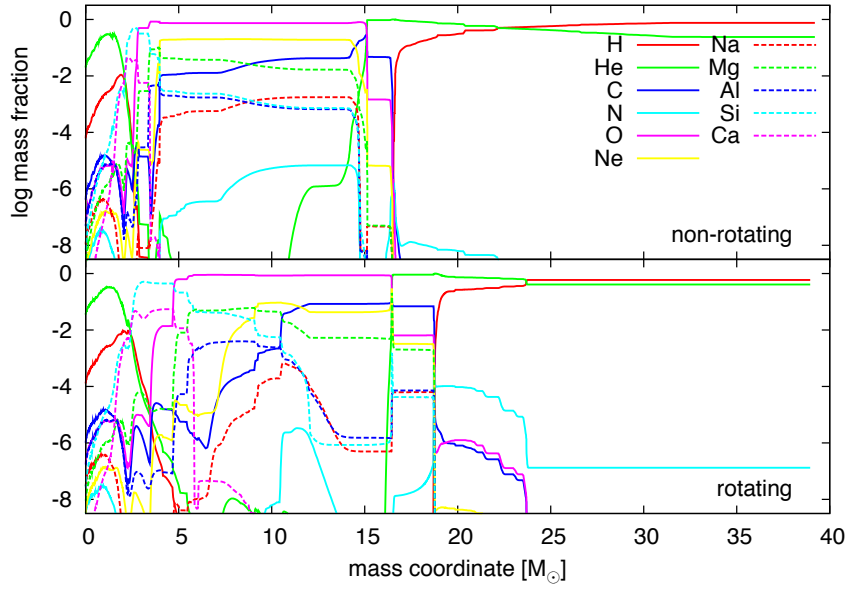
Figure 3.5: Same as Fig. 3.4, but for 40 M$_\odot$ models. For the non-rotating model, M_{CO} and ΔM_{He} are 15.07 M$_\odot$ and 1.571 M$_\odot$, while for the rotating model, these values become 16.45 M$_\odot$ and 2.387 M$_\odot$.
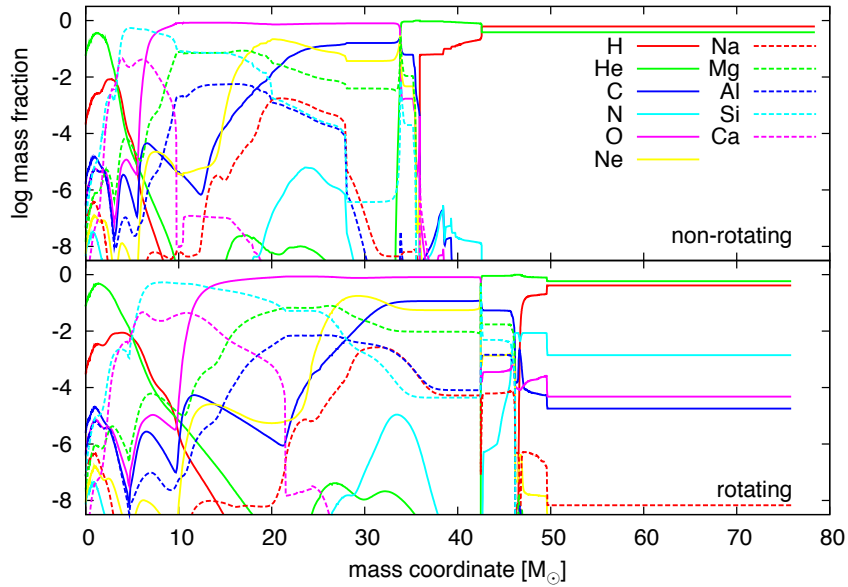
Figure 3.6: Same as Fig. 3.4, but for 80 M$_\odot$ models. For the non-rotating model, M_{CO} and ΔM_{He} are 33.81 M$_\odot$ and 3.674 M$_\odot$, while for the rotating model, these values become 42.48 M$_\odot$ and 3.823 M$_\odot$.
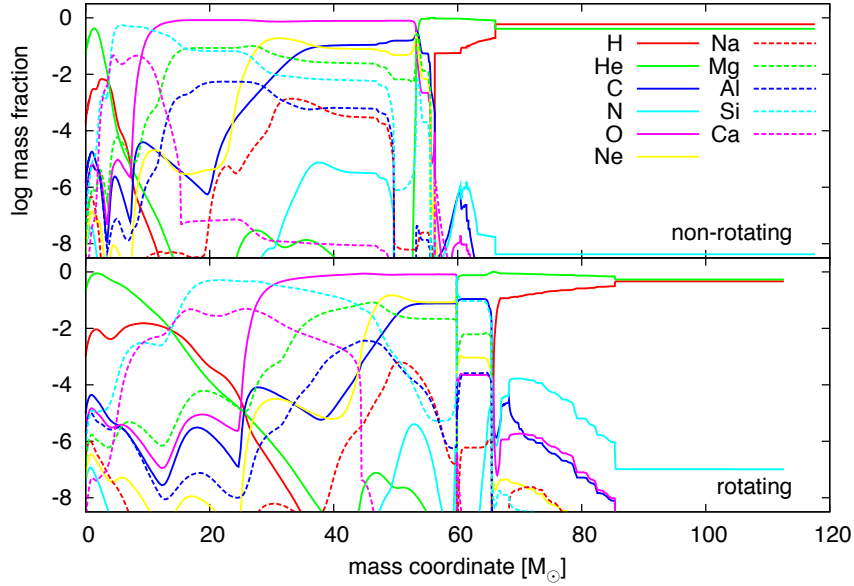
Figure 3.7: Same as Fig. 3.4, but for 120 $M_\odot$ models. For the non-rotating model, M_{CO} and ΔM_{He} are 53.33 $M_\odot$ and 2.976 $M_\odot$, while for the rotating model, these values become 59.58 $M_\odot$ and 6.151 $M_\odot$.

in the helium layer of the rotating model, and abundant ^{14}N is distributed in the hydrogen envelope in the model.

Based on the abundance distributions, yields of weak supernovae are calculated. Results are shown in Figs. 3.8–3.10 for selected models. I find that the characteristics of weak supernova yields directly reflect the characteristics of nucleosynthesis taken place in the progenitor's helium layers. Thus, the abundances of C, N, O, Na, Mg, Al, Si, and Ca in the yields significantly change depending on the parameters of the progenitor modes. In the following, characteristics of these abundance patterns are analyzed.

3.3.1 Carbon and Oxygen

Through triple-α reaction and succeeding α-capture reaction on ^{12}C, carbon and oxygen are produced. The main production site is a convective helium core, in which the prime isotope, ^{4}He, is almost completely consumed during the stellar life. The other production site is a shell helium layer, which forms as a remnant of the edge region of the previously existed helium core after core helium depletion. Between the two sites, I focus on the nucleosynthesis in the shell helium layer, since models with different masses show variations in the burning conditions at the layer.

Figure 3.11 shows carbon yields as a function of the initial mass, taking CO core masses as M_{ej} for each model. In addition, the production factor of M_O/M_C is presented in Fig. 3.12. Hereafter, all figures showing yield ratios take M_{ej} at the CO core masses. Three important characteristics on production of carbon and oxygen in a helium layer can be inferred from those figures. Firstly, production of carbon
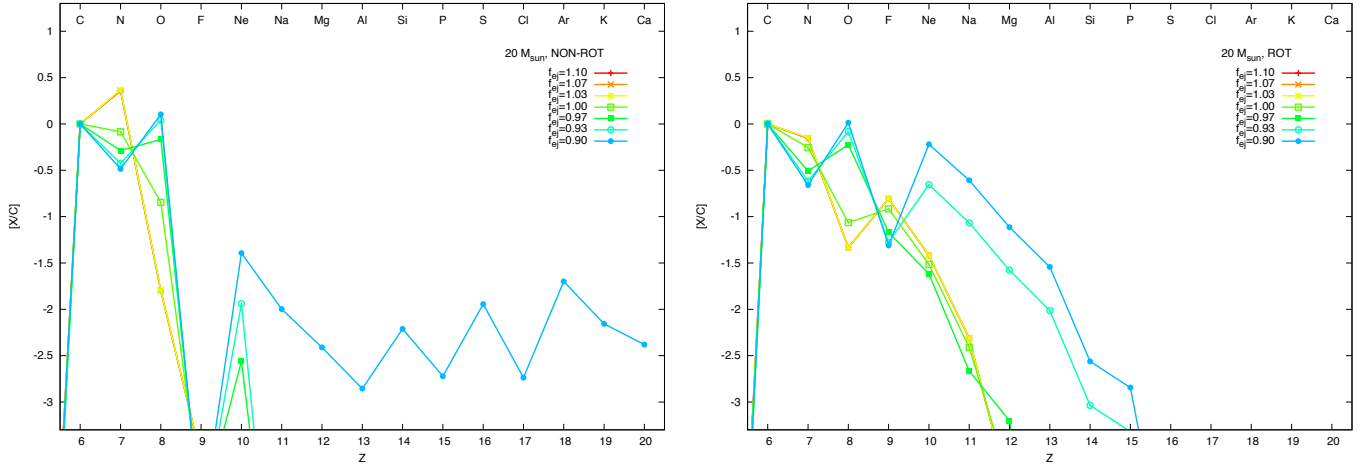
Figure 3.8: Abundance patterns of weak SN yields from the non-rotating (left) and rotating (right) 20 $M_\odot$ models. Yields with different M_{ej} are shown by different colors. The abundance of carbon is used for the normalization.
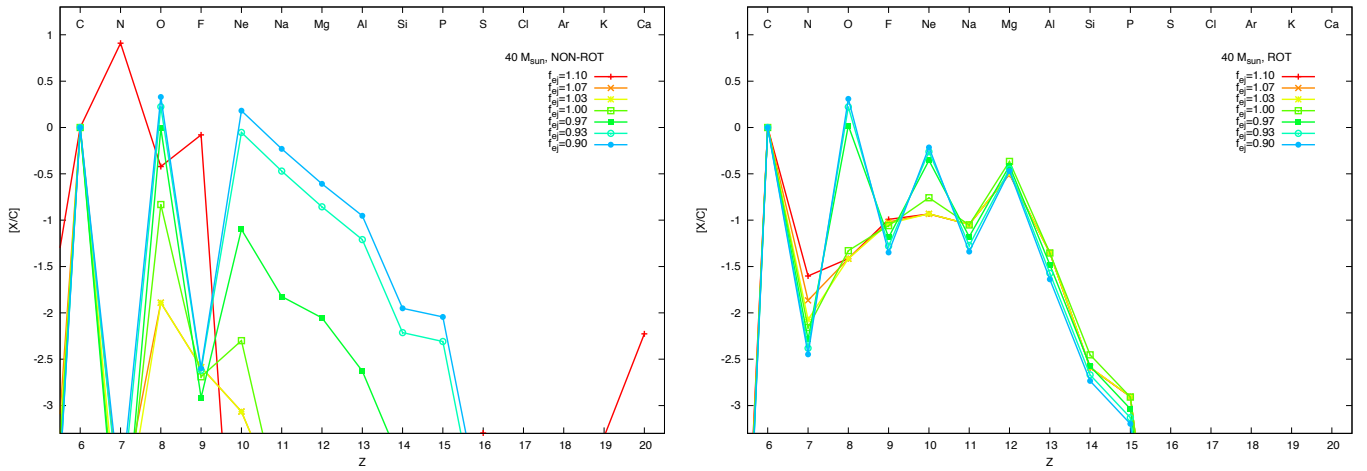

Figure 3.9: Same with Fig. 3.8 but for 40 $M_\odot$ models.
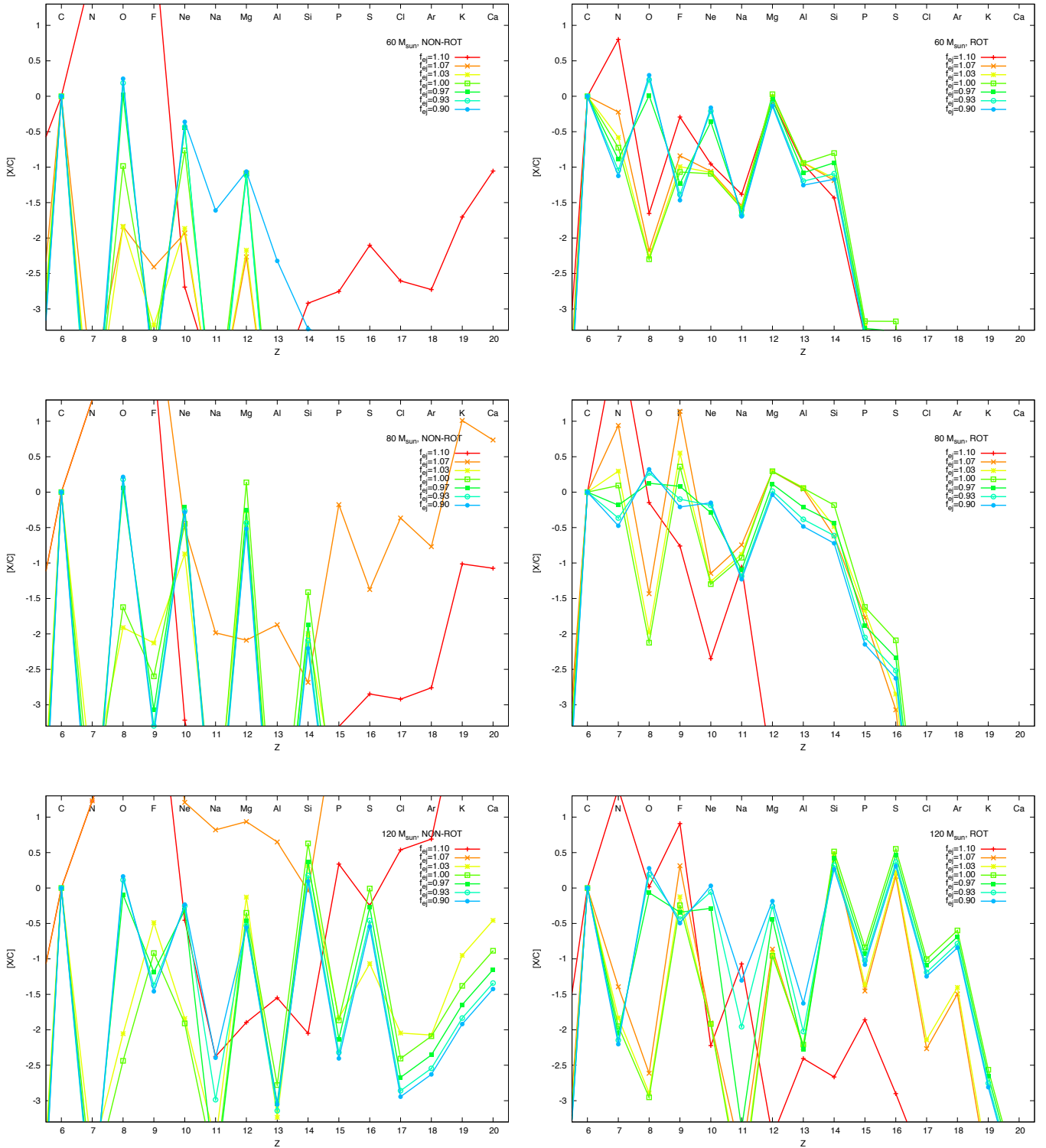
Figure 3.10: Same with Fig. 3.8 but for 60, 80, and 120 M$_\odot$ models.
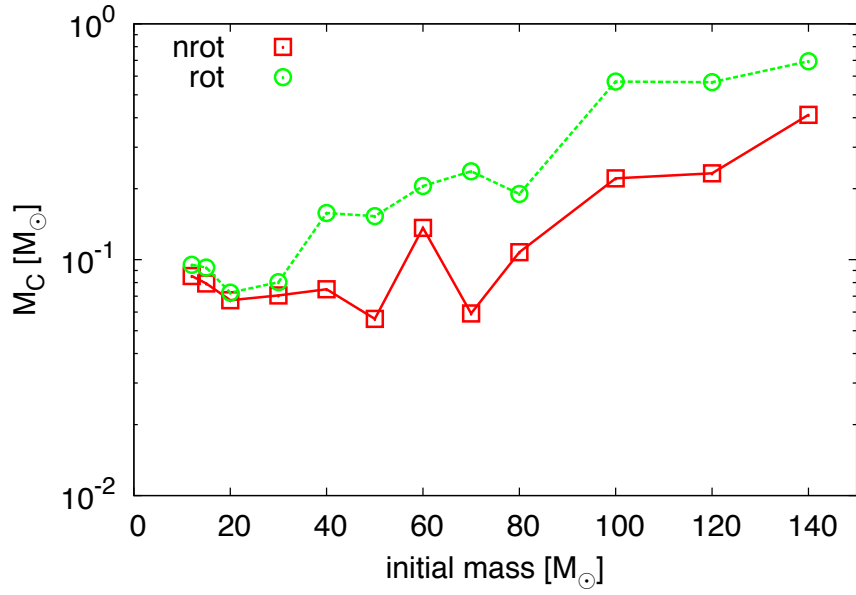
Figure 3.11: Integrated yield of carbon as a function of the initial mass. All isotopes of carbon are summed up. The range of integration is from the base of the helium layer to the surface. Results of non-rotating models are shown by red open squares connected by red solid lines, while green open circles with dashed lines correspond to rotating models.
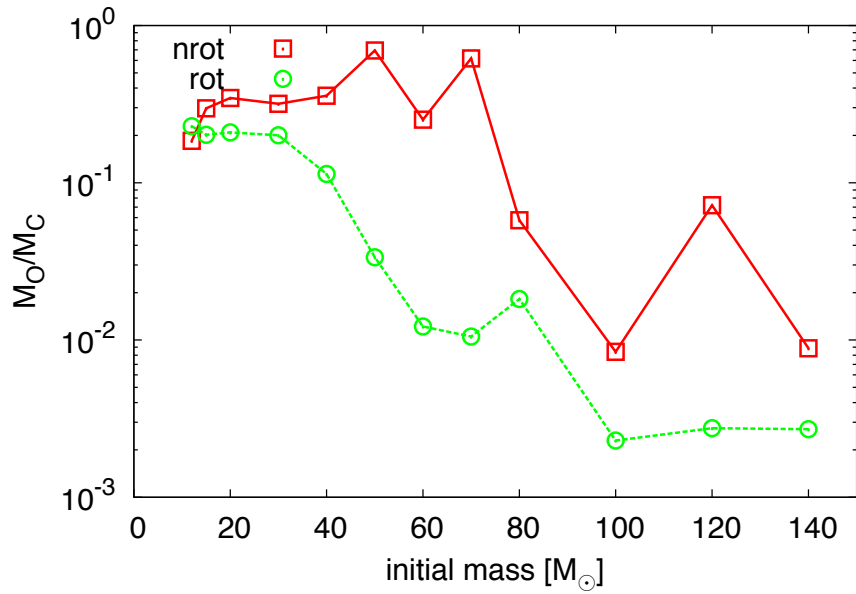
Figure 3.12: The production ratio between oxygen and carbon, M_O/M_C, as a function of initial mass. All isotopes of oxygen and carbon are summed up, respectively. Red open squares show non-rotating results, and green open circles with dashed lines show rotating results, respectively.
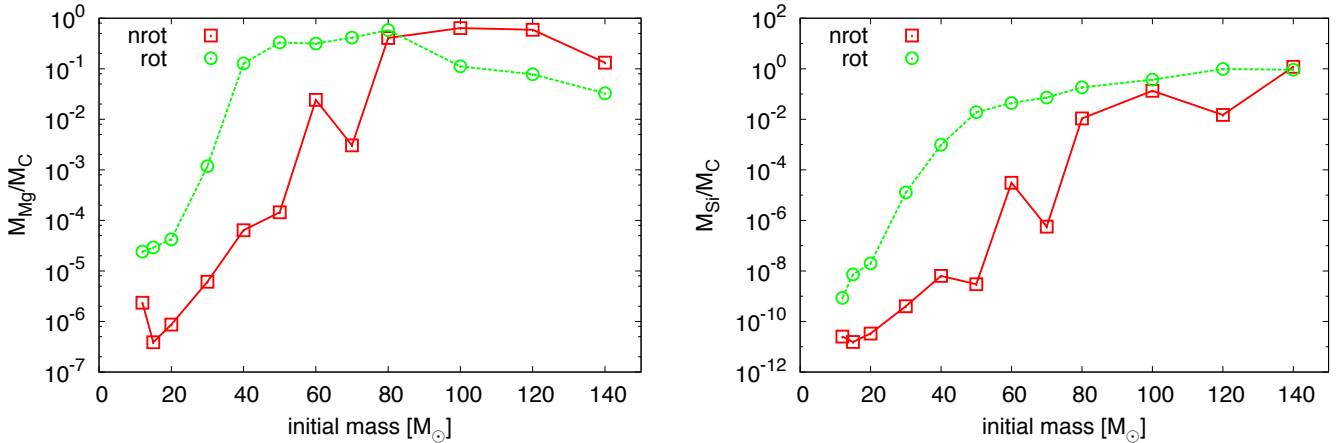
Figure 3.13: Same as Fig. 3.12, but for magnesium (left) and for silicon (right).

and oxygen takes place in all of the models. This is because the temperature at the helium burning shell is high enough to allow the triple alpha and alpha capture reactions to occur. Secondly, the O/C ratio does not exceed unity in all models. This is particularly important, because O/C ratio in the case of core helium burning always exceeds unity. Therefore, if one observes a O/C ratio smaller than the unity from a metal-poor stellar surface, it suggests that the metals in the star are produced in an outer layer of the source star, but not in the central CO core. Finally, the heavier the initial mass of the progenitor is, the smaller the resulting O/C ratio is. As a conclusion, carbon and oxygen production with a small O/C can be regarded as a general nucleosynthetic signature of elemental production in helium layers, and more massive stars will have a smaller O/C ratio.

3.3.2   Neon, Magnesium and Silicon

Intermediate-mass alpha elements of ^{20}Ne, ^{24}Mg, and ^{28}Si are mainly produced during several burning phases inside a CO core. For example, neon and magnesium can be produced through carbon burning as ^{12}C + ^{12}C → ^{20}Ne + α and ^{12}C + ^{12}C → ^{23}Na + p, ^{23}Na + p → ^{24}Mg. Also, silicon is produced by alpha capture on ^{24}Mg during neon or oxygen burning and by ^{16}O + ^{16}O → ^{28}Si + α. Besides the main nucleosynthesis over the phases, I find that these elements are synthesized in a helium layer of a massive star in its later evolution stages. In this case, these alpha elements are produced via a series of alpha capture reactions on ^{16}O.

The production ratio between magnesium and carbon is shown in the left panel of Fig. 3.13. Efficient production of magnesium occurs for rotating $\geq$ 40 M$_\odot$ models and non-rotating $\geq$ 60–80 M$_\odot$ models. The initial mass dependence can be characterized by the steep rise in less massive models and the plateau in more massive models. The increase of the magnesium yield is a result of more efficient alpha capture reactions in massive models, and the plateau is due to the consumption of seed elements of ^{20}Ne. The same trend on the progenitor initial mass is also found in the silicon production ratio, shown in the right panel of Fig. 3.13.
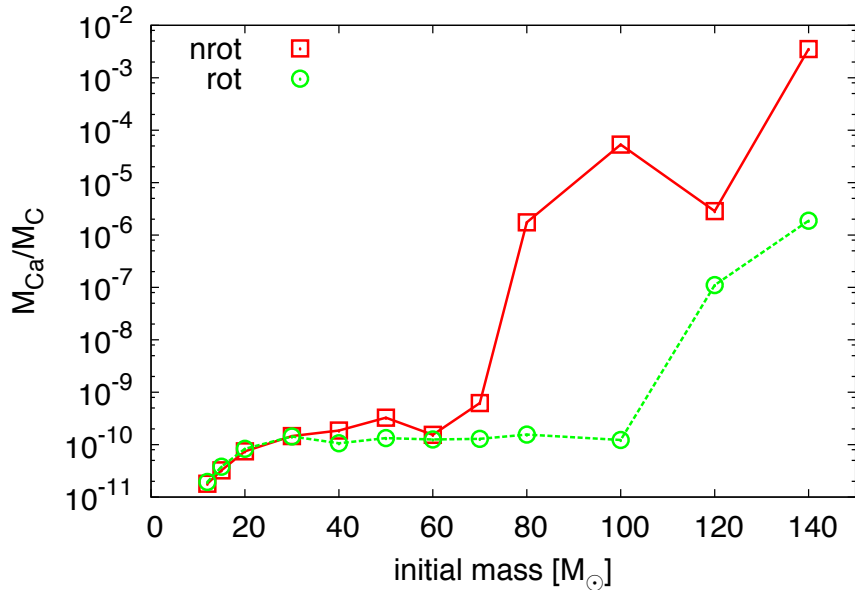
Figure 3.14: Same as Fig. 3.12, but for calcium.

Based on the trend in the initial mass dependence, the pattern of the produced alpha elements can be used as a probe of the progenitor's initial mass.

3.3.3 Calcium

Figure 3.14 shows production ratio of calcium. For rotating models, only the two most massive models of 120 $M_\odot$ and 140 $M_\odot$ show the enhancement. It is fast alpha capture reactions at the base of the helium layer that synthesize calcium in these rotating models. In this small region, other alpha elements of ^{28}Si, ^{32}S, and ^{36}Ar are also produced, and by (α, p) reactions on these alpha elements, some odd species of ^{31}P, ^{35}Cl, and ^{39}K are synthesized as well. For non-rotating models, abundant calcium production occurs for stars of ≥ 80 $M_\odot$. Interestingly, a totally different nuclear process accounts for the production in non-rotating cases.

The calcium production in non-rotating models is attributed to proton capture reactions in a hydrogen burning shell. Similar to helium shell burning, the temperature of the hydrogen burning shell increases as the stellar core contracts. If the base temperature gets high enough, break-out reactions from the CNO cycle take place (Wiescher et al., 1999). These reactions occur at the base of the hydrogen envelope of non-rotating ≥ 80 $M_\odot$ models in our calculation, resulting in production of proton rich isotopes including ^{40}Ca. Figure 3.15 shows how the reaction goes in the non-rotating 140 $M_\odot$ model after the central carbon burning phase. Since the model has the largest initial mass in all of our models, the base temperature in the hydrogen burning region gets very high, $\log T_{\mathrm{base,H}} = 8.66$, when the star shrinks after the depletion of core carbon. The required high base temperature does not realize in a rotating models, since efficient heating by the previous CNO-cycle lifts up the envelope and reduces the base temperature in advance.
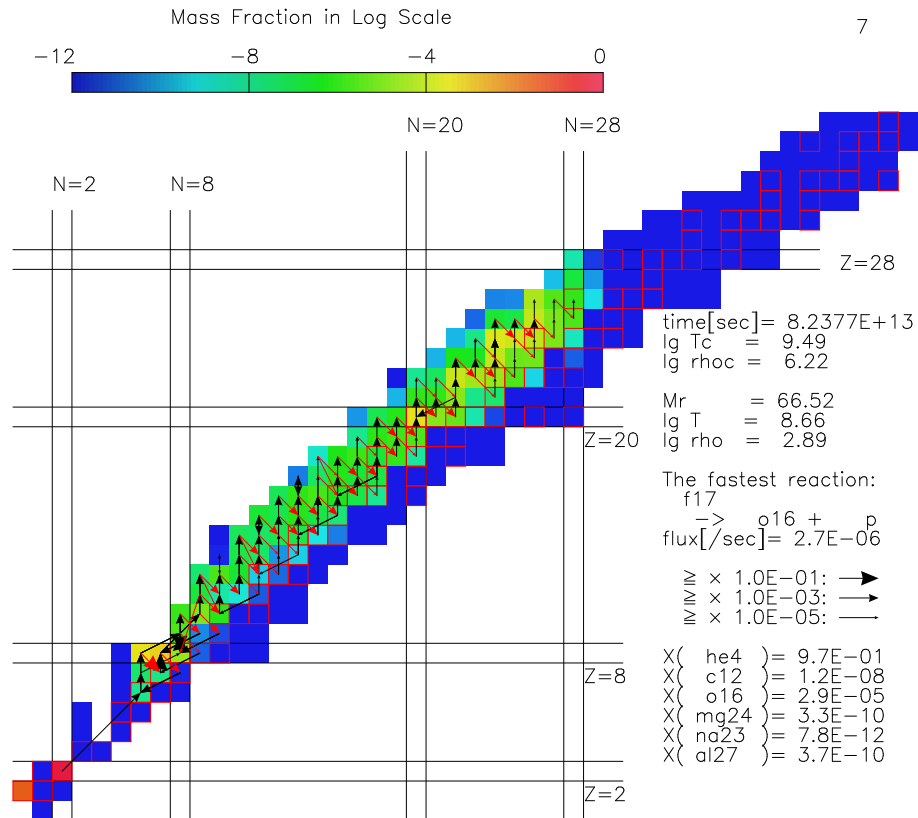
Figure 3.15: A nuclear chart showing fast reactions at $t \sim 8.24 \times 10^{13}$ sec. Reactions at the base of the hydrogen burning shell of the non-rotating 140 $M_\odot$ are shown. X- and y-axis show neutron and proton numbers, red squares are for stable isotopes, and colors show the mass fraction of each isotope. Three different sizes of arrows show different magnitudes of fluxes normalized by the fastest reaction. Black arrows correspond to thermonuclear reactions, while red arrows correspond to reactions involving weak interactions.
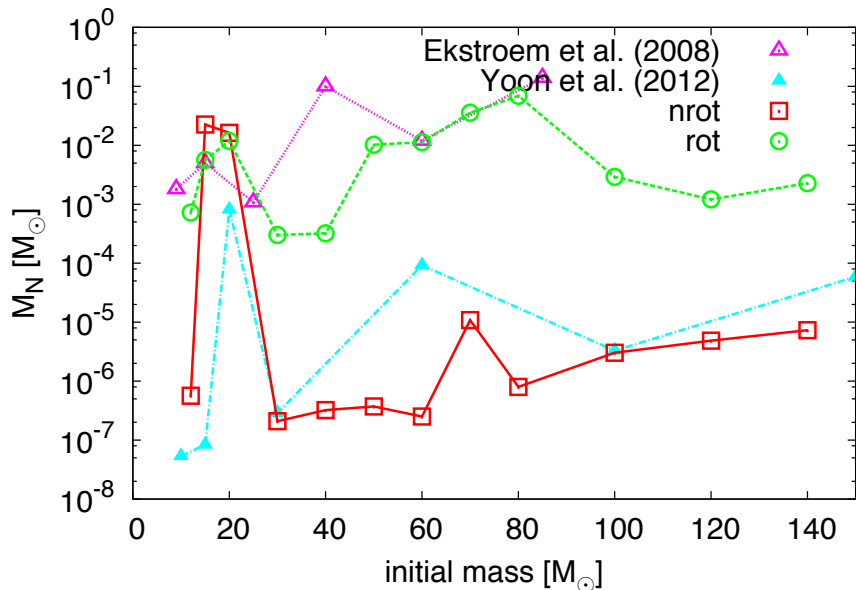
Figure 3.16:   Same as Fig. 3.11, but for nitrogen. In addition to our results shown by red squares (non-rotating models) and green circles (rotating models), results of rotating models from previous works are plotted. Magenta-open triangles show results by Ekström et al. (2008) and blue-filled triangles are results of models of $v_{\mathrm{ini}}/v_{\mathrm{k}} = 0.2$ by Yoon et al. (2012).

3.3.4   Nitrogen

Nitrogen is an especially important element in the context of stellar physics and stellar nucleosynthesis in the early universe. Since nitrogen is only synthesized as a by-product of the CNO-cycle in an evolving star, nitrogen synthesis requires foregoing production of seed elements of carbon or oxygen. However, because a metal-free star does not contain any metals at its birth, the CNO-cycle is only very weakly activated in both core and shell hydrogen burning. If canonical non-rotating stellar models are considered, nitrogen synthesis starts *after CO-rich stars are formed*. Nitrogen produced in such a metal-rich star is called *secondary* nitrogen.

The situation changes if efficient matter mixing takes place inside one star. Carbon and oxygen are naturally produced by core helium burning. Hence, when the CO-rich core material is transported to the hydrogen-rich outer envelope, nitrogen is expected to be synthesized as a result of the CNO-cycle. Such nitrogen produced in metal-free or extremely-metal-poor stars are called *primary* nitrogen. Meynet & Maeder (2002a,b) shows that rotationally induced mixing transports inner material to the envelope, and shows that nitrogen is produced in their rotating massive first stars.

Figure 3.16 shows yields of nitrogen, M_{N}, obtained by several stellar calculations. Yield data other than this work are rotating models of Ekström et al. (2008) and $v_{\mathrm{ini}}/v_{\mathrm{k}} = 0.2$ models of Yoon et al. (2012). In my calculation, all rotating models produce nitrogen during the core helium burning phase. The nitrogen production is resulted from the transportation of seed materials by rotationally
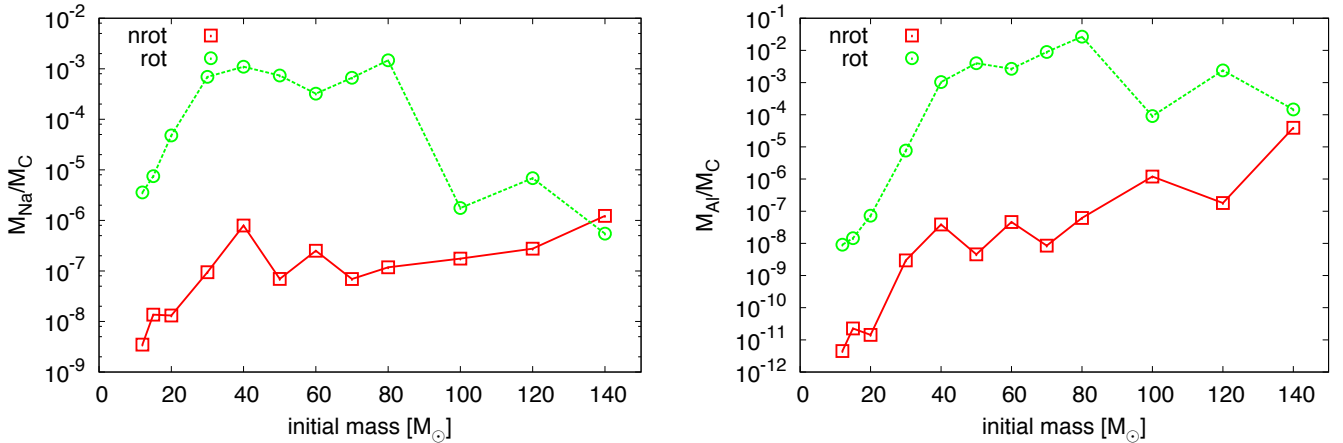
Figure 3.17: Same as Fig. 3.12, but for sodium (left) and for aluminum (right).

induced mixing. Thus, I confirm the primary nitrogen production in this work. Since almost all of the nitrogen is distributed in hydrogen and helium layers at the last stage of the evolution, the graph shows the total yields of nitrogen in the calculations. Similarly, models of Ekström et al. (2008) show the enhancement of nitrogen. On the other hand, not much enhancement is seen in the models by Yoon et al. (2012), suggesting the uncertainty of treatment of stellar rotation. Note that nitrogen production can be seen in some models with initial masses of 15 and 20 $M_\odot$ even for non-rotating cases. This nitrogen production is due to hydrogen ingestion discussed in an earlier section.

The primary nitrogen firstly distributes both in the hydrogen envelope and in the outer region of the helium core. For nitrogen in the hydrogen envelope, matter mixing transports nitrogen enriched material from the base of the hydrogen burning shell to the hydrogen envelope. The mixing processes are rotation induced mixing for less massive stars of ≤ 30 $M_\odot$, or convective mixing in a small convective region that appears in the early core helium burning phase for massive stars of ≥ 40 $M_\odot$. For nitrogen in the outer region of the helium core, matter accretion onto the helium core accounts for the nitrogen enrichment. During the core helium burning phase, hydrogen shell burning increases the mass of the helium core. The accreting matter has a large abundance of nitrogen, and all rotating models form nitrogen-rich helium layers at the end of the core helium burning phase. Nitrogen in the helium layer accounts for the nitrogen yield for less massive models of $\leq$ 20 $M_\odot$. On the other hand, for massive models of ≥ 30 $M_\odot$, most nitrogen in the helium layer is converted into ^{22}Ne in later evolution stages (see the next subsection.), and do not contribute to the nitrogen yield.

3.3.5 Sodium and Aluminum

The production ratios of sodium and aluminum are shown in two panels of Fig. 3.17. These figures clearly show the enhancement of sodium and aluminum in the outer region of rotating first stars. I find that the enhancement of sodium and aluminum

is attributed to the neutron capture reactions, which only takes place in the helium layer of a rotating model.

At first, as a result of the rotationally induced mixing, ^{14}N exists in a helium layer in rotating models. Then, alpha capture reactions produce ^{22}Ne from ^{14}N as

$$^{14}\text{N}(\alpha, \gamma)^{18}\text{F}(,\beta^+\nu_\text{e})^{18}\text{O}(\alpha, \gamma)^{22}\text{Ne}.$$
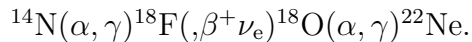
The ^{22}Ne is a well-known neutron source in massive star evolution. A free neutron is emitted by another alpha capture on ^{22}Ne as

$$^{22}\text{Ne}(\alpha, \text{n})^{25}\text{Mg}.$$
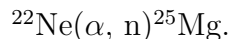
Finally, when the neutron is absorbed by seed elements of ^{22}Ne, ^{25}Mg, and ^{26}Mg, ^{23}Na and ^{27}Al are produced as

$$^{22}\text{Ne}(\text{n}, \gamma)^{23}\text{Ne}(,\beta^-\bar{\nu}_\text{e})^{23}\text{Na},$$
$$(^{25}\text{Mg}(\text{n}, \gamma))\ ^{26}\text{Mg}(\text{n}, \gamma)^{27}\text{Mg}(,\beta^-\bar{\nu}_\text{e})^{27}\text{Al}.$$
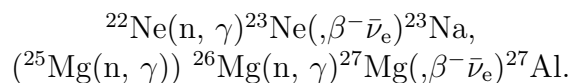
Sodium and aluminum productions also take place in a hydrogen burning shell of rotating models. These are due to the Ne-Na and the Mg-Al chains, since tiny fractions of neon and magnesium are transported from the base of the helium layer to the hydrogen burning shell by rotationally induced mixing (Maeder et al., 2015; Choplin et al., 2016). However, in my calculation, sodium and aluminum production by these proton capture reactions is much less effective than the n-capture processes explained above.

Both the production ratios of sodium and aluminum have very similar dependence on the initial mass. For less massive stars of $\lesssim 40$ M$_\odot$, these production ratios show steep increase with the initial mass. There is a plateau in the range from 40 M$_\odot$ to 80 M$_\odot$. And these odd elements are less produced in the most massive stars of $\gtrsim 100$ M$_\odot$. These trends in the initial mass are due to the temperature dependence of related nuclear reactions. The lower production in less massive stars can be understood as follows: The alpha capture by ^{22}Ne requires a temperature higher than $\sim 10^{8.6}$ K, thus less massive stars do not have a sufficiently large flux of neutrons. In addition, less massive stars do not have sufficiently abundant ^{24}Mg as the seed element of ^{25}Mg, since the alpha capture by ^{20}Ne requires a temperature higher than $\sim 10^{8.7}$ K. This reduces aluminum production. On the other hand, lower production in massive stars of $\gtrsim 100$ M$_\odot$ is attributed to efficient destruction reactions. Alpha capture by ^{23}Na reduces sodium production, and alpha captures by ^{25}Mg and ^{26}Mg, seed elements of ^{27}Al, reduce aluminum production.

In summary, a rotating model with an intermediate initial mass of 30–80 M$_\odot$ shows efficient production of sodium, and a rotating model with an intermediate initial mass of 40–80 M$_\odot$ shows efficient production of aluminum. Thus, these odd elements are useful to prove the existence of rotationally induced mixing in the progenitor.

3.4   Conclusion of this chapter

The purpose of this chapter is to obtain new knowledge of the abundance patterns of first supernova yields, which can be used to constrain the progenitor characteristics. I have calculated Pop III stellar evolution in a wide range of initial parameters. The initial mass range is set from 12 to 140 $M_\odot$ to cover the wide likely mass range of CCSNe. Stellar rotation is newly included in the progenitor calculation, resulting in diverse nucleosynthesis due to efficient internal matter mixing. The stellar yields are calculated by the weak supernova model, which will provide applicable yields to explain abundances of CEMP stars.

I have found that various abundance distributions arise in outer shell helium regions in calculated models. Massive models of ≥ 40 $M_\odot$ for rotating and ≥ 60–80 $M_\odot$ for non-rotating cases show both magnesium and silicon enhancement in their helium layers. These enhancements are due to efficient alpha capture reactions in the region. As for rotating models, owing to rotationally induced mixing, abundant nitrogen is produced in the hydrogen burning shell at first. Alpha capture reactions onto nitrogen take place in later evolutionary phases, resulting in neutron emission and nucleosynthesis of sodium and aluminum. For non-rotating massive stars of ≥ 80 $M_\odot$, calcium production occurs in the hydrogen burning shell, owing to the break-out of the CNO cycle. These characteristics are well reflected in the stellar yields. The new findings will be useful to deduce the properties of source stars, which existed in the early universe.

Chapter 4

Yields of Pop III PISNe

In this chapter, besides the detailed discussion of how to treat the energy conservation in an exploding star, the mechanism of PISN explosion and the nucleosynthesis results are described[1].

A possibility to obtain an explosion owing to the hydrodynamical collapse induced by electron-positron pair production has been firstly pointed out by Barkat et al. (1967) and Rakavy et al. (1967). The explosion is now called pair-instability-supernova. Two key reactions are responsible for the explosion. The first is a creation reaction of electron-positron pair that reduces the pressure and induces the dynamical collapse of a CO core, and the second is a thermonuclear reaction of oxygen burning that effectively heats the core and supplies energy to reverse the motion from collapse to explosion. Firstly, I discuss in detail how these energetics can be treated in a simulation to accurately determine the initial mass range for PISNe. Then the systematic Pop III PISN calculations are conducted, following the evolution from the hydrogen burning phase to the explosion, for the first time.

Theoretical investigation of PISN has been driven by an expectation that their outstanding properties, such as a high explosion energy and a peculiar yield pattern, may enable the observational identification of the hidden properties of the far-away universe (e.g., Umeda & Nomoto, 2002; Heger & Woosley, 2002). In particular, owing to the high explosion energies and/or the large ^{56}Ni yields that make the explosion luminous, PISN is one of the most promising candidates as an observable object at high redshift (Scannapieco et al., 2005; Kasen et al., 2011; Kozyreva et al., 2014a,b; Chatzopoulos et al., 2015; Whalen et al., 2013; Smidt et al., 2015).

According to the most recent study of simulation of first star formation, a large fraction of first stars is born having initial masses of several tens to several hundreds of solar masses (Hirano et al., 2014, 2015). The mass range for the PISN explosion is fully covered by the theoretical prediction. Hence, from the simulations, a large number of PISNe are expected to have happened in the early universe. If a PISN explosion took place in reality, low mass stars might have been born from the metal-enriched gas by the PISN ejecta. And one may observe such a PISN child as an old metal poor star in our Galaxy. Therefore, I calculate the nucleosynthesis

---

[1]Analysis of energy generation rates and results of explosion simulations have been reported in (Takahashi et al., 2016).

in PISNe for the abundance profiling of the metal poor stars. The purpose of this chapter is, first, to find a nucleosynthetic signature of PISN, which can be used to discriminate a PISN-child star by comparing the surface abundance pattern, and moreover, to understand the mass dependency of the nucleosynthesis, in order to further constrain the initial mass of the source star of the PISN children.

4.1   Energy generation rates

Before starting the discussion of PISN mechanism and yields, here I emphasize the importance of understanding how the energy conservation is treated in a simulation code. Energetics of nuclear reaction is fundamentally important to understand the mechanism of PISNe. Based on the equation of one dimensional hydrodynamics, classical textbooks often formalize energy conservation with three kinds of energy generation rates:

$$\frac{\partial L}{\partial M} = \epsilon_{\mathrm{grv}} + \epsilon_{\mathrm{nuc}} - \epsilon_{\nu}, \tag{4.1}$$

where ϵ_{grv}, ϵ_{nuc}, and ϵ_{ν} are the so-called gravothermal energy generation rate, the nuclear energy generation rate, and the neutrino cooling rate, respectively (Chiu, 1968; Cox, 1968; Kippenhahn & Weigert, 1990; Iben, 2013). In order to obtain the complete expression of this equation, definitions of individual energy generation rates should be given explicitly. However, In the literature, such definitions are often omitted or given with some implicit assumptions. If little attention is paid to these points, physically incorrect energy generation rates might produce erroneous results in simulation.

For example, as noted in Cox (1968), if one firstly defines ϵ_{grv} as

$$\epsilon_{\mathrm{grv}} \equiv -\frac{\partial e}{\partial t} - p\frac{\partial(1/\rho)}{\partial t}, \tag{4.2}$$

equating with the first law of the thermodynamics, this reduces to another expression of

$$\epsilon_{\mathrm{grv}} = -T\frac{\partial s}{\partial t} - \frac{1}{m_u}\sum_{\mathrm{particles}} \mu_i\frac{\partial Y_i}{\partial t}. \tag{4.3}$$

If one assumes that the second term on the right hand side is negligibly small, this equation becomes

$$\epsilon_{\mathrm{grv}} = -T\frac{\partial s}{\partial t}, \tag{4.4}$$

which coincides with the formula given in Chiu (1968) and Kippenhahn & Weigert (1990). As for the nuclear energy generation rate, the general definition is more difficult to find[2]. One may define ϵ_{nuc} using the Q-value and the reaction rate λ

$$\epsilon_{\mathrm{nuc}} \equiv \sum_{\mathrm{reactions}} Q_i\lambda_i \tag{4.5}$$

---

[2]Eq. 8.5 in Kippenhahn & Weigert (1990) may provide this.

as a straightforward generalization of that for the pp-chain or the CNO-cycle that are often discussed in detail. In this case, the Q-value must contain the rest masses (and the average energy for neutrino) of *all* particles involved in the reaction, and the summation must run for *all* reactions occurring.

In the following, based on the hydrodynamic equations and thermodynamic relations, I derive exact expressions for energy conservation suitable to be solved in simulations. Then, some formulae commonly used in the literature are shown to be obtained as approximations of the exact expressions. Later, I demonstrate that the explosion properties of PISN, such as the mass range, the ^{56}Ni yield, and the explosion energy, are significantly affected by applying the different energy generation rates.

4.1.1 Exact expressions of the energy generation rates

I begin the discussion with the energy equation in the stellar equations,

$$\frac{\partial e^{\mathrm{rel}}}{\partial t} = -p\frac{\partial(1/\rho_{\mathrm{b}})}{\partial t} - \frac{\partial L}{\partial M_{\mathrm{b}}} + \epsilon_\nu, \tag{4.6}$$

where $\rho_{\mathrm{b}} \equiv m_u n_{\mathrm{b}}$ is the baryon density defined as the product of the atomic mass unit and the baryon number density, and $\rho_{\mathrm{b}}e^{\mathrm{rel}}$ is the relativistic internal energy per unit volume. Note that this energy equation does not include the energy generation rate by the nuclear reactions, ϵ_{nuc}. This is because nuclear reactions just transform the form of the internal energy from the rest mass to thermal motion of gas particles. On the other hand, ϵ_ν is included since neutrinos are not in thermal equilibrium with stellar gas and the energy of neutrinos are excluded from the internal energy. This equation coincides with eq.(4.1), if ϵ_{grv} and ϵ_{nuc} are correctly defined as

$$\epsilon_{\mathrm{grv}}^{\mathrm{base}} \equiv -\frac{\partial e^{\mathrm{rel}}}{\partial t} - p\frac{\partial(1/\rho_{\mathrm{b}})}{\partial t}, \tag{4.7}$$

$$\epsilon_{\mathrm{nuc}}^{\mathrm{base}} \equiv 0. \tag{4.8}$$

Hereafter we refer to these definitions as the *base expression* of energy conservation.

Next, I define the thermal component of the internal energy density as

$$\rho_{\mathrm{b}}e^{\mathrm{therm}} \equiv \rho_{\mathrm{b}}e^{\mathrm{rel}} - \rho c^2, \tag{4.9}$$

in which ρ is the rest mass density (A.12). According to eq.(A.13), the change of the rest mass per baryon is expressed as

$$\mathrm{d}\left(\frac{\rho c^2}{\rho_{\mathrm{b}}}\right) = \frac{1}{m_u}\left[\sum_{\mathrm{ion}} m_i c^2 \mathrm{d}Y_i + m_e c^2 \mathrm{d}Y_e + 2m_e c^2 \mathrm{d}Y_{e^+}\right], \tag{4.10}$$

where m_i and Y_i are the rest mass and the mole fraction of i-th ion, m_e is the electron mass, $Y_e = Y_{e^-} - Y_{e^+}$ is the net electron mole fraction, and Y_{e^-} and Y_{e^+} are the electron and positron mole fractions (see the appendix A.1 for detailed

definitions). Equating eqs.(4.6, 4.9, 4.10), one obtains an alternative expression of energy conservation as

$$\frac{\partial L}{\partial M_{\rm b}} = \epsilon_{\rm grv}^{\rm reac} + \epsilon_{\rm nuc}^{\rm reac} - \epsilon_\nu, \tag{4.11}$$

where I momentarily identify the energy generation rates as

$$\epsilon_{\rm grv}^{\rm reac} \equiv -\frac{\partial e^{\rm therm}}{\partial t} - p\frac{\partial(1/\rho_{\rm b})}{\partial t} \tag{4.12}$$

$$\epsilon_{\rm nuc}^{\rm reac} \equiv -\frac{1}{m_u}\left[\sum_{\rm ion} m_i c^2 \frac{\partial Y_i}{\partial t} + m_e c^2 \frac{\partial Y_e}{\partial t} + 2m_e c^2 \frac{\partial Y_{e^+}}{\partial t}\right]. \tag{4.13}$$

This expression, though it is equivalent to the base expression, is more suitable for intuitive understanding of the effect of reactions, since the thermal part of the internal energy is affected by $\epsilon_{\rm nuc}^{\rm reac}$, which is directly related to the compositional change due to reactions. On the other hand, since one has to evaluate Fermi-Dirac integrals to obtain Y_{e^+}, this formula is not feasible to be applied to a numerical simulation.

One practical solution to take account for the change of the rest mass of electron-positron pairs is including the rest mass of that particular particles into the internal energy of the EOS (Blinnikov et al., 1996; Timmes & Swesty, 2000). Thus, the internal energy in a stellar code is often defined as

$$\rho_{\rm b} e^{\rm therm+pair} \equiv \rho_{\rm b} e^{\rm therm} + \rho_{\rm pair} c^2 \tag{4.14}$$

$$= \rho_{\rm b} e^{\rm therm} + 2m_e c^2 n_{e^+}, \tag{4.15}$$

then the equivalently exact expression, which we call the *reaction expression*, is derived:

$$\epsilon_{\rm grv}^{\rm reac} \equiv -\frac{\partial e^{\rm therm+pair}}{\partial t} - p\frac{\partial(1/\rho_{\rm b})}{\partial t} \tag{4.16}$$

$$\epsilon_{\rm nuc}^{\rm reac} \equiv -\frac{1}{m_u}\left[\sum_{\rm ion} m_i c^2 \frac{\partial Y_i}{\partial t} + m_e c^2 \frac{\partial Y_e}{\partial t}\right]. \tag{4.17}$$

This expression does no longer include the term of Y_{e^+}. Similar treatments can be found in some stellar codes that is used for massive stellar evolution calculation (private communication, Woosley 2015, Heger 2015, Langer 2015, Timmes 2015).

The other way to eliminate the term of Y_{e^+} is to treat the entropy equation instead. This approach guarantees a fluid element evolves adiabatically when the energy flux and reactions are negligible. Moreover, this has an advantage to calculate a thermal structure of degenerate objects like white dwarfs, in which pressure and internal energy scarcely depend on temperature. The entropy equation is obtained by equating the one-dimensional energy conservation (eq.4.6) with the first law of thermodynamics in the form of specific density,

$$de^{\rm rel} = Tds - pd\left(\frac{1}{\rho_{\rm b}}\right) + \frac{1}{m_u}\sum_{\rm particles} \mu_i^{\rm rel} dY_i, \tag{4.18}$$

where T is the temperature, $\rho_{\mathrm{b}}s$ is the entropy per unit volume, and μ_i^{rel} is the relativistic chemical potential (including the rest mass) of i-th particle (see appendix A.2). Since the reaction equilibrium is always established for the pair creation-annihilation reactions, the relation $0 = \mu_{e^+}^{\mathrm{rel}} + \mu_{e^-}^{\mathrm{rel}}$ is satisfied. Then one obtains

$$\frac{\partial L}{\partial M_{\mathrm{b}}} = -T\frac{\partial s}{\partial t} - \frac{1}{m_u}\Big[\sum_{\mathrm{ion}} \mu_i^{\mathrm{rel}}\frac{\partial Y_i}{\partial t} + \mu_e^{\mathrm{rel}}\frac{\partial Y_e}{\partial t}\Big] - \epsilon_\nu. \tag{4.19}$$

This equation does not include the term of Y_{e^+}, and thus can be evaluated only using ionic mole fractions. As for the definitions of the energy generation rates, an ambiguity exists. If one defines $\epsilon_{\mathrm{nuc}}^{\mathrm{ent}}$ to account for the heat generated by reactions, the following *entropy expression* can be defined,

$$\epsilon_{\mathrm{grv}}^{\mathrm{ent}} \equiv -T\frac{\partial s}{\partial t}, \tag{4.20}$$

$$\epsilon_{\mathrm{nuc}}^{\mathrm{ent}} \equiv -\frac{1}{m_u}\Big[\sum_{\mathrm{ion}} \mu_i^{\mathrm{rel}}\frac{\partial Y_i}{\partial t} + \mu_e^{\mathrm{rel}}\frac{\partial Y_e}{\partial t}\Big]. \tag{4.21}$$

4.1.2 Approximate expressions of the energy generation rates

In addition to above equivalently exact expressions, here I derive two approximate expressions, which are often found in the literature and, we are afraid, may have been employed in actual simulations.

Firstly, if one neglects the last term of eq.(4.13), then the reaction expression becomes

$$\tilde{\epsilon}_{\mathrm{grv}}^{\mathrm{reac}} \equiv -\frac{\partial e^{\mathrm{therm}}}{\partial t} - p\frac{\partial(1/\rho_{\mathrm{b}})}{\partial t}, \tag{4.22}$$

$$\tilde{\epsilon}_{\mathrm{nuc}}^{\mathrm{reac}} \equiv -\frac{1}{m_u}\Big[\sum_{\mathrm{ion}} m_i c^2\frac{\partial Y_i}{\partial t} + m_e c^2\frac{\partial Y_e}{\partial t}\Big]. \tag{4.23}$$

This *approximate reaction expression* is easy to evaluate similar to $\epsilon_{\mathrm{nuc}}^{\mathrm{ent}}$ and coincides with the exact one if positron is essentially non-existent. Thus, to investigate evolution of low mass stars or early stages of massive stellar evolution, this expression provides accurate enough energy generation rates, and this is why the expression is utilized in some stellar evolution codes (e.g. in GENEC, Meynet 2015, private communication.) On the other hand, this expression overestimates the nuclear energy generation rate when electron-positron pairs are created, since the neglected positron term accounts for the energy reduction due to pair creation. Correspondingly the nuclear energy generation rate is underestimated when the pair annihilation occurs.

Next, the other approximate expression is derived from the exact entropy expression, in which the thermal contribution of the chemical potential $\mu_i^{\mathrm{therm}} \equiv$

$\mu_i^{\rm rel} - m_i c^2$ is neglected:

$$\tilde{\epsilon}_{\rm grv}^{\rm ent} \equiv -T\frac{\partial s}{\partial t}, \tag{4.24}$$

$$\tilde{\epsilon}_{\rm nuc}^{\rm ent} \equiv -\frac{1}{m_u}\Big[\sum_{\rm ion} m_i c^2\frac{\partial Y_i}{\partial t} + m_e c^2\frac{\partial Y_e}{\partial t}\Big]. \tag{4.25}$$

This *approximate entropy expression*, hence, coincides with the exact one when the thermal contribution to the chemical potential is negligibly small compared with the rest mass. (Equivalent formalisms are used in, e.g., Hayashi et al. 1962; Paxton et al. 2011, and in Chieffi 2015, private communication). Meanwhile, our calculations show that this expression overestimates the nuclear energy generation rate in general.

It is noteworthy that, though totally different assumptions are treated in each expression, the appearance of the nuclear energy generation rates of the exact reaction expression (eq.4.17), the approximate reaction expression (eq.4.23), and the approximate entropy expression (eq.4.25) are in complete agreement with each other. Thus, it is necessary to exhibit the definition of both the so-called gravothermal energy generation rate and the nuclear energy generation rate in order to illustrate what kind of physics are really treated in the simulation.

4.2 Computational settings

I calculate the evolution and subsequent explosion of zero-metallicity non-rotating very massive stars having initial masses of $\sim$ 140–320 $M_\odot$. Properties and fates of calculated models are listed in Table 4.1. Hydrostatic evolution from the hydrogen burning until the end of the helium burning is calculated by the stellar evolution code. The evolutionary properties are very similar to that of massive end of CCSN progenitors ($\sim$ 100–140 $M_\odot$) and are not described here in detail. Later evolution including explosion is calculated by the hydrodynamic code. Finally, the explosive yield is obtained by a post-process calculation.

For the explosion simulation, mainly two different expressions of energy generation rates are applied. The first one is the exact entropy expression (eqs.4.20, 4.21). Hereafter, we refer to this group of calculations as the case A calculations. The second expression is the approximate entropy expression (eqs.4.24, 4.25). These calculations are referred to the case B calculations. Note that the luminosity term is neglected in the energy equation, since the other terms overwhelm the luminosity term for the short timescale evolution.

In order to determine the minimum mass of PISN, additional hydrodynamic calculations are conducted for less massive models of $\sim$ 140–150 $M_\odot$. The distributions obtained by an explosion calculation is mapped onto the time-explicit Lagrangian hydrodynamic code (Colella & Woodward, 1984; Umeda & Nomoto, 2002), and further expansion is calculated. The same EOS, nuclear reaction network, and neutrino cooling formulae are implemented. Based on the calculation, a star whose central region does not fall back into the center at 10^5 sec after the

Table 4.1: Properties of Pop III PISN models

				Case A				Case B			
$M_{\rm ini}$	$M_{\rm He}$	$M_{\rm CO}$	C/O	$E_{\rm tot}$	$M_{^{56}\rm Ni}$	$\log T_{\rm max}$	fate	$E_{\rm tot}$	$M_{^{56}\rm Ni}$	$\log T_{\rm max}$	fate
140	75.2	64.9	0.130	-	-	-	PPISN	-	-	-	PPISN
145	78.2	68.6	0.126	11.30	0.095	9.562	PISN	9.46	0.011	9.531	PISN
150	79.9	71.3	0.125	14.05	0.154	9.571	PISN	12.76	0.038	9.544	PISN
155	82.2	73.6	0.119	16.94	0.263	9.583	PISN	15.02	0.063	9.550	PISN
160	79.7	75.8	0.128	18.50	0.375	9.592	PISN	16.51	0.086	9.556	PISN
180	91.1	86.7	0.121	33.46	3.778	9.642	PISN	30.97	0.555	9.595	PISN
200	98.9	94.7	0.114	42.58	9.401	9.677	PISN	40.48	2.049	9.621	PISN
220	104.1	100.9	0.112	53.88	14.52	9.694	PISN	46.69	3.384	9.632	PISN
240	107.9	106.8	0.105	56.08	19.85	9.717	PISN	55.15	5.895	9.648	PISN
260	121.9	119.3	0.102	81.91	42.21	9.806	PISN	76.76	16.26	9.691	PISN
265	122.9	119.5	0.102	-	-	-	BH	78.82	18.07	9.699	PISN
270	127.1	123.2	0.100	-	-	-	BH	85.56	22.70	9.715	PISN
275	128.4	124.9	0.098	-	-	-	BH	86.78	23.23	9.717	PISN
280	131.4	127.8	0.097	-	-	-	BH	91.12	26.19	9.726	PISN
300	140.3	137.2	0.093	-	-	-	BH	109.2	45.21	9.808	PISN
320	145.6	142.3	0.090	-	-	-	BH	-	-	-	BH

Notes. $M_{\rm ini}$, $M_{\rm He}$, and $M_{\rm CO}$ are the initial mass, the helium core mass, and the carbon-oxygen core mass, C/O is the ratio between mass fractions of carbon and oxygen in the CO core, $E_{\rm tot}$, $M_{^{56}\rm Ni}$, and $T_{\rm max}$ are the explosion energy, the ejected ^{56}Ni mass, and the maximum temperature reached during the explosion, respectively. The fate is specified from PPISN, PISN, or black hole formation (BH). Masses are in $M_\odot$, the total energies are in 10^{51} erg, and $T_{\rm max}$ are in K.

explosion is considered to become a PISN. Otherwise, the fate is identified as a pulsational pair instability supernova (PPISN, Barkat et al., 1967; Heger & Woosley, 2002; Yoshida et al., 2016).

For case A exploding models, their explosive nucleosynthesis is calculated by a post processing manner. Data is taken for each Lagrange mesh, recording the change of the density and the temperature with time. Then the composition evolution of extended 300 isotopes is followed using the recorded density and temperature change. The considered isotopes are from neutron to ^{79}Br, shown by Tab. 2.1. The explosive yield is further processed by a decay calculation, in which additional 10^{10} yr is followed with the temperature of 10^3 K and the density of 10^{-10} g cm^{-3}.

4.3 Explosion of PISNe

4.3.1 Explosion mechanism

Fig. 4.1 shows evolution of central density and temperature for 200 and 280 $M_\odot$ case A models. The 200 $M_\odot$ model explodes as a PISN, while the 280 $M_\odot$ model collapses. The green lines show the boundaries of the adiabatic index $\gamma \leq 4/3$. This reduction of γ in the lower temperature region is due to the electron-positron pair creation. The creation of electron-positron pair does not change the entropy of the matter since the reaction is in equilibrium. On the other hand, the reaction changes the form of the energy from the thermal energy to the rest mass. Accord-
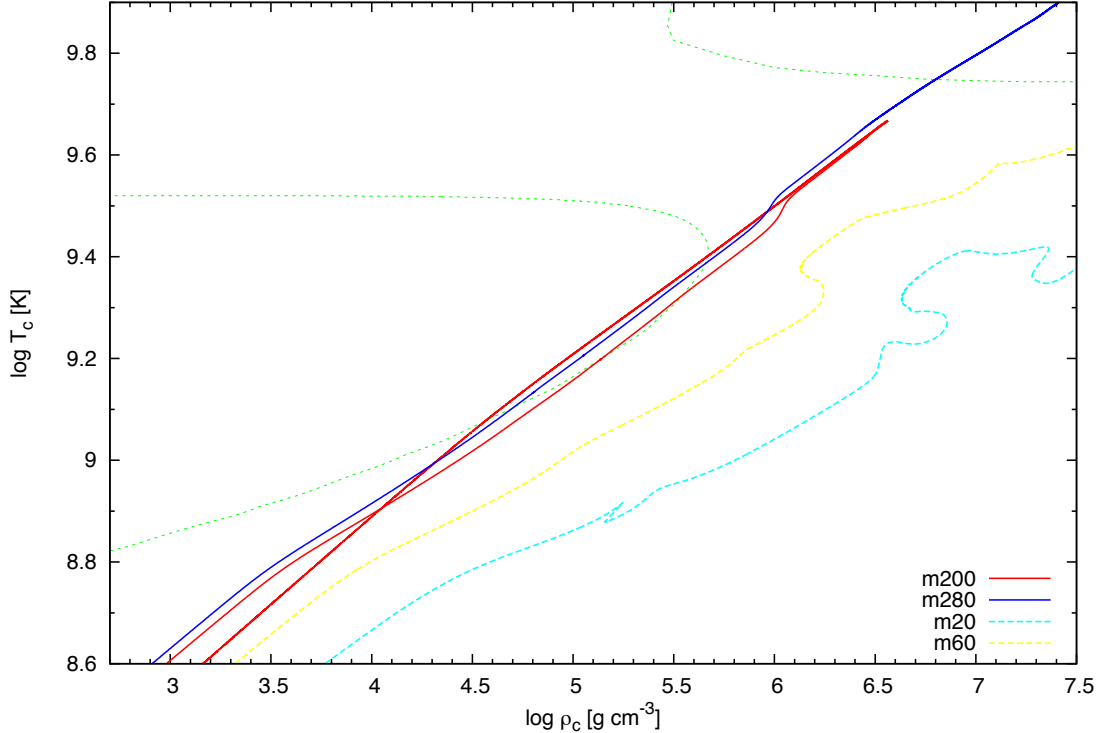
Figure 4.1: Evolutions of 200 and 280 $M_\odot$ very massive Pop III models are shown in the central density-temperature plane. The 200 $M_\odot$ model explodes as a PISN, while the 280 $M_\odot$ model collapses. Comparative Pop III models of 20 and 60 $M_\odot$ are additionally shown by dashed lines. Green dotted lines show the boundaries of the hydrodynamically unstable regions of $\gamma < 4/3$.

ingly, this reduces the pressure, and the adiabatic index falls below the critical value of 4/3.

Explosion properties are well correlated with the CO core mass, rather than the initial mass. If a star forms a massive enough CO core of $\gtrsim 65$ $M_\odot$, the stellar center enters into the unstable domain of the electron-positron pair creaction. The surrounding region in a core has a bit higher entropy than the center, because more effective neutrino cooling reduces the central entropy. Therefore, as the star contracts due to the central instability, the larger part of the core becomes unstable. The enhancement of the instability drives the runaway collapse of the massive CO core. As the collapse takes place within a short timescale, the temperature of the core almost adiabatically increases. During the collapse, carbon, neon, and then oxygen, ignites. The carbon and neon burnings have a small effect on the evolution, since mass fractions of carbon and neon, $\lesssim 0.1$, are small. Contrastingly, subsequent oxygen burning more effectively heats up the core. If the stellar core has a mass between $\sim$ 65–120 $M_\odot$, the increasing pressure by the carbon-oxygen burning halts the collapse and farther pushes the whole core back. If the core
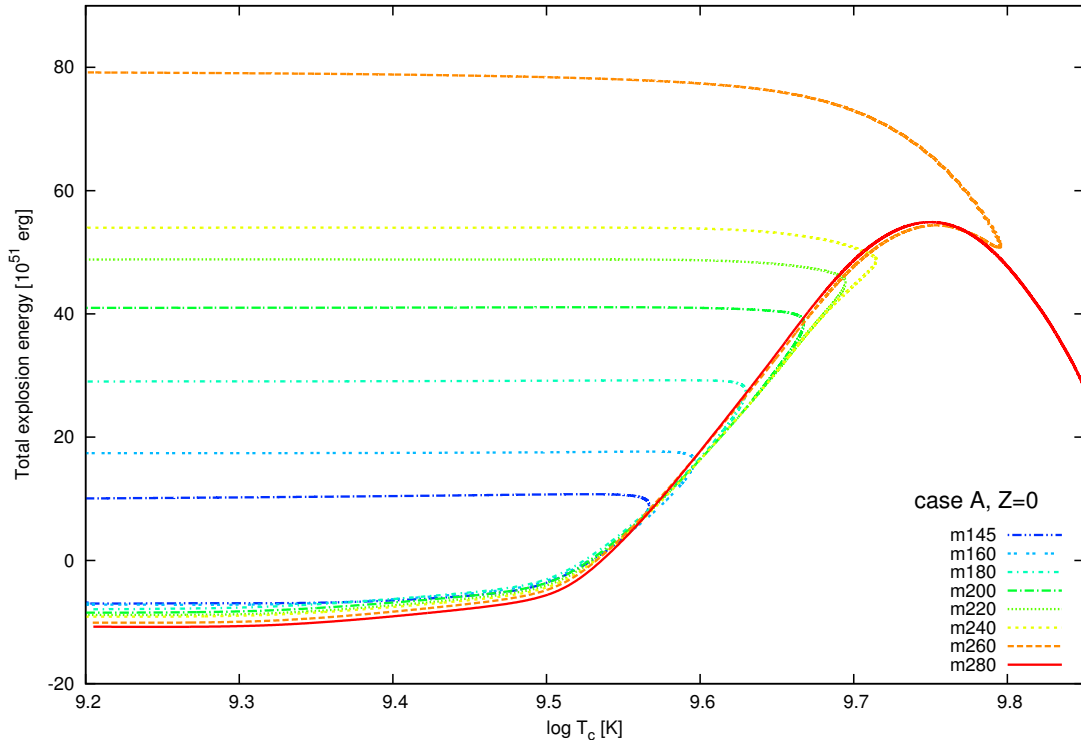
Figure 4.2: Evolution of total explosion energy with the central temperature. Selected models are 145, 160, 180, 200, 220, 240, 260, and 280 $M_\odot$ very massive Pop III models. While the most massive 280 $M_\odot$ model finally collapses, others explode as PISNe.

is more massive enough than ~ 120 $M_\odot$, on the other hand, the heating by the oxygen burning is insufficient to stop the collapse. The star keeps collapsing, being suffered by another instability of iron photo dissociation.

In Fig. 4.2, the evolution of the non-relativistic total energy as a function of the central temperature is shown for selected case A models. The total energy is defined as $\int(\frac{1}{2}U^2 + e^{\text{therm+pair}} - \frac{GM_b}{r})dM_b$, where U is the radial velocity of the gas, M_b is the enclosed baryon mass. This figure clearly shows that two reactions are responsible to determine the fate of the collapsing star. The first reaction is oxygen burning. The total energy rapidly increases after the ignition of the oxygen burning at $T_c \sim 10^{9.5}$ K. If oxygen burning supplies enough energy to invert the core motion, the core starts to expand. The explosion energy of a PISN becomes very large, which exceeds at least $\sim 10 \times 10^{51}$ erg and can be as large as $\sim 80 \times 10^{51}$ erg. On the other hand, the reduction of the total energy after the central temperature exceeds $\sim 10^{9.75}$ K is due to the iron photo-dissociation. As discussed earlier, the dissociation reaction softens the pressure in the same way as the pair creation reaction does. I find that the second hydrodynamical instability due to the photo-dissociation overcomes the heating effect of carbon-oxygen burning and
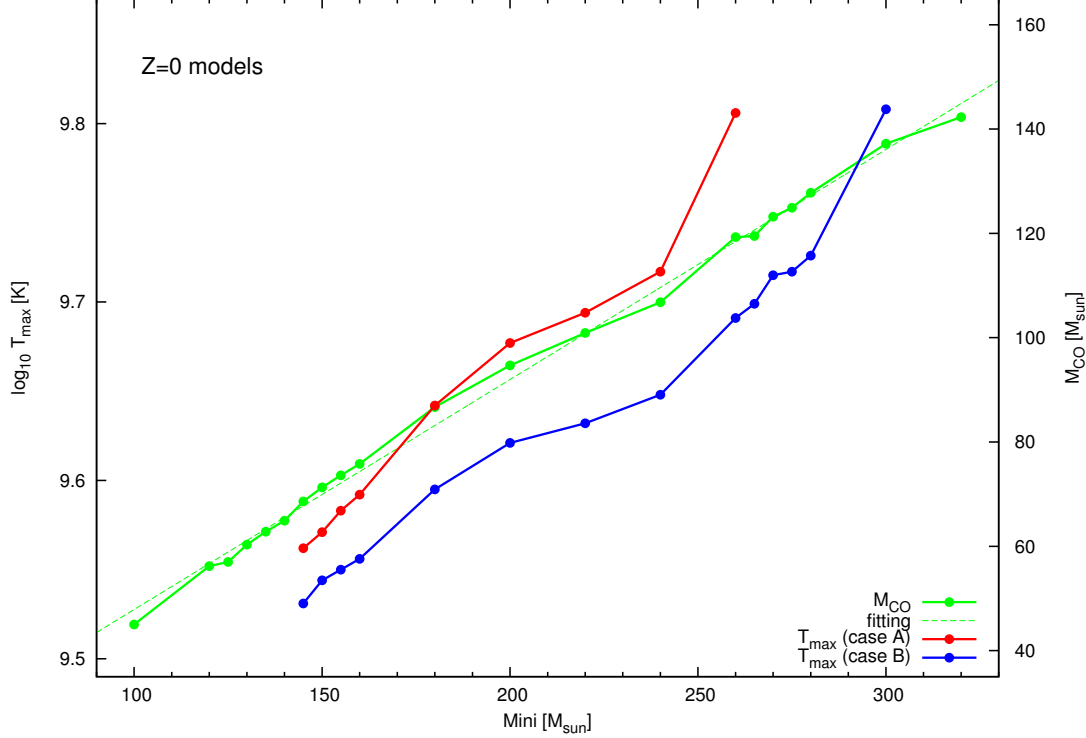
Figure 4.3: The maximum temperature reached during the explosion and the CO core mass as functions of the initial mass for all exploded models. The green dotted line is a fitting function for the CO core mass. For the maximum temperature, case A results are plotted by the red points and case B are by the blue points.

induces the final collapse, if the central temperature of the star once exceeds the critical value of $\sim 10^{9.8}$ K.

4.3.2 Impact of adopting different energy generation rates

By neglecting the thermal part in the chemical potential, the approximate entropy expression applied to the case B calculations overestimates the nuclear energy generation rate. In Figure 4.3, the maximum central temperature reached during the explosion, as well as the CO core mass, are shown as functions of the initial mass. This figure shows all case B models explode with lower central temperatures than the case A counterparts. The central temperature indicates how much amount of oxygen is consumed in the contracting CO core. In other words, the higher the central temperature is, the larger amount of oxygen are consumed. Hence, using the more efficient energy generation rate, the case B star explodes with a smaller amount of oxygen burned.

Being applied more effective energy generation, some massive stars that collapse with the exact energy generation rate become able to explode in the case B
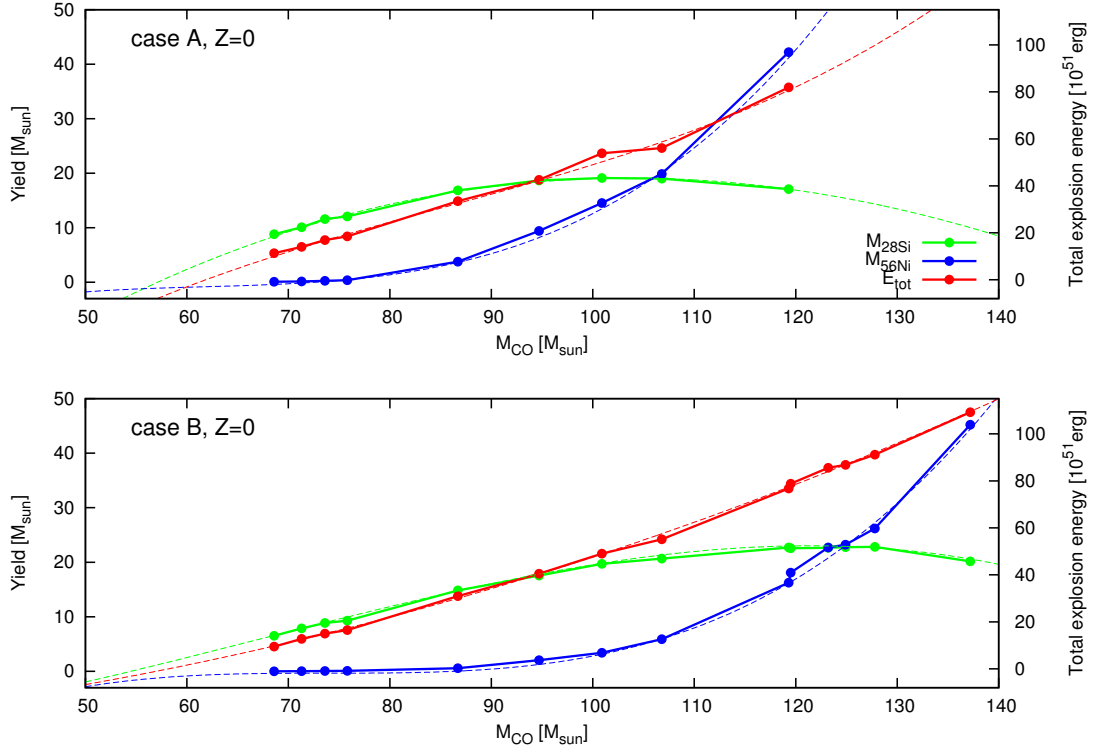
Figure 4.4: Yields of ^{28}Si (green) and ^{56}Ni (blue) and the total explosion energy as functions of the CO core mass for all exploded models. The top panel shows results of case A calculations and bottom shows that of case B. The green dotted lines show the fitting polynomials.

simulation. Fig. 4.4 shows that the maximum CO core mass for PISN extends from 119 M$_\odot$ to 137 M$_\odot$ by changing the definitions of energy generation rates. These figures also show that the explosion energy is roughly proportional to the CO core mass, and the dependence is almost identical in the two sets of calculations. As a result, the maximum explosion energy of PISN in case B becomes larger than the case A result. On the other hand, since the ^{56}Ni yield strongly depends on the maximum temperature, the most massive models for each set of calculations yield similarly largest amount of ^{56}Ni.

In Figure 4.5, yield comparison among four models, two from my calculation and the other two from Heger & Woosley (2002), are shown. With the exact entropy expression, yield of my zero metallicity 240 M$_\odot$ model shows almost the same composition pattern as the 110 M$_\odot$ helium star model by Heger & Woosley (2002). As both models have almost the same He core mass of $\sim$ 110 M$_\odot$, this agreement indicates the physical consistency of the two calculations. The only difference between the two is production of hydrogen, helium, lithium, and nitrogen in our model. These elements are produced at the base of the hydrogen envelope, which is omitted in the model by Heger & Woosley (2002). If the approximate
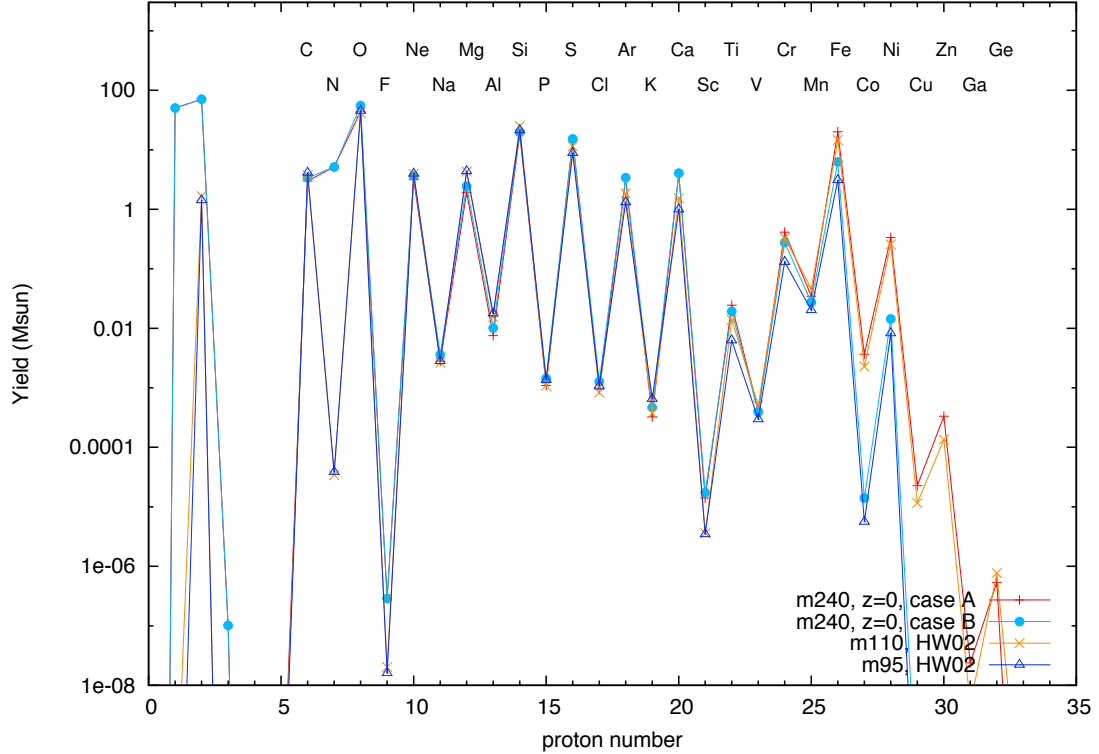
Figure 4.5: Composition patterns of PISN yields of different models. Red-plus patterns and cyan-point patterns show yields of case A and case B 240 M$_\odot$ calculations, respectively. Similarly, patterns shown by orange-cross and blue-triangle are yields of 110 M$_\odot$ and 95 M$_\odot$ helium star models taken by Heger & Woosley (2002).

entropy expression is applied to the same 240 M$_\odot$ star instead, the composition pattern is altered. Reflecting the lower temperature during the explosion at the central region, the case B 240 M$_\odot$ model yields smaller amount of heavy elements heavier than nickel. The composition pattern resembles the pattern of the 95 M$_\odot$ helium star model by Heger & Woosley (2002), however, the helium star mass is much smaller than the core mass of the 240 M$_\odot$ model.

Here I shortly conclude that, in order to accurately consider the energetics of reactions, the definition of energy generation rates in the hydrodynamic equation is fundamentally important. The energy generation rate of the approximate entropy expression, which is applied to the case B calculations, more effectively heats surroundings than the exact expression applied to the case A. As a result, the ^{56}Ni yield as a function of the CO core mass shifts to higher masses for the case B calculations. Moreover, the mass range for the PISN is extended in the case B simulations, from the fiducial range of 65–120 M$_\odot$ to the more wide range of 65–140 M$_\odot$ in terms of the CO core mass, and from 145–260 M$_\odot$ to 145–300 M$_\odot$ in terms of the initial mass. In the following, yield calculations are done using the
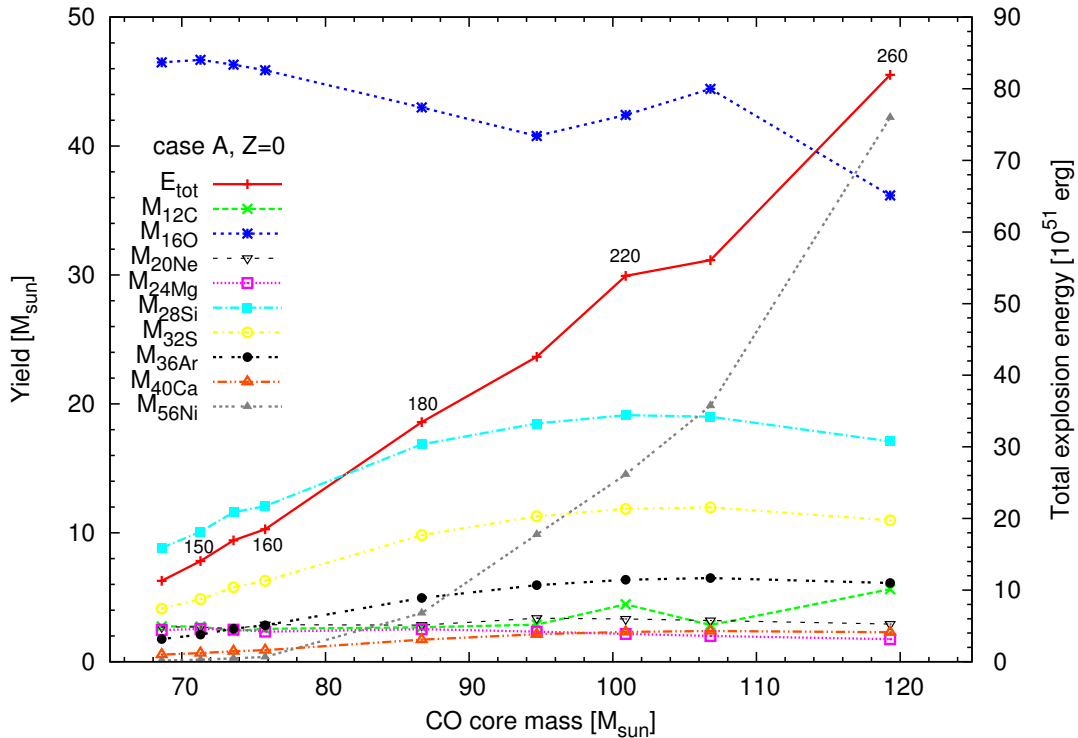
Figure 4.6: Yields and the total explosion energy as functions of the CO core mass. Models of 145, 150, 155, 160, 180, 200, 220, 240, and 260 $M_\odot$ are summarized. Numbers indicated near the total energy show the corresponding initial masses.

case A explosion results.

4.4   Yields of PISNe

In Fig. 4.6, the explosion energy as well as the yields of representative isotopes are summarized as functions of the CO core mass. While the explosion energy is roughly proportional to the CO core mass, the elemental yields have more complicated dependence. According to the dependence on the CO core mass, elements can be divided into three groups. The first group is hydrostatic burning products: lighter elements than aluminum. Their yields weakly depend on the CO core mass. The second group is oxygen burning products, which consist of isotopes heavier than silicon and lighter than calcium. Their yields have a peak at the intermediately massive CO core of ~ 100 $M_\odot$, while the ratio among them has a little dependency on the core mass. The last group is silicon burning products dominated by ^{56}Ni. For less massive models, almost no ^{56}Ni is produced by the explosion. Massive models, contrastingly, yield large amount of ^{56}Ni. More detailed elemental analyses are given below.
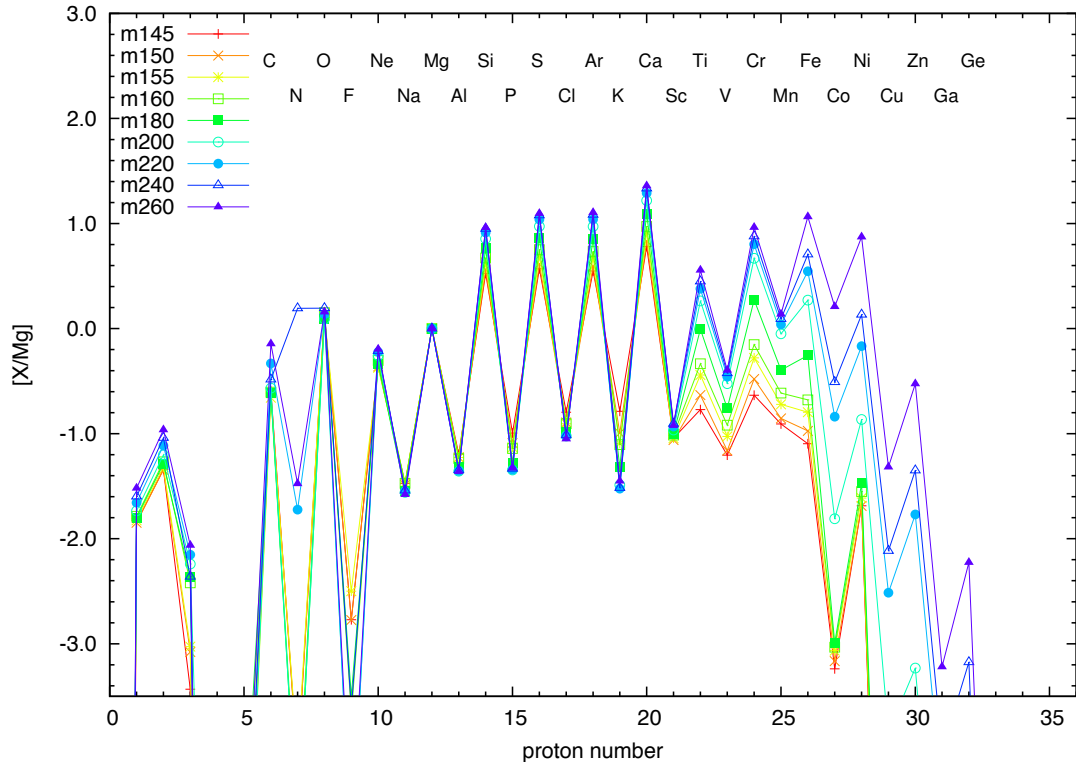
Figure 4.7: Abundance patterns of PISN yields. The abundance of magnesium is used for the normalization.

4.4.1 Carbon to aluminum

Fig. 4.7 shows abundance patterns of PISN yields in [X/Mg], taking the proton number as the x-axis. Abundances are normalized by the magnesium yield in this figure. This is because all of PISN models eject abundant magnesium, the magnesium yield has a small dependency on the CO core mass, and moreover a surface abundance of magnesium is obtained for most of the metal poor stars. This figure shows that lighter elements from carbon to aluminum except nitrogen are similarly produced by PISNe. Scatters of the abundance ratios are especially small for [O/Mg] = 0.09–0.19, [Ne/Mg] = −0.37–−0.19, [Na/Mg] = −1.58–−1.46, and [Al/Mg] = −1.36–−1.19. The large production of nitrogen in the 240 $M_\odot$ model is due to convective dredge-up during their late core helium burning phase, in which base of the surface convection reaches the surface of the CO core and mixes small amount of carbon and oxygen into the hydrogen rich envelope.

4.4.2   Silicon to calcium

Intermediate-mass elements of silicon to calcium are mainly produced by oxygen burning, and partially produced by neon and carbon burning. A well-known peculiarity of PISN yields can be seen here as a pronounced variance between odd-Z and even-Z elemental yields, which discriminates PISN yields from the usual CCSN yields (Heger & Woosley, 2002; Umeda & Nomoto, 2002). The odd-even variance is due to the high Y_e, or the high proton-to-neutron ratio, of PISN explosions. Since the pushing-back takes place within a short timescale, electron capture reactions are too slow to change the core Y_e. With the high proton-to-neutron ratio, the explosive nucleosynthesis favorably synthesizes even-Z elements.

Each PISN still shows a similar abundance pattern in these elements, however, the odd-even difference is much more pronounced in a more massive PISN explosion. In other words, yields of intermediate-mass elements depend on the core mass of the PISN, and furthermore, the opposite mass dependency between odd-Z and even-Z yields is found. Abundance ratios of even-Z elements are the lowest for the lightest 145 M$_\odot$ model and the highest for the most massive 260 M$_\odot$ model, e.g., [Si/Mg] = 0.52–0.96 and [Ca/Mg] = 0.78–1.35. On the other hand, that of odd-Z elements are the highest for the 145 M$_\odot$ model and the lowest for the 260 M$_\odot$ model, e.g., [K/Mg] = −1.52–−0.78.

4.4.3   Scandium to germanium

The heavy elements, from scandium to germanium, are synthesized in the innermost region of the star. Firstly, silicon burning takes place in this region, then it quickly develops into the NSE, in which baryons freely transform to attain the most stable state of the lowest free energy. The equilibrium is lifted when the star starts to expand. During the expansion, heavy elements are re-processed and further the unstable nuclei decay into stable nuclei.

The mass dependence of these elements is extremely large. The lowest mass 145 M$_\odot$ model yields smallest masses of these elements, for example, [Fe/Mg] = −1.09, [Co/Mg] = −3.23, [Ni/Mg] = −1.68, and [Zn/Mg] = −8.93. In contrast, the highest mass 260 M$_\odot$ model yields magnificently large amount of the heavy elements, [Fe/Mg] = 1.06, [Co/Mg] = 0.20, [Ni/Mg] = 0.87, and [Zn/Mg] = −1.31. Note that the abundance ratio [Sc/Mg], spanning from −1.06 to −0.91, shows a small scatter with changing the stellar initial mass.

The peculiarity of the abundance pattern is the large concentration on specific elements of chromium, iron, and nickel. As a result, a steep decline is observed around the proton number of 28–32. This can be indicated by the small abundance ratios of [Ni/Fe] or [Zn/Ni]. The largest proton number element produced by a PISN is germanium. The 260 M$_\odot$ model produces germanium of [Ge/Mg] = −2.22. No further massive elements are produced, thus [As, Se/Mg] < −9.

4.5 Conclusion of this chapter

Two key reactions are responsible for the PISN explosion dynamics. The first is the electron-positron pair creation, by which the dynamical collapse is triggered. The second is the oxygen burning, which efficiently heats up the core and explodes the star. I have pointed out the importance of the treatment of the energy generation rates in the stellar equation, and demonstrate that the explosion properties, especially the mass range for the PISN explosion, is severely affected by adopting approximate energy generation rates.

The explosive yield is calculated based on the explosion simulation using the exact formulation of the energy conservation. First, the pronounced odd-even variance is also confirmed in my calculation (Heger & Woosley, 2002). Furthermore, I have found that the elemental yield can be divided into three groups based on the mass dependencies. First group consists of lighter elements of carbon to aluminum. Their abundance pattern is almost constant with changing the initial mass of the star. In addition to the lighter elements, scandium shows similar constancy. Therefore, abundance ratios such as [Na/Mg], [Al/Mg], and [Sc/Mg] can be used as the first requirement for a hypothetical PISN child to exhibit. Deficiencies of them can be interpreted as realization of the odd-even variance. The second group, the intermediate-mass elements from silicon to calcium, is composed of products of oxygen burning. The odd-even variance in these elements is found to show the initial mass dependence. Thus the abundance patterns such as [Si/Mg] and [Ca/Mg] can be used as a potential probe to constrain the initial mass of the PISN source star. Finally, the heaviest elements from titanium to germanium show the strongest mass dependence. This is a generalizing statement of the strong mass dependence of Ni pointed by Umeda & Nomoto (2002). The steep decline around the proton number of 28–32, which can be indicated by abundance ratios of [Ni/Fe] or [Zn/Ni], can be used as the second requirement to search PISN children.

Chapter 5

Abundance profiling

In preceding chapters, I have pointed out some abundance patterns seen in the yields of first supernovae that characterize the properties of progenitor stars. Applying the weak supernova model, CCSN yields from 12–140 $M_\odot$ first stars are shown to exhibit peculiar abundance patterns synthesized in the helium layers. As for yields of PISNe occurring from more massive 145–260 $M_\odot$ stars, three groups of elements having different mass dependencies are found.

The main purpose of this chapter is to provide a proof of existence of at least some particular first stars, by conducting the *abundance profiling.* By gathering these examples, properties of first stars will be constrained. I conduct detailed comparisons between theoretical yields of Pop III massive stars and observations of surface abundance patterns of metal-poor stars. Metal-poor stars would be born from the chemically primitive gas clouds in the early universe. And the metal ejection by first stars would be responsible for the metal pollution. Thus the signatures of the first nucleosynthesis are expected to be imprinted in the surface abundance patterns of metal-poor stars in the local universe. Through the abundance comparison, the properties of the source stars can be obtained.

As an application of the weak supernova model, I aim to constrain the properties of source stars of the three most-iron-deficient stars discovered so far[1]. They are SMSS 0313-6708 of [Fe/H] < -7.1 (Keller et al., 2014), HE 0107-5240 of [Fe/H] $= -5.3$ (Christlieb et al., 2002), and HE 1327-2326 of [Fe/H] $= -5.7$ (Frebel et al., 2005). All of these stars are members of CEMP stars, having large carbon abundances compared to iron of [C/Fe] > 0.7. Moreover, they are also known to show enhancements in intermediate-mass elements, such as sodium, magnesium, and silicon. Therefore it is expected that a weak supernova model, which abundantly produces such intermediate-mass elements synthesized in the outer region of the progenitor, can provide a reasonable fitting.

In contrast to Pop III CCSNe, no candidate metal-poor stars have been discovered for PISN children except for the recent work by Aoki et al. (2014). The reason of the non-detection may be explained as a result of the observational bias. Because of the large metal yield, PISN children may be born having a relatively large [Ca/H] ~ -2.5, which can be missed from metal-poor star huntings utilizing

---

[1]Comparison with the three most-iron-deficient stars has been reported in Takahashi et al. (2014).

Table 5.1: Summary of abundance profiling

Object	[Fe/H]	$M_{\rm ini}$	$f_{\rm ej}$	Rotation	Dilution Factor
SMSS 0313-6708	< -7.1	50-80	0.96 ± 0.04 (60 M$_\odot$)	non-rotating	$1.78 \times 10^3 - 6.09 \times 10^2$
			0.98 ± 0.04 (80 M$_\odot$)	non-rotating	$1.62 \times 10^3 - 1.91 \times 10^2$
HE 0107-5240	-5.3	30-40	1.07 ± 0.06 (30 M$_\odot$)	rotating	$7.84 \times 10^2 - 2.23 \times 10^2$
HE 1327-2326	-5.7	20-40	0.96 ± 0.01 (40 M$_\odot$)	non-rotating	$5.00 \times 10^2 - 4.32 \times 10^2$
		15-30	0.93 ± 0.01 (20 M$_\odot$)	rotating	$7.92 \times 10^2 - 7.35 \times 10^2$

Table 5.2: Stellar yields of the best fit models

Object	$M_{\rm ini}$	Rotation	$f_{\rm ej}$	$M_{\rm SN}$	^{4}He	^{12}C	^{13}C	^{14}N	^{16}O	^{20}Ne	^{23}Na	^{24}Mg	^{27}Al	^{28}Si
SMSS 0313-6708	60	Nonrotating	0.96	37.3	1.70e1	3.05e-1	2.00e-8	2.13e-7	9.18e-1	5.81e-2	3.81e-8	6.88e-3	6.63e-9	4.90e-6
	80	Nonrotating	0.98	46.8	2.21e1	2.62e-1	3.08e-9	3.00e-7	6.09e-1	9.00e-2	1.50e-8	5.21e-2	6.39e-9	1.21e-3
HE 0107-5240	30	rotating	1.07	18.1	8.21e0	4.53e-2	4.25e-4	2.94e-4	6.20e-3	4.19e-5	3.09e-5	2.03e-5	2.56e-7	3.14e-7
HE 1327-2326	40	Nonrotating	0.96	25.5	1.09e1	1.86e-1	2.89e-8	1.09e-6	5.18e-1	2.08e-2	1.56e-4	1.45e-3	4.81e-5	5.01e-5
	20	rotating	0.93	14.2	5.94e0	1.59e-1	7.78e-3	1.18e-2	3.36e-1	1.83e-2	1.77e-4	1.20e-3	3.81e-5	4.11e-5

Notes. The first column shows the object name, from second to fourth columns show the initial mass, the inclusion of rotation, and the adopted $f_{\rm ej}$ of the model. The rest show total mass of the ejecta and ejected mass of each element in solar mass units.

the CaII K line (Karlsson et al., 2008). However, a growing number of metal-poor stars have been discovered by recent observations (e.g., Hollek et al., 2011; Bonifacio et al., 2012; Cohen et al., 2013; Yong et al., 2013b; Roederer et al., 2014). Also it is noteworthy that the systematic observation to find the PISN signatures in metal-poor stars is now undertaken (Ren et al., 2012).

Therefore, in this work, I conduct the first systematic comparison between PISN theoretical yields and observations using the big stellar abundance data compiled in *SAGA* database (**http://sagadatbase.jp/**, Suda et al. 2008, 2011; Yamada et al. 2013). The purpose of the comparison is, firstly, to confirm the (non-)existence of PISN signatures on the present metal-poor stellar sample, and secondly, to validate what are the fundamentally reliable and practically useful abundance ratios to discriminate PISN signatures. The possible discovery of PISN children provides a firm proof of the existence of very-massive first stars in the early universe.

5.1 Comparison with weak supernova yields

Hereafter, results of the abundance profiling to the three most-iron-deficient stars are discussed. The best fit models are listed in Table 5.1, showing initial masses and rotational characteristics of models for each star. In Table 5.2, the stellar yields of intermediate mass elements are summarized. In the following subsections, important characteristics of observed abundance patterns and how the best fit models are selected are presented.

5.1.1 SMSS 0313-6708

A dwarf halo star, SMSS 0313-6708, discovered by Keller et al. (2014), is the most iron-deficient star discovered so far. Amazingly enough, the high resolution spectroscopy could not detect iron emission lines from the stellar surface. Thus only the
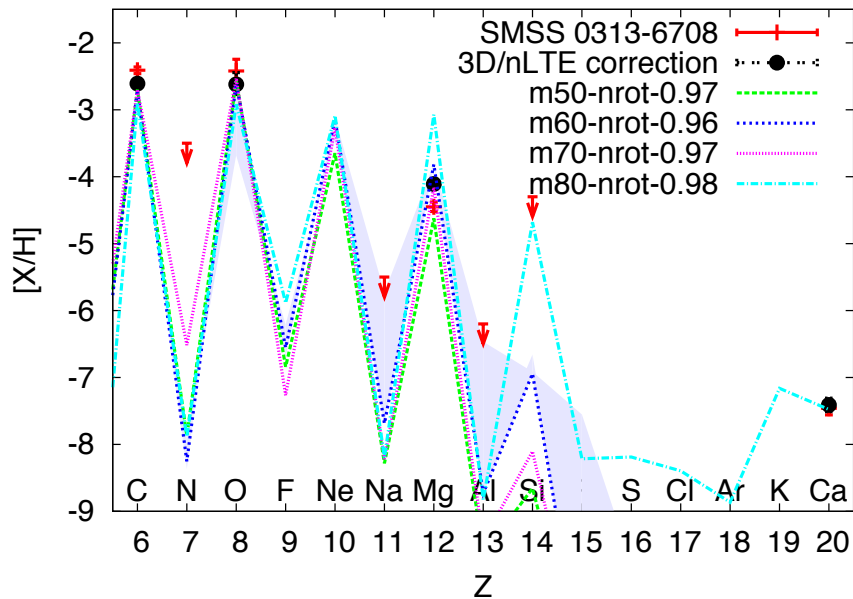
Figure 5.1: The abundance pattern of SMSS 0313-6708 which has [Fe/H] < -7.1. Red crosses and arrows show observed values and upper limits, and black points show corrected values accounting for the effect of 3D/non-LTE stellar atmosphere, respectively. Four model yields are non-rotating 50 $M_\odot$ with f_{ej}=0.97 (green long-dashed), non-rotating 60 $M_\odot$ with f_{ej}=0.96 (blue short-dashed), non-rotating 70 $M_\odot$ with f_{ej}=0.97 (magenta dotted), and non-rotating 80 $M_\odot$ with f_{ej}=0.98 (cyan dash-dotted). A blue shadow shows the influence of changing f_{ej} in the range of 0.92–1.00 for the 60 $M_\odot$ model.

upper limit of extremely low value of $[\text{Fe/H}] < -7.1$[2] is estimated as the iron abundance. Owing to the low level of metal contents, sparse abundance information has been obtained. Similar to iron, upper limits are obtained for nitrogen, sodium, aluminum, and silicon. At the moment of the discovery, abundances of only four elements, lithium, carbon, magnesium, and calcium, have been obtained. In addition, the oxygen abundance has been determined by UV spectroscopy (Bessell et al., 2015). Among them, carbon and oxygen show an exceptionally large abundance of $[\text{C/H}] \sim -2.4$ (or ~ -2.6 considering 3D correction) and $[\text{O/C}] = 0.02 \pm 0.175$.

The fitting results are shown by Fig. 5.1. The small abundance ratio [Mg/C] ~ -1 gives the first constraint for the fitting. More massive models of ≥ 100 $M_\odot$ synthesize too much magnesium in their helium layer to account for the small magnesium abundance. Thus low mass (12–40 $M_\odot$) models, accounting for the magnesium production by carbon burning in CO cores, or intermediate-mass (50–80 $M_\odot$) models, producing magnesium in their helium layer, can explain the abundance ratio. Next, although only upper limits are obtained so far, abundance ratios of [Na/C] and [Al/C] are informative for the model constraint. Magnesium production by carbon burnings in the low mass models is necessarily accompanied with sodium and aluminum production. Also, all rotating models synthesize the odd-Z elements in their helium layers. These models overproduces sodium and aluminum

---

[2]Recently the value is lowered to < -7.52 by Bessell et al. (2015).

and are rejected. Therefore, I conclude that only non-rotating 50–80 M$_\odot$ models can explain the observed abundances of SMSS 0313-6708. It is noteworthy that the oxygen abundance, recently obtained by Bessell et al. (2015), is completely compatible with my models. This consistency strongly supports the conclusion, since the observation has been made after I firstly came to the conclusion in Takahashi et al. (2014).

The calcium abundance [Ca/H] ~ -7 is not used as a constraint in the above reasoning. Models of 50–70 M$_\odot$ do not synthesize calcium by themselves, thus they need other pollution source(s) that explain the small existence of calcium. This could be matter ejection of extremely limited fraction of inner region during the supernova explosion, which is also suggested by the recent hydrodynamical simulation by Chen et al. (2016). If so, the explosion would eject similar amount of heavy elements such as iron. The iron abundance of SMSS 0313-6708 might be in a similar level with calcium, [Fe/H] ~ -7, in this case. On the other hand, the massive model of 80 M$_\odot$ coincidentally produces calcium in its helium layer. In this case, no other pollution is needed. The model yields more magnesium than the observation, but this could be within the uncertainties of both observation and simulation. In addition, the extremely low abundance of calcium can be explained by external pollution by accreting the interstellar material (Yoshii, 1981). Indeed, Shigeyama et al. (2003) obtain that a wide metallicity distribution function having the peak metallicity of [Fe/H] ~ -6 for Pop III low mass stars. This estimate will be applicable to the almost iron-free SMSS 0313-6708 to explain the low abundance of [Ca/H] ~ -7.

The explanation proposed here is consistent with the model by Keller et al. (2014). The given mass, 60 M$_\odot$, is exactly inside the mass range of my conclusion, and their model is a non-rotating first star. The small difference is in a production mechanism of calcium. They attribute calcium production by the breakout reactions from CNO-cycle during the stable hydrogen burning phase. On the contrary, such fast proton-capture reactions only take place in later phases of evolution of massive stars of $\geq$80 M$_\odot$ in my models. Different models have been proposed by Ishigaki et al. (2014). Among their best-fit models, a 25 M$_\odot$ model exploded with a high explosion energy of 10^{52} erg well reproduces the low [Na/Mg] and [Al/Mg] ratios. To distinguish the model with my model, the abundance ratio [O/C] is informative. Reflecting the difference in initial masses of models, my best fit models suggest the oxygen abundance will be [O/C] ~ 0, while the model by Ishigaki et al. (2014) has much lower value of [O/C] ~ -2. Recent observation of [O/C] ~ 0 by Bessell et al. (2015), therefore, prefers the model of less energetic explosion from a 50–80 M$_\odot$ progenitor to the model of energetic explosion from a 25–40 M$_\odot$ progenitor.

5.1.2   HE 0107-5240

HE 0107-5240 is an HMP star, having the metallicity of [Fe/H] $= -5.3$, firstly reported by Christlieb et al. (2002). The fitting result is plotted on Fig. 5.2. Observational data are collected from Christlieb et al. (2004), Bessell et al. (2004), Bessell & Christlieb (2005), and for 3D correction, from Collet et al. (2006) . The
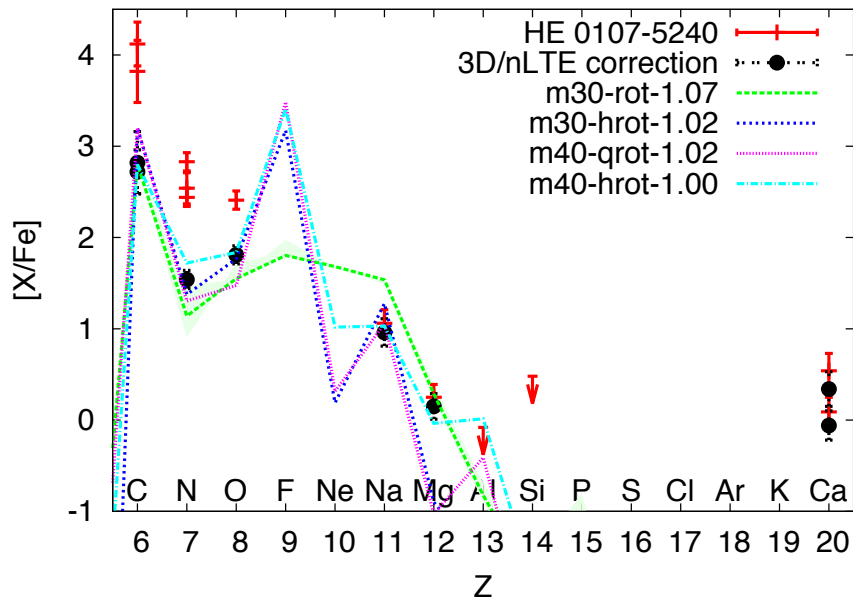
Figure 5.2: Same as Fig. 5.1, but for HE 0107-5240. The star has [Fe/H] = -5.3. Selected model yields are rotating 30 $M_\odot$ with f_{ej}=1.07 (green long-dashed), half-speed-rotating 30 $M_\odot$ with f_{ej}=1.02 (blue short-dashed), quarter-speed-rotating 40 $M_\odot$ with f_{ej}=1.02 (magenta dotted), and half-speed-rotating 40 $M_\odot$ with f_{ej}=1.00 (cyan dash-dotted). A green shadow corresponds to different f_{ej} models from 1.00–1.13 for the rotating 30 $M_\odot$ model.

best fit model found from the basic model grid is the rotating 30 $M_\odot$ model with the mass ejection parameter of $f_{ej} = 1.07$. In addition to the basic model, models with a bit slower rotation are calculated and fitted to the observation. They are 30 $M_\odot$ with half speed of rotation and 40 $M_\odot$ with half and quarter speed of rotation.

The very small [O/C] = −1.4 is the most informative abundance ratio of the star. Since a CO core of a massive star has much larger O/C ratio, matter ejection from inside of the CO core is rejected to account for the observation. Therefore, it turns out that those elements are produced in the outer region than the helium layer of the source star. Next, the abundance ratio of magnesium, [Mg/C] ∼ −3, provides the constraint on the initial mass. As more massive stars overproduce magnesium in their helium layer, 30 $M_\odot$ models provide good fits for the observation. Moreover, the sodium abundance ratio [Na/C] ∼ −2 excludes non-rotating models. The result does not so much depend on the mass ejection parameter. The wide $f_{ej} = 1.01$–1.13 suggests the robustness of this fitting.

Since the best fit model slightly overproduces sodium, models with slower rotation speeds have been calculated. Among them, a 40 $M_\odot$ model with half speed of rotation provides nearly perfect fitting. Note that calcium and other heavy elements are needed to be explained by the other process in this fitting. The small calcium abundance of [Ca/Fe] ∼ 0 suggests that those heavy elements come from the same origin.

Here I compare the above result with two previous works. The first model is a mixing-fallback model proposed by Iwamoto et al. (2005). With a mass cut of 6.3 $M_\odot$ and with a very small escape fraction of 1.2×10^{-4}, their 25 $M_\odot$ model
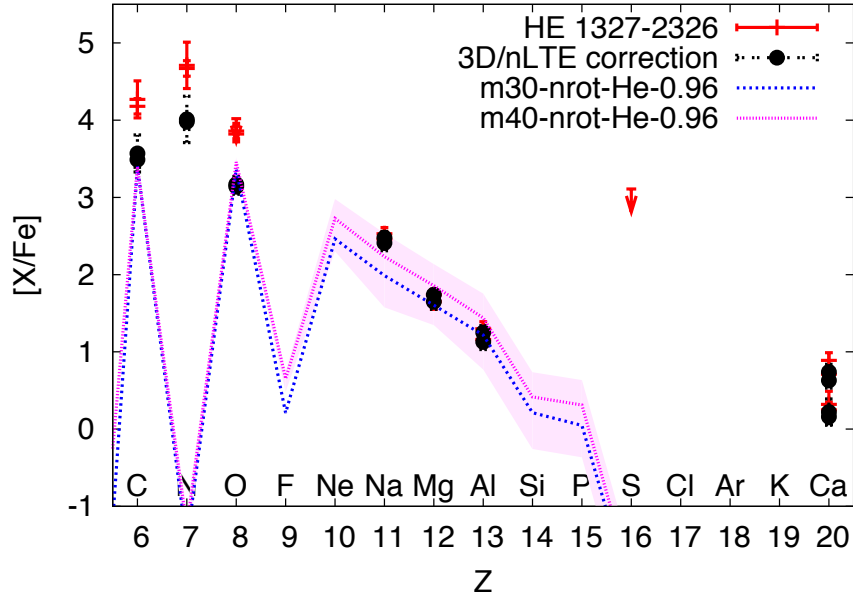
Figure 5.3: Same as Fig. 5.1, but for HE 1327-2326. The star has [Fe/H] = −5.7. Model yields of non-rotating 30 $M_\odot$ with f_{ej}=0.96 (blue short-dashed) and non-rotating 40 $M_\odot$ with f_{ej}=0.96 (magenta dotted) are presented. A magenta shadow corresponds to different f_{ej} models from 0.95–0.97 for the 40 $M_\odot$ model.

could provide a very nice fitting results to the observation. Corresponding to the large mass cut, carbon and oxygen distributed in the helium layer account for the low [O/C]. On the other hand, inner carbon burning product accounts for the low Mg abundance with the small escape fraction. It seems that a high degree of fine-tuning to those parameters would be required in the model. The other model has been proposed by Limongi et al. (2003), in which superposition of two supernovae of a less energetic explosion from 35 $M_\odot$ and a typical supernova from 15 $M_\odot$ differently contribute to the yield and explain the observation in combination. The strategy dividing elements into lighter and heavier group is similar to my model. Difference exists for the sodium production mechanisms. They attribute the sodium production by proton injection into the helium layer. As discussed earlier, the process is well known to occur in metal-poor ∼ 15–40 $M_\odot$ stars. However, since the timescale of the reactive mixing will be too short to be properly treated by the current numerical method, special care will be needed to treat the nucleosynthetic result. As the nucleosynthesis is based on the robust mechanism of rotationally induced reactions, I conclude that my model provides more realistic interpretation on the abundance pattern of HE 0107-5240 than previous models.

5.1.3   HE 1327-2326

HE 1327-2326 is a subgiant HMP star with [Fe/H] = −5.7, reported by Frebel et al. (2005). Figures 5.3 and 5.4 are the same as Fig. 5.1, but for HE 1327-2326. These figures have the same observation points, but have different model fitting.
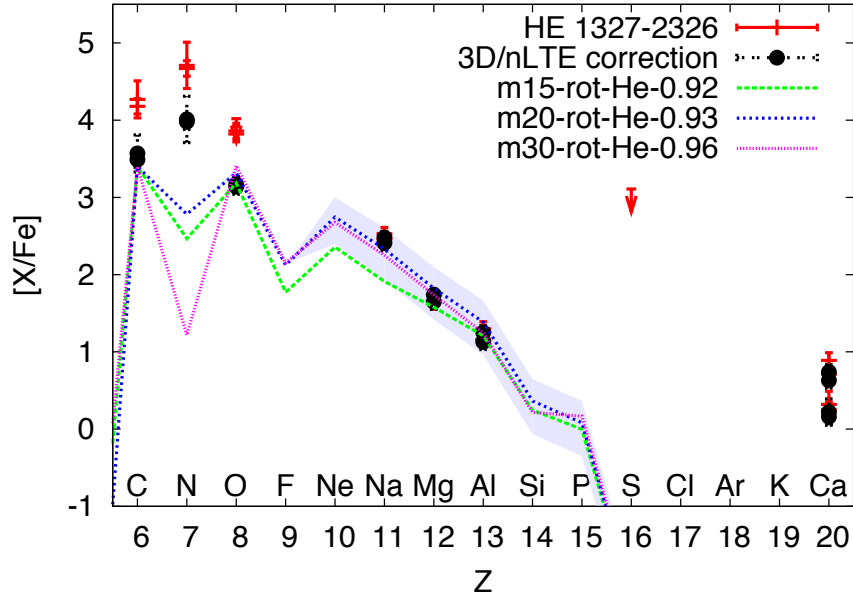
Figure 5.4: Same as Fig. 5.1, but for HE 1327-2326. Three model yields of rotating 15 M$_\odot$ with f_{ej}=0.92 (green long-dashed), rotating 20 M$_\odot$ with f_{ej}=0.93 (blue short-dashed), and rotating 30 M$_\odot$ with f_{ej}=0.96 (magenta dotted) are presented. A blue shadow corresponds to different f_{ej} models from 0.92–0.94 for the 20 M$_\odot$ model.

In the former figure, non-rotating models are presented, while the latter shows rotating models. Plotted observation points are taken from Aoki et al. (2006), Frebel et al. (2006, 2008), and Bonifacio et al. (2012). For 3D correction, results in Collet et al. (2006) are applied onto data obtained by Aoki et al. (2006) and Frebel et al. (2006).

Firstly, since the star shows negative [O/C], the ejection of the inner CO core material should be limited, and thus materials distributing in the outer region dominate the ejecta. Then the small [Mg/C] = −1.8 cannot be explained by more massive models than 40 M$_\odot$, which overproduce magnesium in their helium layers. On the other hand, by ejecting the outer edge of the carbon burning materials, models equal to or less massive than 40 M$_\odot$ explain the abundance. This naturally explains the decreasing trends in [Na, Mg, Al/C], because sodium, magnesium, and aluminum are produced by the carbon burning.

Further constraints can be made. The smallest 12 M$_\odot$ models produce less sodium and fail to explain the sodium ratio. Non-rotating 15 and 20 M$_\odot$ models suffer from proton ingestion and overproduce calcium. As a result, intermediate-mass stars of 30–40 M$_\odot$ for non-rotating models and 15–30 M$_\odot$ for rotating models give a consistent yield to the observation. The best-fit models are for non-rotating 40 M$_\odot$ and rotating 20 M$_\odot$ models. Because M_{ej} in these models are set to edges of carbon convective regions, acceptable widths of M_{ej} become very narrow. The acceptable ranges are shown in Figs. 5.3 and 5.4 as colored shadows, corresponding to $f_{\mathrm{ej}} = 0.95$–0.97 for the non-rotating 40 M$_\odot$ model and to $f_{\mathrm{ej}} = 0.92$–0.94 for the rotating 20 M$_\odot$ model.

HE 1327-2326 shows significant enhancement of nitrogen. Although none of our

70

calculation presented in this work does not consistently match with the nitrogen abundance, a weak supernova from a rotating progenitor may be able to explain the observation. Our rotating models only include moderate rotators of $v_{\rm rot}/v_{\rm k} \sim 0.15$, and the best model of 20 $M_\odot$ yields about 1/10 of observed nitrogen. Therefore, one possibility to account for the large production is fast rotation in which highly effective internal mixing will take place. Also, a rotating star with a very small but non-zero metallicity is known to have a large enhancement in nitrogen production. Comparing the results by Ekström et al. (2008) and Hirschi (2007), models with a metallicity of 10^{-8} show larger nitrogen production than Pop III models. Ekström et al. (2008) has explained this trend as a consequence of existence and absence of CNO elements at its birth. This is because, a metal poor progenitor with CNO elements can support the structure by the CNO cycle from the first ignition of hydrogen. At the end of the core hydrogen burning phase, this results in faster core rotation and thus more effective internal mixing.

The nitrogen enhancement may be explained by an intrinsic nucleosynthesis. In a low mass metal poor star, a process called the helium-flash driven deep mixing (He-FDDM) may take place (Fujimoto et al., 1990, 2000; Suda et al., 2004). In the process, a convective region powered by a shell helium-flash penetrates into the hydrogen envelope, resulting in nucleosynthesis of nitrogen. To compare with the scenario of the nitrogen enhancement due to the rotationally induced mixing, an isotopic ratio of ^{12}C/^{13}C will be useful. In the case of the intrinsic enhancement, theory predicts the equilibrium value of the CN cycle of ^{12}C/^{13}C $\sim$ 3–4 (Picardi et al., 2004; Weiss et al., 2004; Aoki et al., 2006). On the other hand, a much higher isotopic ratio of 21.5 is resulted in my rotating 20 $M_\odot$ progenitor. The observation provides a lower limit of the isotopic ratio of ^{12}C/^{13}C > 5. This prefers the rotation induced nitrogen enhancement to the intrinsic nitrogen production. One note, however, should be added here. Since the present models are still insufficient in nitrogen production by a factor of ~ 10, a model that is compatible with the nitrogen abundance may produce ~ 10 times more ^{13}C than these models. This will reduce the isotopic ratio, thus will work in the opposite direction.

5.2   Comparison with PISN yields

5.2.1   General trends of observed abundance ratios

One purpose of this section is to find an abundance ratio that is useful to discriminate a possible candidate of PISN children from the other normal metal-poor stars. The ratio, thus, must be made of abundances of easily accessible elements by observations. Table 5.3 shows the number of stars compiled in *SAGA* database, in which the abundance of each element is determined by observations. It indicates that the most accessible elements are magnesium, calcium, titanium, and iron, then they are followed by sodium, aluminum, silicon, chromium, nickel, and zink. Among them, magnesium is selected as the base, or the denominator, of the abundance ratios. First this is due to the good accessibility, and moreover because it facilitates comprehensive comparisons of the theoretical yields of PISNe

Table 5.3: Number of stars in *SAGA* database

element	number of stars
Na	2298
Mg	3490
Al	1972
Si	2485
P	0
S	350
Cl	0
Ar	0
K	256
Ca	3485
Sc	1240
Ti	3161
V	916
Cr	2257
Mn	1256
Fe	4022
Co	1113
Ni	2660
Cu	602
Zn	1719

Notes. Numbers of stars in *SAGA* database, in which the abundance is observed for each element, are shown.

as shown in the preceding chapter.

Among the peculiar abundance patterns of the PISN yields, the abundance ratio of [Na/Mg] is found to show the nearly mass-independent constant value of $-1.58 - -1.46$, and thus is one of the good indicator of the odd-even variation. Corresponding observations are plotted in Fig. 5.5 as a function of [Fe/H]. In this figure, a theoretically obtainable band is overlaid for the comparison, and a typical error of observations, ± 0.1 dex, is indicated by the magenta cross. The main component, including the decreasing trend toward low [Fe/H], has been well reproduced by galactic chemical evolution models taking CCSN ejecta into account (e.g. Kobayashi et al., 2006). Interestingly, although the figure includes more than 2000 stellar data, no stars are found within the theoretical band of the [Na/Mg] ratio. In other words, no metal-poor star currently showing sodium signature at its surface agrees with the PISN yields. Therefore, if the observation achieves to detect the low sodium abundance, a candidate of PISN children will show the small [Na/Mg] ratio distinctively apart from the other metal-poor stars. Possibly the lack of stars in the low [Na/Mg] region is explained by the observational limit. In this case, the candidate star should not exhibit detectable sodium lines in its spectroscopy.

For other elements of aluminum, silicon, calcium, and zinc, moderate numbers (several to tens) of stars are found inside the theoretical bands. Then, as a next step, comparisons using combinations of them are conducted.

Stellar data are plotted on a plane of [Ca/Mg] and [Al/Mg] in Fig. 5.6. As
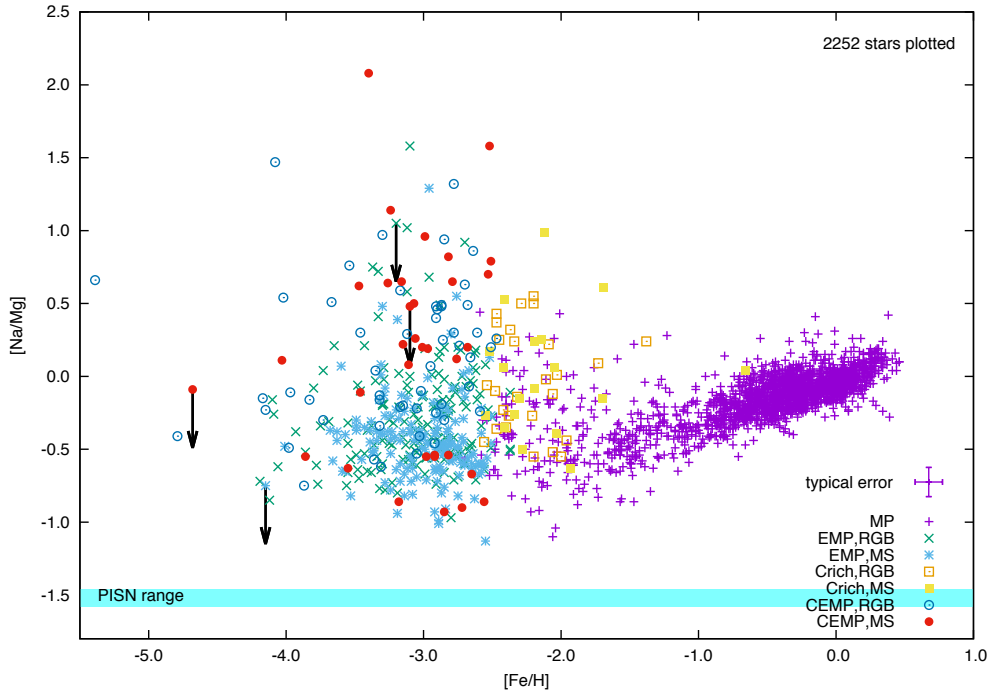
Figure 5.5: [Na/Mg] versus [Fe/H] collected from the compilation of the *SAGA* database. Stellar data are plotted by points. The cyan band shows the obtainable variations of theoretical yields by changing the initial mass.
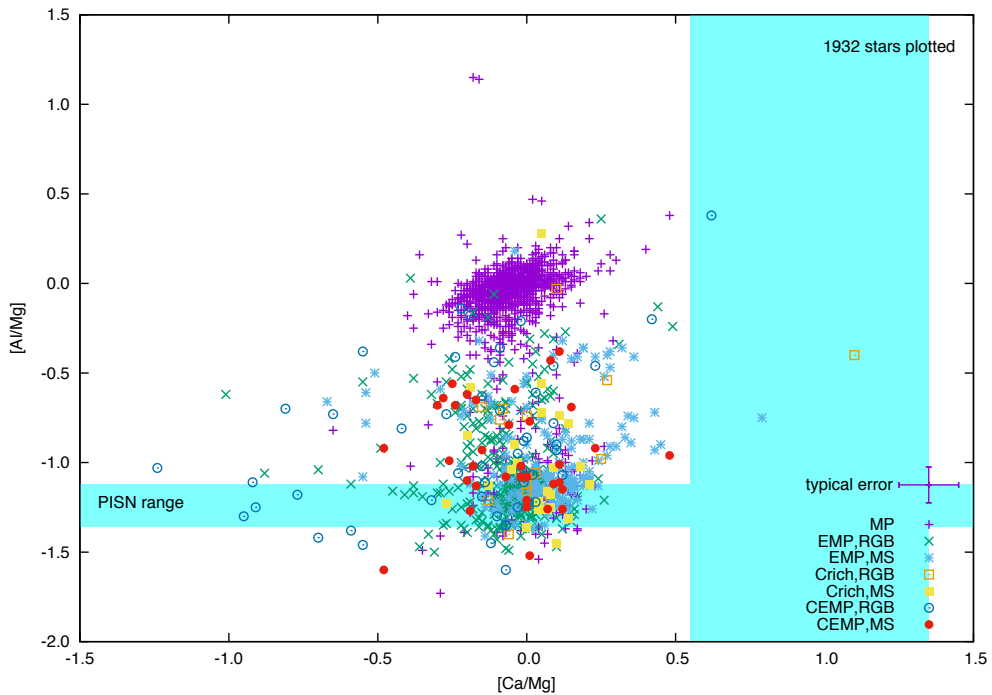
Figure 5.6: Same as Fig. 5.5 but for [Al/Mg] versus [Ca/Mg].
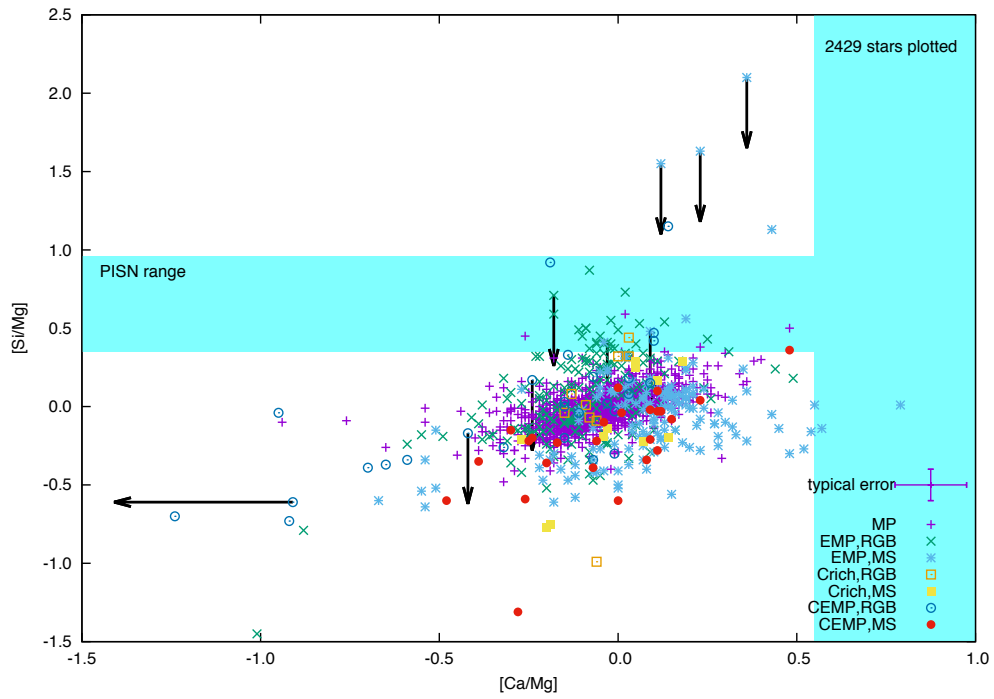
Figure 5.7: Same as Fig. 5.5 but for [Si/Mg] versus [Ca/Mg].
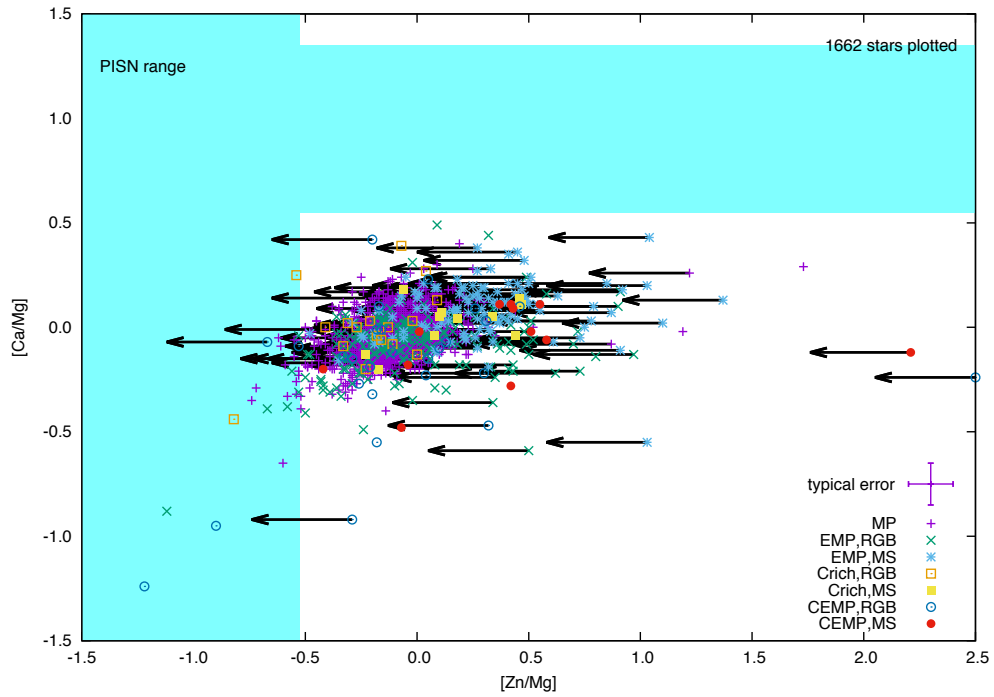
Figure 5.8: Same as Fig. 5.6 but for [Ca/Mg] versus [Zn/Mg].

74
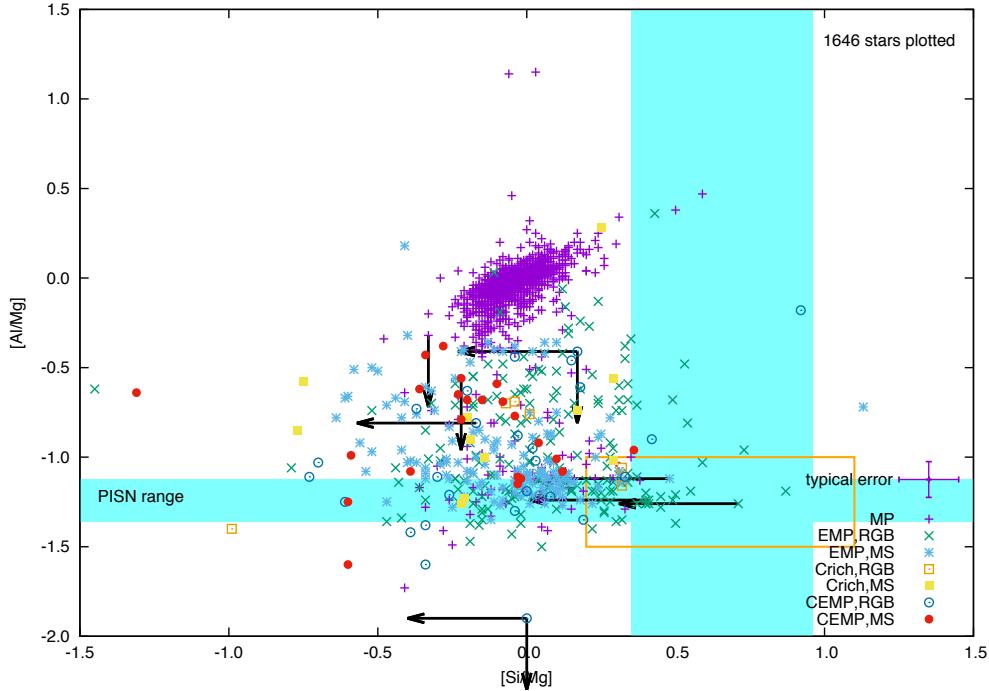
Figure 5.9: Same as Fig. 5.6 but for [Al/Mg] versus [Si/Mg]. Stars in the orange box are selected for the comparison with theoretical yields.

well as sodium, the main evolution sequences of calcium and aluminum have been well explained by CCSN ejecta (Kobayashi et al., 2006). As for the PISN yields, while tens of stars are found to be included within the theoretical range of either [Ca/Mg] or [Al/Mg], no stars show comparable values of both ratios at the same time. The same takes place for the [Ca/Mg] vs [Si/Mg] plot shown as Fig. 5.7, and for the [Zn/Mg] vs [Ca/Mg] plot shown as Fig. 5.8. As the majority of stars in the sample have lower [Ca/Mg] ~ 0 than the theoretical limit, these disagreements can be attributed to too low calcium abundances of currently observed metal-poor stars. Thus, the hierarchy of the problem is opposite to [Na/Mg]: the requirement of [Ca/Mg] $= 0.78 - 1.35$ is too large for the current stellar samples to agree with. The PISN children candidate will show a higher [Ca/Mg] ratio than the other metal-poor stars, even if they successively match the abundance patterns of [Al/Mg], [Si/Mg], or [Zn/Mg] in advance.

In Fig. 5.9, the observed abundance patterns are shown for the [Al/Mg] vs [Si/Mg] plot. In this case, numbers of stars are found to agree with the theoretical yields. Considering the typical error of the observation, 56 stars, which are inside the orange box of ([Al/Mg], [Si/Mg]) $= (0.2, -1.0) - (1.1, -1.5)$, are selected for the further comparison with the theoretical yields.

Finally, I discuss abundance ratios made by iron-peak elements except for zinc. They are titanium, chromium, iron, and nickel. I find that they are not as useful as the other accessible elements discussed above. The critically important reason is that, inside the large variations of the theoretical abundance patterns, the most feasible values of [X/Mg] $= 0$ is included. The calculated range of [Ti/Mg] spans,

for example, from -0.77 to 0.55. Therefore majority of observations is included in the theoretical bands, and they cannot discriminate the candidate of PISN children from other metal-poor stars.

5.2.2   Detailed comparisons with metal-poor stars

Metal-poor stars compared with theoretical PISN yield patterns in this work are summarized in Table 5.4. In addition to SDSS J0018-0939 (Aoki et al., 2014), 56 stars are selected from $SAGA$ database. Since I do not utilize the metallicity of the stars, [Fe/H], as the condition of the selection, the sample includes metal-poor stars with metallicity as large as -1.86. Most of these relatively-metal-rich stars will show the results of not one-time but many-times metal pollutions in their abundances. However, the wide range in metallicity can be rather adequate for the comparison with PISN yields, as some theoretical works suggest that high metallicity of $\sim 10^{-3}$ $Z_\odot$ is reachable by a one-shot PISN in the early universe due to the large metal production (Karlsson et al., 2008; Greif et al., 2010). Therefore, the high maximum metallicity characterizes the sample of this work, as most of the previous works except for Aoki et al. (2014) have considered only EMP stars of [Fe/H] $\lesssim -3$ to be compared with PISN yield patterns.

First of all, just as a confirmation of the earlier findings, it is shown that metal-poor stars in the sample have neither the low sodium abundances of [Na/Mg] = $-1.58 - -1.46$ nor the high calcium abundances of [Ca/Mg] > 0.78. In addition, three characteristics of abundance patterns are found from the stellar sample. They are

1. the larger [Sc/Mg] than the theoretical values,

2. the larger [Zn/Mg] than the theoretical values, and

3. the inconsistently smaller [Cr/Co] than the theoretical values.

Representative stellar abundances are plotted in Figs. 5.10–5.12, while results of comparisons for all of those stars are shown in the appendix C.

It is shown that only five stars in the sample have low [Sc/Mg] < -0.7 ratios. They are #14. CS22891-200 ([Sc/Mg] = -1.27), #21. CS22898-047 ([Sc/Mg] = -0.71), #34. CS22956-050 ([Sc/Mg] = -0.85), #35. CS22956-062 ([Sc/Mg] = -0.74), and #50. HE0056-3022 ([Sc/Mg] = -0.75). The abundance pattern of #34. CS22956-050 is shown in Fig. 5.10. Since, similarly to [Na/Mg] and [Al/Mg], theoretical ratios of [Sc/Mg] is found to show the nearly mass-independent low values of $-1.06 - -0.91$, comparing the [Sc/Mg] ratio is useful to distinguish a PISN children candidate from the other metal-poor stars. The ratio of [Sc/Mg] thus can be used as the second indicator of the odd-even variation of the PISN yields besides [Na/Mg]. It is noteworthy that a Pop III CCSN yield also tends to fail to reproduce the observed low scandium abundances (e.g., Kobayashi et al., 2006; Ishigaki et al., 2014). But in this case, ejection of high entropy inner material may be able to account for the production of not only scandium, but also titanium, cobalt, and zinc (Tominaga, 2009). Recent Pop III CCSN yields, in which

#	Obj	[Fe/H]	[Na/Mg]	[Ca/Mg]	[Sc/Mg]	[Zn/Mg]	[Cr/Co]	Reference
1	BD+34_2476	-1.97	-0.23	0.23	-0.01	-0.47	-0.13	Ishigaki et al. (2010, 2012, 2013) Gehren et al. (2006)
2	BD-01_2582	-2.62	-0.27	0.00	-0.54	-0.20	0.05	1.
3	BS16085-0050	-2.91	—	-0.23	-0.31	—	-0.22	2.
4	BS16928-053	-2.91	-0.52	-0.08	-0.69	—	-0.21	2., Lai et al. (2008)
5	CS22180-014	-2.86	-0.54	-0.03	-0.51	< 0.28	-0.38	1.
6	CS22183-031	-3.57	—	-0.22	-0.66	-0.10	-0.37	1.
7	CS22186-002	-2.72	-0.52	0.11	-0.39	0.03	-0.25	1.
8	CS22189-009	-3.92	-0.54	-0.06	-0.63	-0.08	-0.28	1.
9	CS22873-128	-3.75	-0.77	-0.18	-0.48	-0.29	-0.30	1.
10	CS22878-101	-3.53	—	-0.11	-0.65	0.02	-0.23	1.
11	CS22879-103	-2.16	—	-0.06	-0.48	-0.19	-0.05	1.
12	CS22886-044	-1.86	—	0.14	-0.25	-0.14	-0.11	1.
13	CS22888-002	-2.93	—	0.05	-0.51	< 0.26	-0.38	1.
14	CS22891-200	-4.06	—	-0.05	-1.27	< 0.01	-0.25	1.
15	CS22893-005	-2.99	-0.56	-0.01	-0.47	< -0.04	-0.15	1.
16	CS22894-019	-2.98	—	0.02	-0.33	< 1.10	-0.36	1.
17	CS22894-049	-2.84	—	0.02	-0.36	< 0.30	-0.43	1.
18	CS22896-015	-2.85	-0.57	-0.03	-0.27	-0.47	-0.06	1.
19	CS22896-110	-2.85	—	-0.03	-0.57	-0.34	-0.23	1.
20	CS22896-136	-2.41	—	0.18	-0.36	-0.06	-0.13	1.
21	CS22898-047	-3.51	—	-0.02	-0.71	0.12	-0.50	1.
22	CS22941-017	-3.11	-0.57	-0.06	-0.44	-0.27	-0.21	1.
23	CS22942-002	-3.61	—	-0.16	-0.62	-0.03	-0.51	1.
24	CS22942-011	-2.88	-0.45	-0.10	-0.49	-0.14	-0.14	1.
25	CS22943-095	-2.52	—	0.11	-0.31	0.02	-0.24	1.
26	CS22943-132	-2.63	—	-0.03	0.24	-0.48	-0.33	1.
27	CS22944-032	-3.22	—	-0.09	-0.59	-0.24	-0.31	1.
28	CS22945-028	-2.92	-0.56	-0.04	-0.64	-0.30	-0.11	1.
29	CS22947-187	-2.58	-0.40	-0.05	-0.45	-0.29	-0.01	1.
30	CS22949-048	-3.55	—	-0.02	-0.51	0.48	-0.19	1.
31	CS22950-046	-4.12	—	-0.09	-0.69	< 0.27	-0.35	1.
32	CS22951-059	-2.84	—	-0.01	-0.14	-0.26	-0.26	1.
33	CS22953-003	-3.13	-0.42	-0.06	-0.62	-0.02	-0.12	1., Spite et al. (2011)
34	CS22956-050	-3.67	—	-0.03	-0.85	-0.07	-0.31	1.
35	CS22956-062	-2.75	-0.69	-0.05	-0.74	< 0.04	-0.28	1.
36	CS22956-114	-3.19	—	0.02	-0.51	< 0.19	-0.20	1.
37	CS22957-019	-2.43	—	0.12	-0.20	-0.15	-0.16	1.
38	CS22957-022	-3.28	—	-0.06	-0.56	-0.03	-0.14	1.
39	CS22958-083	-3.05	-0.52	-0.18	-0.69	0.08	-0.08	1.
40	CS22963-004	-4.09	—	0.17	-0.69	< 0.91	-0.53	1.
41	CS22968-029	-3.10	—	0.03	-0.56	< 0.51	-0.23	1.
42	CS29502-092	-3.30	-0.53	-0.14	-0.61	-0.07	-0.19	1., Aoki et al. (2002)
43	CS29517-042	-2.53	—	0.14	-0.26	0.00	-0.24	1.
44	CS30312-059	-3.41	—	-0.05	-0.67	-0.05	-0.29	1.
45	CS30339-073	-3.93	-0.38	-0.08	-0.66	< 0.70	-0.36	1.
46	G25-24	-2.11	—	0.02	-0.43	-0.36	0.15	1.
47	HD110184	-2.52	—	0.10	-0.25	-0.13	0.00	2., Roederer et al. (2010)
48	HD175606	-2.39	-0.40	0.16	-0.26	0.07	-0.06	1.
49	HE0048-6408	-3.75	-0.39	-0.16	-0.65	< -0.07	-0.21	Placco et al. (2014)
50	HE0056-3022	-3.77	-0.35	-0.06	-0.75	0.11	-0.45	1.
51	HE0057-4541	-2.36	—	-0.10	-0.37	—	-0.51	3.
52	HE0105-6141	-2.58	—	-0.04	-0.21	—	-0.69	3.
53	HE0302-3417A	-3.70	—	-0.09	-0.51	-0.13	-0.65	4.
54	HE1320-2952	-3.69	-0.31	-0.09	-0.42	—	-0.63	Yong et al. (2013a)
55	HE2302-2154A	-3.88	—	0.01	-0.50	0.42	-0.76	4.
56	SDSSJ082511+163459	-3.22	—	0.19	—	—	-1.10	Caffau et al. (2011b)
	Aoki star							
57	J0018-0939	-2.46	-0.49	0.25	< -0.37	< 1.22	0.76	Aoki et al. (2014)

Notes. References are: 1. Roederer et al. (2014), 2. Honda et al. (2004), 3. Siqueira Mello et al. (2014), and 4. Hollek et al. (2011).
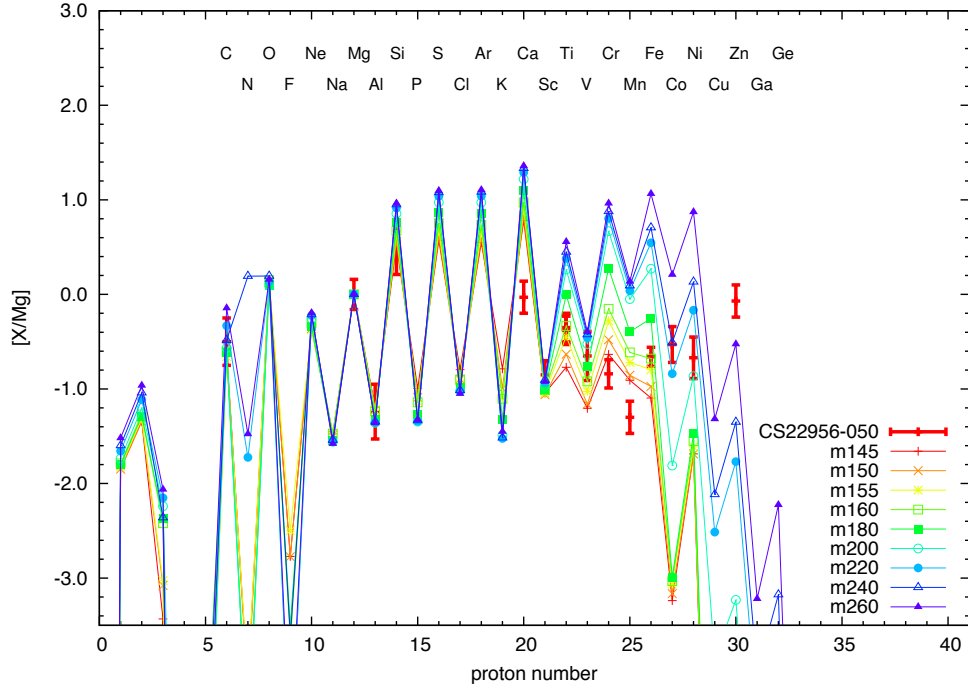
Figure 5.10: The abundance pattern of #34. CS22956-050. Red thick crosses show observed values, while PISN yields are shown by thin lines.

inner density is artificially reduced to mimic the high entropy effect, successively reproduce the observed high [Sc/Mg] ratios (Tominaga et al., 2014). On the other hand, as the explosion mechanism is clearly elucidated, no degree-of-freedom for this kind of modifications remains in PISN models.

Similarly, the abundance ratio of [Zn/Mg] is found to be useful for the discrimination. In this case, only four stars are found to have low [Zn/Mg] < 0.3, #1. BD+34_2476 ([Zn/Mg] = −0.47), #19. CS22896-110 ([Zn/Mg] = −0.34), #26. CS22943-132 ([Zn/Mg] = −0.48), and #46. G25-24 ([Zn/Mg] = −0.36), while the maximum theoretical value is [Zn/Mg] = −0.52 that is obtained by the most massive 260 $M_\odot$ PISN. As an example, the abundance pattern of #34. CS22943-132 is shown in Fig. 5.11. The small [Zn/Mg] ratio of the candidate star, if observed, will separate itself from the other majority of metal-poor stars in the [Zn/Mg] plot; otherwise the small abundance will be too faint to be detected. Physical origins of the distinctive ratios are different. The small [Na/Mg] and [Sc/Mg] ratios are representations of the odd-even variance of PISN yields, while the small [Zn/Mg] ratio is due to the low explosion temperature, with which only a part of a star is affected by the complete silicon burning.

Finally, I find that observed small ratios of [Cr/Co] < 0 introduce a critical inconsistency in explaining those observations by PISN yields. For the demonstration, a metal-poor star, #37. CS22957-019, is plotted as an example in Fig. 5.12. According to my yield calculations, chromium can be well produced by the lightest 145 $M_\odot$ PISN, which yields [Cr/Mg] = −0.63. As a result, a small initial mass of ∼ 145–150 $M_\odot$ is estimated from the [Cr/Mg] observation. On the other hand, only
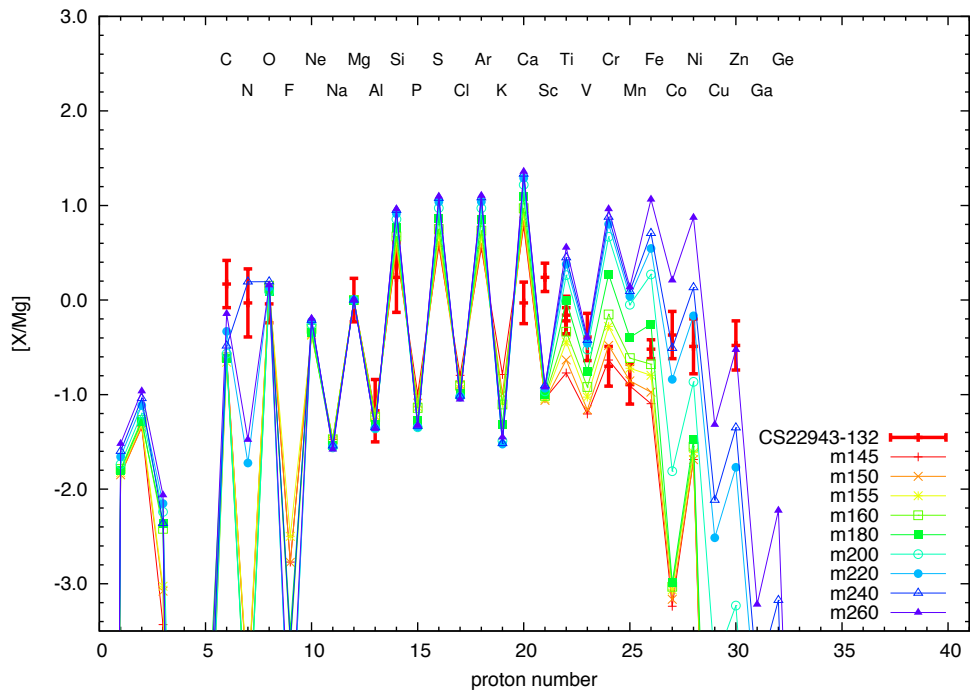
Figure 5.11: The abundance pattern of #34. CS22943-132.
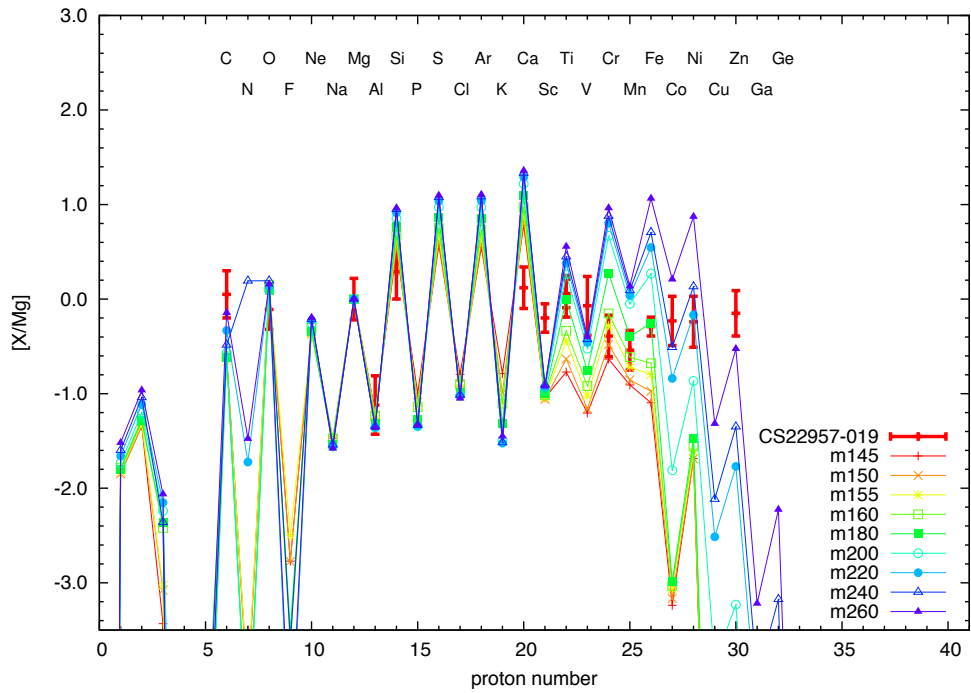
Figure 5.12: The abundance pattern of #37. CS22957-019.
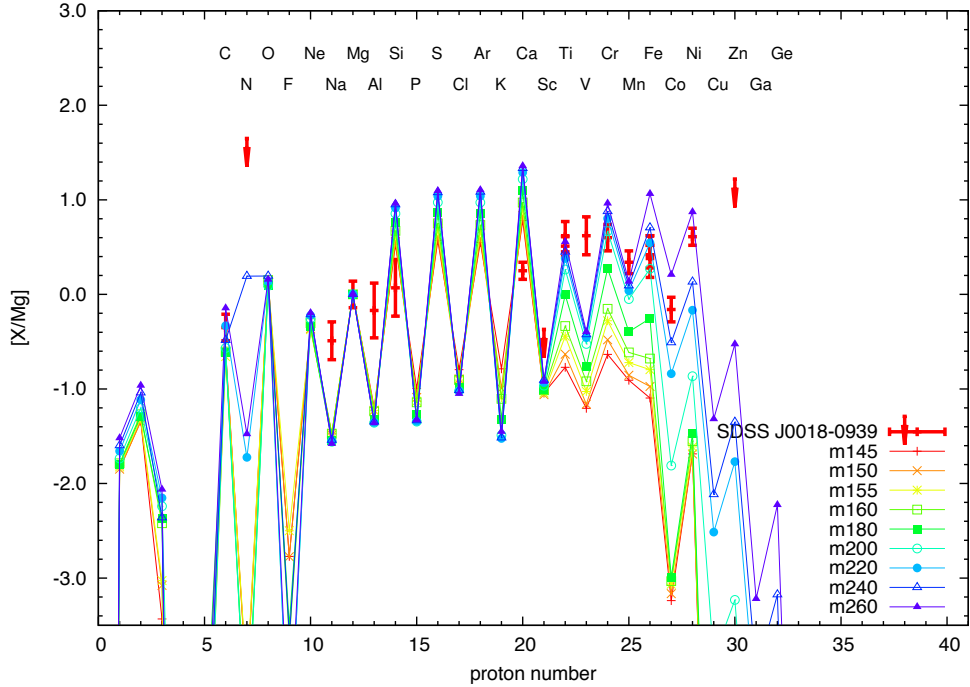
Figure 5.13: The abundance pattern of #57. SDSS J0018-0939.

more massive PISNe can yield cobalt. For instance, at least 220 $M_\odot$ is required to produce [Co/Mg] > -0.83. This results in a large initial mass estimate of $\sim$ 240 $M_\odot$ by using the [Co/Mg] ratio. The inconsistent two initial masses clearly reject the possibility to explain the stellar abundance by PISN yields. The same discussion is possible applying other iron-peak elements of [Ti/Mg], [Fe/Mg], or [Ni/Mg] than [Cr/Mg], but it is found that [Cr/Mg] tends to provide the smallest initial mass.

5.2.3   SDSS J0018-0939

SDSS J0018-0939 is a metal-poor main-sequence star with a metallicity of [Fe/H] $= -2.46$, discovered by Aoki et al. (2013). Aoki et al. (2014) further observe the distinctive abundance pattern, which is characterized by the low [α/Fe] ratios of [C, Mg, Si/Fe] and by the exceptionally small [Co/Ni] ratio. Despite the star has the relatively large metallicity, they assume that the star possesses primitive chemical abundances based on the low abundances of neutron-rich elements of [Sr/Fe] < -1.8 and [Ba/Fe] < -1.3. One explanation given in the work is a single nucleosynthesis by a very massive star occurring in the early universe. They compare two theoretical yields with the observation; one is a Pop III 1000 $M_\odot$ CCSN model exploded with 6.67×10^{53} erg (Ohkubo et al., 2006), and the other is a Pop III 130 $M_\odot$ PISN model (Umeda & Nomoto, 2002), and moreover discuss that the low [C, Mg/Fe] and the low [Co/Ni] can be explained by the PISN model.

Figure 5.13 shows comparison between the stellar abundances of SDSS J0018-

0939 (Aoki et al., 2014) and my PISN yield models. Interestingly, only upper limits have been obtained for informative elements of scandium and zinc. Therefore the star avoids an early stage rejection due to overproductions of these elements. Besides, as pointed out in the original work, the exceptionally low cobalt abundance works in a good direction. Thanks to the low [Co/Mg], the iron-peak elements except for vanadium are compatible with massive PISN models of 240–260 $M_\odot$. However, on the other hand, there are two fundamental problems for the explanation. First is the too weak odd-even variation of the observed pattern. Sodium, aluminum, and vanadium in the star are apparently overproduced. Second is the underproduction of calcium. The low calcium abundance may be matched with the least massive PISN model yields, $\lesssim 145$ $M_\odot$. However, the mass range is completely inconsistent with the estimate given by iron-peak elements. Although the low cobalt abundance is still very interesting, contrary to Aoki et al. (2014), I conclude that the abundance pattern of SDSS J0018-0939 is not compatible with any of my PISN models.

5.3 Conclusion of this chapter

Yields from massive first stars of 12–140 $M_\odot$ are calculated by the weak supernova explosion model, and the abundance patterns are compared with the three most-iron-deficient stars discovered so far. The abundance pattern of SMSS 0313-6708 can be explained by non-rotating massive 50–80 $M_\odot$ models with large inner boundaries of ejections, $f_{ej} = 0.92$–1.00. The non-rotating 60 $M_\odot$ model provides the best explanation for both the observed low [Mg/C] and the upper limits on [Na, Al/C], while the low abundance of [Ca/C] can be consistently explained by the 80 $M_\odot$ model. The recent detection of [O/C] ~ 0 strongly supports the consistency of the explanation. Abundances of [N, O, Na/C] in HE 0107-5240 can be consistently explained by a rotating 30 $M_\odot$ model. The wide acceptable range in $f_{ej} = 1.01$–1.13 suggests the robustness of this model. Moreover, 30 and 40 $M_\odot$ models with slower rotations provide much better fitting results for the sodium abundance. HE 1327-2326 has a small [O/C] and an interesting decreasing trend of [Na, Mg, Al/C]. These abundances are consistently explained by both rotating and non-rotating 15–40 $M_\odot$ models, ejecting the mass from the outer edge of the carbon burning regions, $f_{ej} = 0.92$–0.97. To explain the large abundance of [N/C], much faster rotation or another origins than the single explosion may be needed.

In conclusion, I have constrained the initial parameters of source stars for the three most-iron-deficient stars. Not only the deficiency of iron, but also the enhancement of intermediate mass elements of carbon, nitrogen, oxygen, sodium, and magnesium is an important feature of these stars. I have found that this peculiar abundance feature is useful to constrain the initial parameters of the progenitor star. The first comparison provides the indication of the existence of the massive first stars of 15–80 $M_\odot$ in the early universe. Moreover, the variation in the estimated stellar rotation velocities suggests that the intrinsic diversity also exists in the rotation properties of first stars. Similar analysis will be applicable to other carbon enhanced HMP stars, which will be discovered by future observations.

The results will be valuable to constrain the characteristics of the first stars in the early universe.

More massive 145–260 M$_\odot$ first stars explode as PISNe. The yields are calculated by one-dimensional hydrodynamic calculations. Thanks to the development of a large compilation data of *SAGA* database, I have conducted the first systematic comparison between the theoretical PISN yields with surface abundances of metal-poor stars including large number of data obtained from recent observations.

Unfortunately, I have found no candidate metal-poor stars included in the sample that exhibit characteristic abundance signatures of PISN yields. Thus the constraint on the very massive Pop III stars has not been obtained. First, the predicted [Na/Mg] = $-1.58 - -1.46$ is too low to be compared with the current stellar observations, and second, the high [Ca/Mg] = $0.78 - 1.35$ exclude most of the metal-poor stars out from the candidates of PISN children. However, by making the direct comparisons, effectiveness of theoretically proposed abundance patterns can be verified. In addition to the [Na/Mg] ratio, the [Sc/Mg] ratio is found to be useful as the indicator of the odd-even variance of the PISN yields. Also, the low [Zn/Mg] < -0.52 due to the low explosion temperature can be used as a firm requirement for the candidate abundance pattern. The abundance pattern observed in the iron-peak elements, in most cases, is found to give critical inconsistency to the model yields: the small initial mass suggested by [Cr/Mg] is in complete disagreement with the large initial mass obtained by [Co/Mg], if the metal-poor star has a typical value of [Cr/Co] < 0. The interesting example, SDSS J0018-0939, has the exceptionally small [Co/Mg] ratio as discussed in Aoki et al. (2014). The large odd-Z abundances of [Na, Al, V/Mg] and the small [Ca/Mg] are, however, inconsistent with PISN yields.

Chapter 6

Conclusion

6.1 Summary and conclusion

The purpose of this thesis is to constrain the properties of massive first stars, such as the initial masses and rotational properties, by conducting the abundance profiling. The low metal abundances as well as the large scatters in the abundance ratios suggest that metal-poor stars observed in the local universe are born from the chemically primitive gas clouds existed in the early universe. Assuming that chemical signatures of the first metal ejection are imprinted in abundances of a metal-poor star, properties of the source star can be inferred by comparing the surface abundance of the metal-poor star and theoretically calculated yields of first stars.

In advance of the comparison, the characteristics of theoretical abundance patterns should be understood to specify the parameters of theoretical models. To begin with, I have calculated stellar yields of 12–140 $M_\odot$ first stars with and without taking stellar rotation into account. The *weak explosion* model is applied, in which the explosion is assumed to be so weak that the explosive nucleosynthesis does not change the outer distributing materials and only the outer weakly-bound material is ejected. I have found that various abundance distributions realize in the outer shell-helium regions. Yields of intermediate-mass α elements of magnesium and silicon mainly depend on initial masses, and nitrogen and odd-Z elements of sodium and aluminum depend on rotation velocities. These characteristic abundance patterns are well reflected in the stellar yields, and therefore are useful to deduce the properties of source stars.

Next, I have conducted a systematic calculation of explosion and nucleosynthesis of PISNe. I have investigated the energetics and the formalisms to accurately treat the energy conservation, and have confirmed the initial mass range of PISN to be 145–260 $M_\odot$. Nucleosynthesis of PISNe is calculated based on the accurate explosion simulations, in order to find characteristic abundance patterns that can be used to discriminate PISN signatures from the others. I have found that the elemental yields can be divided into three groups based on the mass dependencies. Abundance ratios of the first group, which consists of lighter elements of carbon to aluminum in addition to scandium, are nearly mass independent. Thus the ratios, [Na, Al, Sc/Mg], can be used as the first indication of the odd-even variance of

PISN yields. Abundance ratios of the second group, from silicon to calcium, depend on the initial mass. Therefore the ratios, [Si, Ca/Mg], are useful to determine the initial mass of the PISN. The heaviest elements of iron-peak elements show the strongest mass dependencies. The decreasing trend towards increasing mass number, which can be indicated by small abundance ratios of [Ni/Fe] or [Zn/Ni], can be the second requirement for PISN yields.

Finally, I have conducted abundance profiling utilizing theoretical yields calculated above. The yields of the weak explosion model are compared with the three most-iron-poor objects discovered so far; SMSS 0313-6708 of [Fe/H] < -7.1, HE 0107-5240 of [Fe/H] $= -5.3$, and HE 1327-2326 of [Fe/H] $= -5.7$. The abundance pattern of SMSS 0313-6708 is only explained by non-rotating 50–80 $M_\odot$ models with large inner boundaries of ejections, $f_{ej} = 0.92$–1.00. This is required to simultaneously explain the high magnesium abundance and low sodium and aluminum abundances. The reliability of the model is further reinforced by recent observational confirmation of the high oxygen abundance of [O/C] ~ 0. Abundances of [N, O, Na/C] in HE 0107-5240 is explained by a rotating 30 $M_\odot$ model. The wide acceptable ejection parameter of $f_{ej} = 1.01$–1.13 indicates the robustness of the model. The consistency of the model is also indicated as slower rotating models of 30 and 40 $M_\odot$ can provide better fitting results. HE 1327-2326 has a small [O/C] and an interesting decreasing trend in [Na, Mg, Al/C] ratios. Rotating and non-rotating 15–40 $M_\odot$ models can explain the abundances, by ejecting stellar materials from the outer edge of the carbon burning regions with $f_{ej} = 0.92$–0.97. The high nitrogen abundance may require much faster rotation or another origin than the single explosion.

In order to find the PISN signatures from the present metal-poor stellar sample, and to validate the applicability of characteristic abundance patterns for the discrimination, I have conducted the first systematic comparison between the theoretical yields of PISN and the big stellar abundance data compiled in *SAGA* database. Unfortunately, I have found no candidate metal-poor stars showing characteristic signatures of PISN yields. The predicted low [Na/Mg] and high [Ca/Mg] are too isolated from the main sequences of observed metal-poor stars. However, this means that these characteristic abundance ratios are useful to discriminate the hypothetical PISN children. In addition to [Na/Mg], the low abundance of [Sc/Mg] is found to be useful to indicate the odd-even variance, and the low [Zn/Mg] can be used as an indicator of the low temperature explosion of a PISN. Moreover, I have found that the critical inconsistency is often resulted from the [Cr/Co] ratio; the smaller initial mass indicated by [Cr/Mg] completely disagrees with the larger mass obtained by [Co/Mg]. Although the exceptionally small [Co/Mg] in SDSS J0018-0939 can avoid this inconsistency, the overabundance in odd-Z elements of sodium, aluminum, and vanadium, and the small [Ca/Mg] ratio are incompatible with any of my PISN yields.

Abundance profiling enables us to investigate the characteristics of massive first stars existed in the far-away early universe.

By the comparison with the most-iron-deficient stars, indication of the existence of ~ 15–80 $M_\odot$ first stars is obtained for the first time. Some of them would rotate, but some of others would not. This indicates the diversity of the rotation properties

of massive first stars. Further investigation will provide invaluable information on the properties of massive first stars. On the other hand, the characteristic yields of $\sim$ 100–140 M$_\odot$ stars, large abundance ratios of [O/C] and [Mg, Si/C], have not been found from the HMP stars. Moreover, no signature of PISN yields occurring from 145–260 M$_\odot$ first stars has been found from the current big sample of metal-poor stellar abundances. These result are incompatible with the wide initial mass distribution of first stars estimated by the recent cosmological simulations. Where are children of very massive first stars? This remains a big open question in investigations of the early universe.

6.2 Future prospects

In closing the thesis, I discuss future prospects on the theoretical investigations of the early universe.

First, the direct proceeding of this work will be made to increase the comparison number of the CEMP stellar samples for the abundance profiling of the weak supernovae. So far, $\sim$ 20 CEMP stars have been discovered with the metallicities of [Fe/H] < -4.0 (cf. Frebel & Norris, 2015). These are indeed good targets to be compared with the model. Characteristic abundances of massive first stars, especially from more massive side of $\sim$ 100–140 M$_\odot$ that are missed from the current comparison, may be found from the increasing samples.

Additionally, in order to maximize the applicability of the abundance profiling, further understanding of theoretical yields of various CCSN explosions will be done. The weak supernova model accounts for only a part of supernova explosions. Therefore, characteristic abundance patterns should be noticed for other explosions, such as for usual 10^{51} erg explosions, for ten times more energetic hypernovae (HNe), and for explosions with long GRBs. To discriminate HN yields from different initial masses and rotations will be of prime importance, because the majority of EMP stars, which have high [Co, Zn/Fe] ratios, are considered to be born from HN yields (Umeda & Nomoto, 2005).

Possibly the various CCSN explosion properties are inherited from the initial conditions of the progenitor evolution, such as the initial mass and the initial rotation velocity. To confirm the relation between the initial conditions and the fate, therefore, will be one of the most important challenge in the future. Such a relation, perhaps, is obtainable for metal-rich stars by calibrating the theory with observations. The key points here are how to accurately treat the effect of convection, stellar rotation, and binarity, which are currently only crudely estimated.

As for the metal-free stars in the early universe, however, it requires a special care to reduce the results obtained for the metal-rich universe. For instance, the pre-existence of a weak magnetic field is assumed for a rotating model in this thesis. The magnetic field is enhanced by a dynamo and results in an efficient angular momentum transport. However, the existence of the magnetic field in the early universe as well as the specific mechanisms of the dynamo process are currently only poorly investigated. Also, the evolution of binary system largely depends on the evolution of radii of components. Since the radii of first stars are affected

by mass loss and stellar rotation, completely different fates are possibly resulted if different conditions are assumed for these processes. Physically fundamental insights will be needed to construct a more reliable model for first stars.

As for the observational prospects, several progresses will be achieved. Future surveys will significantly increase the number of observations of metal-poor stars (e.g., the APOGEE survey; Majewski et al. 2010, the LEGUE survey; Deng et al. 2012, the GALAH syrvey; Heijmans et al. 2012, and the *Gaia* mission; Cacciari 2009). The large number of sample will enable us to conduct a statistical investigation for abundance profiling. A mass distribution of first stars in a range of ~ 12–140 M$_\odot$ may be obtained by the abundance profiling. Some of the metal-poor stars may exhibit characteristic signatures of PISN yields in their abundances. And ultimately, completely metal-free stars will be perhaps discovered. This observational progress should be accompanied with the improvements of the understanding of the stellar surface abundance. Currently, uncertainties on a surface abundance measurement are often dominated by the theoretical uncertainties due to 3D and non-LTE effects (Asplund, 2005). More accurate modeling of stellar surface will be highly demanding in the near future.

Finally, several next-generation telescopes will start the operations in the next decade. With the emergence of the Thirty Meter Telescope (TMT), the Extremely Large Telescope (ELT), the Giant Magellan Telescope (GMT), and the James Webb Space Telescope (JWST), much more accurate abundance determination and detection will be achieved. Furthermore, the direct observations of the first galaxies, the first supernovae, and perhaps even the first massive stars, will be possible. The direct detections of the ultra-high-z objects will provide crucially important information of the properties of first stars. In advance, theory should provide invaluable predictions on how to interpret those signals from the first objects and how to discriminate first objects from metal-poor but already metal-polluted objects, which will be observed much more frequently.

References

Abel T., Bryan G. L., Norman M. L., 2002, Science, 295, 93

Aoki W., Norris J. E., Ryan S. G., Beers T. C., Ando H., 2002, ApJ, 567, 1166

Aoki W., Beers T. C., Christlieb N., Norris J. E., Ryan S. G., Tsangarides S., 2007, ApJ, 655, 492

Aoki W., Tominaga N., Beers T. C., Honda S., Lee Y. S., 2014, Science, 345, 912

Aoki W. et al., 2006, ApJ, 639, 897

Aoki W. et al., 2013, AJ, 145, 13

Asplund M., 2005, ARA&A, 43, 481

Asplund M., Grevesse N., Sauval A. J., Scott P., 2009, ARA&A, 47, 481

Audi G., 2003, ArXiv Nuclear Experiment e-prints

Audouze J., Silk J., 1995, ApJ, 451, L49

Baraffe I., Heger A., Woosley S. E., 2001, ApJ, 550, 890

Barkat Z., Rakavy G., Sack N., 1967, Physical Review Letters, 18, 379

Beers T. C., Christlieb N., 2005, ARA&A, 43, 531

Beers T. C., Preston G. W., Shectman S. A., 1992, AJ, 103, 1987

Bessell M. S., Christlieb N., 2005, in V. Hill, P. Francois, F. Primas, eds, From Lithium to Uranium: Elemental Tracers of Early Cosmic Evolution. IAU Symposium, Vol. 228, pp. 237–238

Bessell M. S., Christlieb N., Gustafsson B., 2004, ApJ, 612, L61

Bessell M. S. et al., 2015, ApJ, 806, L16

Blinnikov S. I., Dunina-Barkovskaya N. V., Nadyozhin D. K., 1996, ApJS, 106, 171

Böhm-Vitense E., 1958, ZAp, 46, 108

Bonifacio P., Caffau E., Venn K. A., Lambert D. L., 2012, A&A, 544, A102

Bonifacio P. et al., 2015, A&A, 579, A28

Bromm V., Larson R. B., 2004, ARA&A, 42, 79

Bromm V., Coppi P. S., Larson R. B., 2002, ApJ, 564, 23

Bruenn S. W. et al., 2013, ApJ, 767, L6

Burrows A., 2013, Reviews of Modern Physics, 85, 245

Cacciari C., 2009, Mem. Soc. Astron. Italiana, 80, 97

Caffau E. et al., 2011a, Nature, 477, 67

Caffau E. et al., 2011b, A&A, 534, A4

Chatzopoulos E., Wheeler J. C., 2012, ApJ, 748, 42

Chatzopoulos E., van Rossum D. R., Craig W. J., Whalen D. J., Smidt J., Wiggins B., 2015, ApJ, 799, 18

Chen K. J., Heger A., Whalen D. J., Moriya T. J., Bromm V., Woosley S., 2016, ArXiv e-prints

Chiappini C., Hirschi R., Meynet G., Ekström S., Maeder A., Matteucci F., 2006, A&A, 449, L27

Chieffi A., Limongi M., 2004, ApJ, 608, 405

Chieffi A., Limongi M., 2013, ApJ, 764, 21

Chieffi A., Domínguez I., Limongi M., Straniero O., 2001, ApJ, 554, 1159

Chiu H. Y., 1968, Stellar physics. Vol.1

Choplin A., Maeder A., Meynet G., Chiappini C., 2016, A&A, 593, A36

Christlieb N., 2003, in R.E. Schielicke, ed., Reviews in Modern Astronomy. Reviews in Modern Astronomy, Vol. 16, p. 191

Christlieb N. et al., 2002, Nature, 419, 904

Christlieb N., Gustafsson B., Korn A. J., Barklem P. S., Beers T. C., Bessell M. S., Karlsson T., Mizuno-Wiedner M., 2004, ApJ, 603, 708

Clark P. C., Glover S. C. O., Smith R. J., Greif T. H., Klessen R. S., Bromm V., 2011, Science, 331, 1040

Cohen J. G., Christlieb N., Thompson I., McWilliam A., Shectman S., Reimers D., Wisotzki L., Kirby E., 2013, ApJ, 778, 56

Colella P., Woodward P. R., 1984, Journal of Computational Physics, 54, 174

Collet R., Asplund M., Trampedach R., 2006, ApJ, 644, L121

Cox J. P., 1968, Principles of stellar structure - Vol.1: Physical principles; Vol.2: Applications to stars

Cyburt R. H. et al., 2010, ApJS, 189, 240

Deng L. C. et al., 2012, Research in Astronomy and Astrophysics, 12, 735

Denissenkov P. A., VandenBerg D. A., 2003, ApJ, 598, 1246

Deupree R. G., 1990, ApJ, 357, 175

Ekström S., Meynet G., Chiappini C., Hirschi R., Maeder A., 2008, A&A, 489, 685

Ekström S. et al., 2012, A&A, 537, A146

Endal A. S., Sofia S., 1978, ApJ, 220, 279

Eriguchi Y., Mueller E., 1985, A&A, 146, 260

Espinosa Lara F., Rieutord M., 2007, A&A, 470, 1013

Ferguson J. W., Alexander D. R., Allard F., Barman T., Bodnarik J. G., Hauschildt P. H., Heffner-Wong A., Tamanai A., 2005, ApJ, 623, 585

Ferrara A., Pettini M., Shchekinov Y., 2000, MNRAS, 319, 539

Frebel A., Norris J. E., 2015, ARA&A, 53, 631

Frebel A., Christlieb N., Norris J. E., Aoki W., Asplund M., 2006, ApJ, 638, L17

Frebel A., Collet R., Eriksson K., Christlieb N., Aoki W., 2008, ApJ, 684, 588

Frebel A., Chiti A., Ji A. P., Jacobson H. R., Placco V. M., 2015, ApJ, 810, L27

Frebel A. et al., 2005, Nature, 434, 871

Fujimoto M. Y., Iben Jr. I., Hollowell D., 1990, ApJ, 349, 580

Fujimoto M. Y., Ikeda Y., Iben Jr. I., 2000, ApJ, 529, L25

Fukuda I., 1982, PASP, 94, 271

Fuller G. M., Fowler W. A., Newman M. J., 1982, ApJS, 48, 279

Gammie C. F., 2001, ApJ, 553, 174

Gehren T., Shi J. R., Zhang H. W., Zhao G., Korn A. J., 2006, A&A, 451, 1065

Georgy C., Ekström S., Meynet G., Massey P., Levesque E. M., Hirschi R., Eggenberger P., Maeder A., 2012, A&A, 542, A29

Georgy C. et al., 2013, A&A, 558, A103

Gies D. R., Lambert D. L., 1992, ApJ, 387, 673

Gil-Pons P., Gutiérrez J., García-Berro E., 2007, A&A, 464, 667

Graboske H. C., Dewitt H. E., Grossman A. S., Cooper M. S., 1973, ApJ, 181, 457

Greif T. H., Glover S. C. O., Bromm V., Klessen R. S., 2010, ApJ, 716, 510

Greif T. H., Bromm V., Clark P. C., Glover S. C. O., Smith R. J., Klessen R. S., Yoshida N., Springel V., 2012, MNRAS, 424, 399

Hachisu I., Matsuda T., Nomoto K., Shigeyama T., 1990, ApJ, 358, L57

Haiman Z., Loeb A., 1997, ApJ, 483, 21

Hamuy M., 2003, ApJ, 582, 905

Hashimoto M., Nomoto K., Shigeyama T., 1989, A&A, 210, L5

Hayashi C., Hōshi R., Sugimoto D., 1962, Progress of Theoretical Physics Supplement, 22, 1

Heger A., Woosley S. E., 2002, ApJ, 567, 532

Heger A., Woosley S. E., 2010, ApJ, 724, 341

Heger A., Langer N., Woosley S. E., 2000, ApJ, 528, 368

Heger A., Woosley S. E., Spruit H. C., 2005, ApJ, 626, 350

Heijmans J. et al., 2012, in Ground-based and Airborne Instrumentation for Astronomy IV. Proc. SPIE, Vol. 8446, p. 84460W

Hirano S., Hosokawa T., Yoshida N., Umeda H., Omukai K., Chiaki G., Yorke H. W., 2014, ApJ, 781, 60

Hirano S., Zhu N., Yoshida N., Spergel D., Yorke H. W., 2015, ApJ, 814, 18

Hirschi R., 2007, A&A, 461, 571

Hollek J. K., Frebel A., Roederer I. U., Sneden C., Shetrone M., Beers T. C., Kang S. j., Thom C., 2011, ApJ, 742, 54

Honda S., Aoki W., Kajino T., Ando H., Beers T. C., Izumiura H., Sadakane K., Takada-Hidai M., 2004, ApJ, 607, 474

Horiguchi T., Tachibana T., Koura H., Katakura J., 2000, Chart of the Nuclides (Ibaraki: Japan A. Energy Res. Inst.)

Hosokawa T., Omukai K., Yoshida N., Yorke H. W., 2011, Science, 334, 1250

Hosokawa T., Yoshida N., Omukai K., Yorke H. W., 2012, ApJ, 760, L37

Hosokawa T., Hirano S., Kuiper R., Yorke H. W., Omukai K., Yoshida N., 2016, ApJ, 824, 119

Hunter I., Lennon D. J., Dufton P. L., Trundle C., Simón-Díaz S., Smartt S. J., Ryans R. S. I., Evans C. J., 2008, A&A, 479, 541

Hunter I. et al., 2009, A&A, 496, 841

Iben Jr. I., 2013, Stellar Evolution Physics, Volume 1: Physical Processes in Stellar Interiors

Iglesias C. A., Rogers F. J., 1996, ApJ, 464, 943

Ishigaki M., Chiba M., Aoki W., 2010, PASJ, 62, 143

Ishigaki M. N., Chiba M., Aoki W., 2012, ApJ, 753, 64

Ishigaki M. N., Aoki W., Chiba M., 2013, ApJ, 771, 67

Ishigaki M. N., Tominaga N., Kobayashi C., Nomoto K., 2014, ApJ, 792, L32

Itoh N., Adachi T., Nakagawa M., Kohyama Y., Munakata H., 1989, ApJ, 339, 354

Itoh N., Kuwashima F., Munakata H., 1990, ApJ, 362, 620

Itoh N., Hayashi H., Nishikawa A., Kohyama Y., 1996, ApJS, 102, 411

Iwamoto N., Umeda H., Tominaga N., Nomoto K., Maeda K., 2005, Science, 309, 451

Janka H. T., 2012, Annual Review of Nuclear and Particle Science, 62, 407

Johnson J. A., Bolte M., 2002, ApJ, 579, L87

Johnson J. L., Bromm V., 2006, MNRAS, 366, 247

Karlsson T., Johnson J. L., Bromm V., 2008, ApJ, 679, 6-16

Kasen D., Woosley S. E., Heger A., 2011, ApJ, 734, 102

Keller S. C. et al., 2007, Publications of the Astronomical Society of Australia, 24, 1

Keller S. C. et al., 2014, Nature, 506, 463

Kifonidis K., Plewa T., Janka H. T., Müller E., 2003, A&A, 408, 621

Kinugawa T., Inayoshi K., Hotokezaka K., Nakauchi D., Nakamura T., 2014, MNRAS, 442, 2963

Kippenhahn R., 1974, in R.J. Tayler, J.E. Hesser, eds, Late Stages of Stellar Evolution. IAU Symposium, Vol. 66, p. 20

Kippenhahn R., Moellenhoff C., 1974, Ap&SS, 31, 117

Kippenhahn R., Thomas H. C., 1970, in A. Slettebak, ed., IAU Colloq. 4: Stellar Rotation. p. 20

Kippenhahn R., Weigert A., 1990, Stellar Structure and Evolution

Kitaura F. S., Janka H. T., Hillebrandt W., 2006, A&A, 450, 345

Kobayashi C., Tsujimoto T., Nomoto K., Hachisu I., Kato M., 1998, ApJ, 503, L155

Kobayashi C., Umeda H., Nomoto K., Tominaga N., Ohkubo T., 2006, ApJ, 653, 1145

Komatsu E. et al., 2011, ApJS, 192, 18

Kotake K., Sumiyoshi K., Yamada S., Takiwaki T., Kuroda T., Suwa Y., Nagakura H., 2012, Progress of Theoretical and Experimental Physics, 2012, 01A301

Kozyreva A., Blinnikov S., Langer N., Yoon S. C., 2014a, A&A, 565, A70

Kozyreva A., Yoon S. C., Langer N., 2014b, A&A, 566, A146

Krtička J., Kubát J., 2009, A&A, 493, 585

Kudritzki R. P., 2002, ApJ, 577, 389

Lai D. K., Bolte M., Johnson J. A., Lucatello S., Heger A., Woosley S. E., 2008, ApJ, 681, 1524-1556

Langanke K., Martínez-Pinedo G., 2001, Atomic Data and Nuclear Data Tables, 79, 1

Langer N., 1998, A&A, 329, 551

Lau H. H. B., Stancliffe R. J., Tout C. A., 2008, MNRAS, 385, 301

Limongi M., Chieffi A., 2012, ApJS, 199, 38

Limongi M., Chieffi A., Bonifacio P., 2003, ApJ, 594, L123

Lodders K., Palme H., Gail H. P., 2009, Landolt Börnstein

Lovegrove E., Woosley S. E., 2013, ApJ, 769, 109

Lucatello S., Tsangarides S., Beers T. C., Carretta E., Gratton R. G., Ryan S. G., 2005, ApJ, 625, 825

Maeder A., 1987, A&A, 178, 159

Maeder A., Meynet G., 2000, A&A, 361, 159

Maeder A., Meynet G., Chiappini C., 2015, A&A, 576, A56

Majewski S. R., Wilson J. C., Hearty F., Schiavon R. R., Skrutskie M. F., 2010, in K. Cunha, M. Spite, B. Barbuy, eds, Chemical Abundances in the Universe: Connecting First Stars to Planets. IAU Symposium, Vol. 265, pp. 480–481

Marigo P., Girardi L., Chiosi C., Wood P. R., 2001, A&A, 371, 152

Marigo P., Chiosi C., Kudritzki R. P., 2003, A&A, 399, 617

McKee C. F., Tan J. C., 2008, ApJ, 681, 771

McWilliam A., Preston G. W., Sneden C., Searle L., 1995, AJ, 109, 2757

Meynet G., Maeder A., 1997, A&A, 321, 465

Meynet G., Maeder A., 2000, A&A, 361, 101

Meynet G., Maeder A., 2002a, A&A, 390, 561

Meynet G., Maeder A., 2002b, A&A, 381, L25

Meynet G., Ekström S., Maeder A., 2006, A&A, 447, 623

Meynet G., Hirschi R., Ekstrom S., Maeder A., Georgy C., Eggenberger P., Chiappini C., 2010, A&A, 521, A30

Misner C. W., Sharp D. H., 1964, Physical Review, 136, 571

Miyaji S., Nomoto K., Yokoi K., Sugimoto D., 1980, PASJ, 32, 303

Morel T., Hubrig S., Briquet M., 2008, A&A, 481, 453

Moriya T. J., Langer N., 2015, A&A, 573, A18

Nadezhin D. K., 1980, Ap&SS, 69, 115

Nomoto K., Thielemann F. K., Yokoi K., 1984, ApJ, 286, 644

Nomoto K., Tominaga N., Umeda H., Kobayashi C., Maeda K., 2006, Nuclear Physics A, 777, 424

Nomoto K., Kobayashi C., Tominaga N., 2013, ARA&A, 51, 457

Norris J. E. et al., 2013, ApJ, 762, 28

Oda T., Hino M., Muto K., Takahara M., Sato K., 1994, Atomic Data and Nuclear Data Tables, 56, 231

Ohkubo T., Umeda H., Maeda K., Nomoto K., Suzuki T., Tsuruta S., Rees M. J., 2006, ApJ, 645, 1352

Omukai K., 2001, ApJ, 546, 635

Omukai K., Nishi R., 1998a, ApJ, 508, 141

Omukai K., Nishi R., 1998b, ApJ, 508, 141

Omukai K., Palla F., 2001, ApJ, 561, L55

Omukai K., Yoshii Y., 2003, ApJ, 599, 746

Paxton B., Bildsten L., Dotter A., Herwig F., Lesaffre P., Timmes F., 2011, ApJS, 192, 3

Paxton B. et al., 2013, ApJS, 208, 4

Picardi I., Chieffi A., Limongi M., Pisanti O., Miele G., Mangano G., Imbriani G., 2004, ApJ, 609, 1035

Pinsonneault M. H., Kawaler S. D., Sofia S., Demarque P., 1989, ApJ, 338, 424

Placco V. M., Frebel A., Beers T. C., Christlieb N., Lee Y. S., Kennedy C. R., Rossi S., Santucci R. M., 2014, ApJ, 781, 40

Planck Collaboration et al., 2014, A&A, 571, A1

Potekhin A. Y., Chabrier G., Lai D., Ho W. C. G., van Adelsberg M., 2006, Journal of Physics A Mathematical General, 39, 4453

Rakavy G., Shaviv G., Zinamon Z., 1967, ApJ, 150, 131

Ren J., Christlieb N., Zhao G., 2012, Research in Astronomy and Astrophysics, 12, 1637

Ritter J. S., Safranek-Shrader C., Gnat O., Milosavljević M., Bromm V., 2012, ApJ, 761, 56

Ritter J. S., Safranek-Shrader C., Milosavljević M., Bromm V., 2016, MNRAS, 463, 3354

Roe P. L., 1981, Journal of Computational Physics, 43, 357

Roederer I. U., Preston G. W., Thompson I. B., Shectman S. A., Sneden C., Burley G. S., Kelson D. D., 2014, AJ, 147, 136

Roederer I. U., Cowan J. J., Karakas A. I., Kratz K. L., Lugaro M., Simmerer J., Farouqi K., Sneden C., 2010, ApJ, 724, 975

Ryan S. G., Norris J. E., Beers T. C., 1996, ApJ, 471, 254

Salpeter E. E., van Horn H. M., 1969, ApJ, 155, 183

Scannapieco E., Madau P., Woosley S., Heger A., Ferrara A., 2005, ApJ, 633, 1031

Schaerer D., 2002, A&A, 382, 28

Shigeyama T., Tsujimoto T., Yoshii Y., 2003, ApJ, 586, L57

Siess L., Livio M., Lattanzio J., 2002, ApJ, 570, 329

Siqueira Mello C. et al., 2014, A&A, 565, A93

Slattery W. L., Doolen G. D., Dewitt H. E., 1982, Phys. Rev. A, 26, 2255

Smidt J., Whalen D. J., Chatzopoulos E., Wiggins B., Chen K. J., Kozyreva A., Even W., 2015, ApJ, 805, 44

Smith B. D., Wise J. H., O'Shea B. W., Norman M. L., Khochfar S., 2015, MNRAS, 452, 2822

Song H. F., Meynet G., Maeder A., Ekström S., Eggenberger P., 2016, A&A, 585, A120

Sonoi T., Umeda H., 2012, MNRAS, 421, L34

Spite M. et al., 2011, A&A, 528, A9

Spruit H. C., 1992, A&A, 253, 131

Spruit H. C., 2002, A&A, 381, 923

Stacy A., Bromm V., 2013, MNRAS, 433, 1094

Stacy A., Greif T. H., Bromm V., 2010, MNRAS, 403, 45

Stacy A., Bromm V., Loeb A., 2011, MNRAS, 413, 543

Stacy A., Greif T. H., Klessen R. S., Bromm V., Loeb A., 2013, MNRAS, 431, 1470

Steigman G., 2007, Annual Review of Nuclear and Particle Science, 57, 463

Suda T., Aikawa M., Machida M. N., Fujimoto M. Y., Iben Jr. I., 2004, ApJ, 611, 476

Suda T., Yamada S., Katsuta Y., Komiya Y., Ishizuka C., Aoki W., Fujimoto M. Y., 2011, MNRAS, 412, 843

Suda T. et al., 2008, PASJ, 60, 1159

Sukhbold T., Woosley S. E., 2014, ApJ, 783, 10

Sumiyoshi K., Suzuki H., Otsuki K., Terasawa M., Yamada S., 2000, PASJ, 52, 601

Susa H., Hasegawa K., Tominaga N., 2014, ApJ, 792, 32

Takahashi K., Yokoi K., 1987, Atomic Data and Nuclear Data Tables, 36, 375

Takahashi K., Yoshida T., Umeda H., 2013, ApJ, 771, 28

Takahashi K., Umeda H., Yoshida T., 2014, ApJ, 794, 40

Takahashi K., Yoshida T., Umeda H., Sumiyoshi K., Yamada S., 2016, MNRAS, 456, 1320

Tan J. C., McKee C. F., 2004, ApJ, 603, 383

Timmes F. X., Swesty F. D., 2000, ApJS, 126, 501

Timmes F. X., Woosley S. E., Weaver T. A., 1995, ApJS, 98, 617

Toki H., Suzuki T., Nomoto K., Jones S., Hirschi R., 2013, Phys. Rev. C, 88, 015806

Tominaga N., 2009, ApJ, 690, 526

Tominaga N., Umeda H., Nomoto K., 2007a, ApJ, 660, 516

Tominaga N., Iwamoto N., Nomoto K., 2014, ApJ, 785, 98

Tominaga N., Maeda K., Umeda H., Nomoto K., Tanaka M., Iwamoto N., Suzuki T., Mazzali P. A., 2007b, ApJ, 657, L77

Totani T., Morokuma T., Oda T., Doi M., Yasuda N., 2008, PASJ, 60, 1327

94

Tumlinson J., Shull J. M., 2000, ApJ, 528, L65

Ugliano M., Janka H. T., Marek A., Arcones A., 2012, ApJ, 757, 69

Umeda H., Nomoto K., 2002, ApJ, 565, 385

Umeda H., Nomoto K., 2003, Nature, 422, 871

Umeda H., Nomoto K., 2005, ApJ, 619, 427

Umeda H., Yoshida T., Takahashi K., 2012, Progress of Theoretical and Experimental Physics, 2012, 01A302

Weiss A., Schlattl H., Salaris M., Cassisi S., 2004, A&A, 422, 217

Whalen D. J. et al., 2013, ApJ, 777, 110

Wiescher M., Görres J., Schatz H., 1999, Journal of Physics G Nuclear Physics, 25, 133

Wongwathanarat A., Müller E., Janka H. T., 2015, A&A, 577, A48

Woosley S. E., Heger A., 2006, ApJ, 637, 914

Woosley S. E., Weaver T. A., 1986, ARA&A, 24, 205

Woosley S. E., Weaver T. A., 1995, ApJS, 101, 181

Yamada S., 1997, ApJ, 475, 720

Yamada S., Janka H. T., Suzuki H., 1999, A&A, 344, 533

Yamada S., Suda T., Komiya Y., Aoki W., Fujimoto M. Y., 2013, MNRAS, 436, 1362

Yanny B. et al., 2009, AJ, 137, 4377

Yasutake N., Fujisawa K., Yamada S., 2015, MNRAS, 446, L56

Yong D. et al., 2013a, ApJ, 762, 26

Yong D. et al., 2013b, ApJ, 762, 27

Yoon S. C., Langer N., 2005, A&A, 443, 643

Yoon S. C., Langer N., Norman C., 2006, A&A, 460, 199

Yoon S. C., Woosley S. E., Langer N., 2010, ApJ, 725, 940

Yoon S. C., Dierks A., Langer N., 2012, A&A, 542, A113

Yoon S. C., Kang J., Kozyreva A., 2015, ApJ, 802, 16

Yoshida N., Abel T., Hernquist L., Sugiyama N., 2003, ApJ, 592, 645

Yoshida N., Bromm V., Hernquist L., 2004, ApJ, 605, 579

Yoshida N., Oh S. P., Kitayama T., Hernquist L., 2007, ApJ, 663, 687

Yoshida N., Omukai K., Hernquist L., 2008, Science, 321, 669

Yoshida T., Umeda H., 2011, MNRAS, 412, L78

Yoshida T., Umeda H., Maeda K., Ishii T., 2016, MNRAS, 457, 351

Yoshii Y., 1981, A&A, 97, 280

Yoshii Y., Tsujimoto T., Nomoto K., 1996, ApJ, 462, 266

Zahn J. P., 1992, A&A, 265, 115

Appendix A

Relations on the thermodynamic functions

A.1 Definitions of mass densities, number densities, and mole fractions

When reactions occur, rest mass density becomes a non-conserved variable. Instead of the rest mass density, one may define the baryon number density n_b as the new conserved variable, employing the baryon number conservation as the new conservation law. Using the baryon number density, pseudo mass density, or also called as the baryon mass density, can be defined as $\rho_b \equiv m_u n_b$, which also conserves regardless of reactions.

The baryon number density is related with the number density of ion, which has the mass number of A_i, as

$$n_b = \sum_{\text{ion}} A_i n_i. \tag{A.1}$$

Ionic mole fraction Y_i and mass fraction X_i are defined as

$$Y_i \equiv n_i/n_b \tag{A.2}$$
$$X_i \equiv \rho_i/\rho_b, \tag{A.3}$$

where $\rho_i \equiv A_i m_u n_i$ is pseudo mass density of i-th ion. Thus, a relation

$$Y_i = X_i/A_i \tag{A.4}$$

holds. Using the conservation relation $\sum_{\text{ion}} X_i = 1$, one may use the mass fractions as dependent variables for chemical composition.

One may define the net electron number density and the net electron mole fraction as

$$n_e \equiv \sum_{\text{ion}} Z_i n_i \tag{A.5}$$
$$Y_e \equiv n_e/n_b \tag{A.6}$$
$$= \sum_{\text{ion}} Z_i Y_i, \tag{A.7}$$

where Z_i is charge number of i-th ion. Via charge neutrality, the net electron number density is related with number densities of electron n_{e^-} and positron n_{e^+} as

$$n_e = n_{e^-} - n_{e^+}. \tag{A.8}$$

Like an ionic mole fraction, electron and positron mole fractions are defined as

$$Y_{e^-} \equiv n_{e^-}/n_b, \tag{A.9}$$
$$Y_{e^+} \equiv n_{e^+}/n_b. \tag{A.10}$$

Then, the relation

$$Y_e = Y_{e^-} - Y_{e^+} \tag{A.11}$$

is obtained.

Rest mass density of gas composed of photon, ions, electron, and positron are written as

$$\rho = \sum_{\text{ion}} m_i n_i + m_{e^-} n_{e^-} + m_{e^+} n_{e^+}. \tag{A.12}$$

Equating with above relations, one may obtain

$$\frac{\rho c^2}{\rho_b} = \frac{1}{m_u}\left[\sum_{\text{ion}} m_i c^2 Y_i + m_e c^2 Y_e + 2 m_e c^2 Y_{e^+}\right], \tag{A.13}$$

where the relation $m_e \equiv m_{e^-} = m_{e^+}$ is used. In the right hand side, a reaction only changes the mole fractions, and thus the equation gives a simple way to calculate the change of the rest mass per baryon by reactions.

A.2 The first law of thermodynamics

Macroscopic expression of the first law of thermodynamics is

$$\mathrm{d}E^{\text{rel}} = T\mathrm{d}S - p\mathrm{d}V + \sum_{\text{particles}} \mu_i^{\text{rel}}\mathrm{d}N_i, \tag{A.14}$$

where E^{rel} is the total relativistic internal energy, S is the total entropy, V is the volume, and N_i is the number of i-th particle contained in the system. One may define a total baryon number in the system, $N_b \equiv \sum_{\text{ion}} A_i N_i$, as a constant value. Then, specific densities of the relativistic internal energy, the entropy, the volume, and the number fractions are defined as

$$e^{\text{rel}} \equiv E^{\text{rel}}/(m_u N_b) \tag{A.15}$$
$$s \equiv S/(m_u N_b) \tag{A.16}$$
$$1/\rho_b \equiv V/(m_u N_b) \tag{A.17}$$
$$Y_i \equiv N_i/N_b. \tag{A.18}$$

Using these specific densities, the first law of thermodynamics in the specific density form,

$$\mathrm{d}e^{\mathrm{rel}} = T\mathrm{d}s - p\mathrm{d}\left(\frac{1}{\rho_b}\right) + \frac{1}{m_u}\sum_{\text{particles}}\mu_i^{\mathrm{rel}}\mathrm{d}Y_i, \tag{A.19}$$

is obtained.

Appendix B

Kippenhahn diagrams of massive first stars
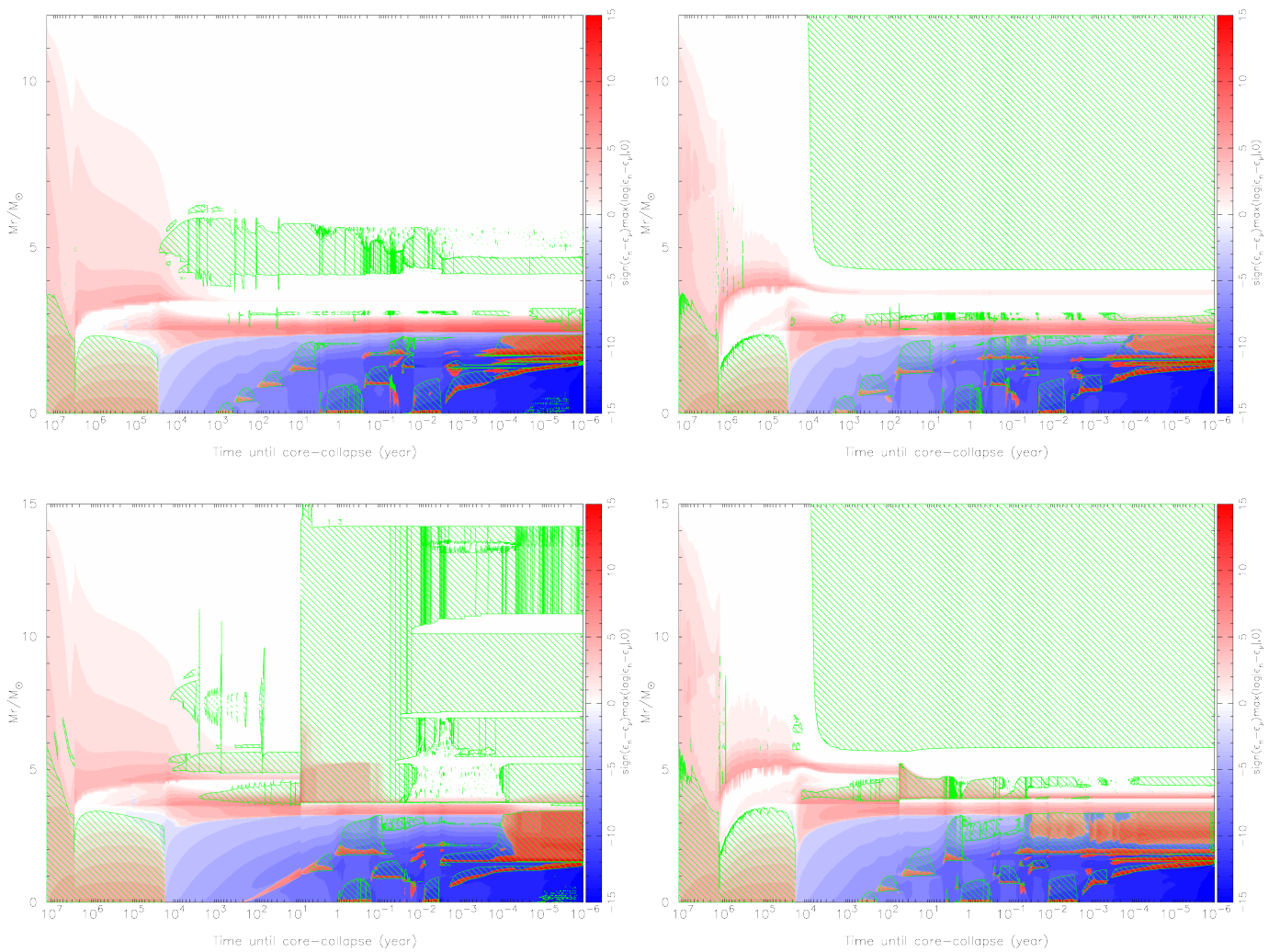
Figure B.1: Kippenhahn diagrams of the non-rotating (left) and rotating (right) 12 M$_\odot$ (top) and 15 M$_\odot$ (bottom) models.
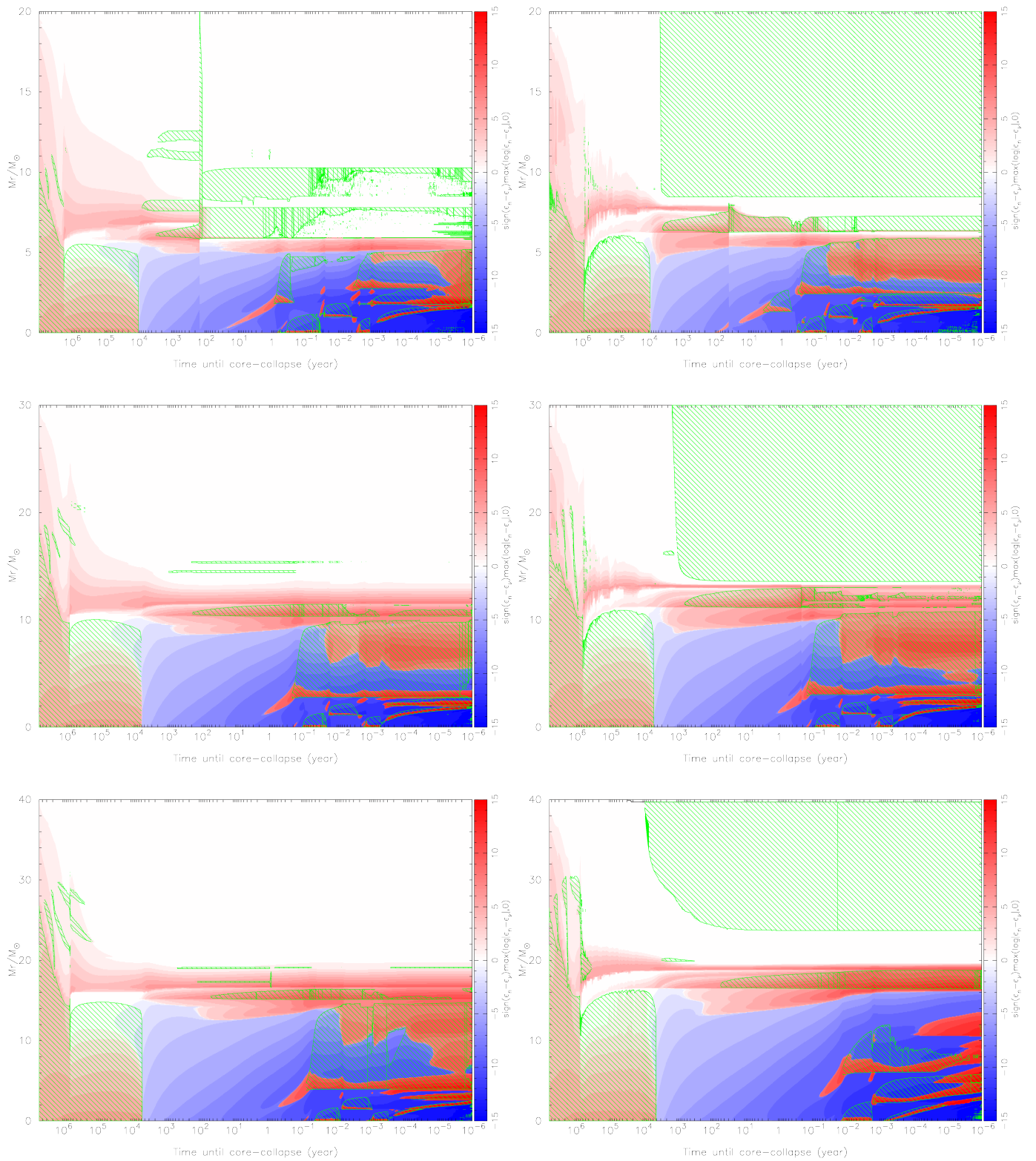
Figure B.2: Kippenhahn diagrams of the non-rotating (left) and rotating (right) 20 M$_\odot$ (top), 30 M$_\odot$ (middle), and 40 M$_\odot$ (bottom) models.
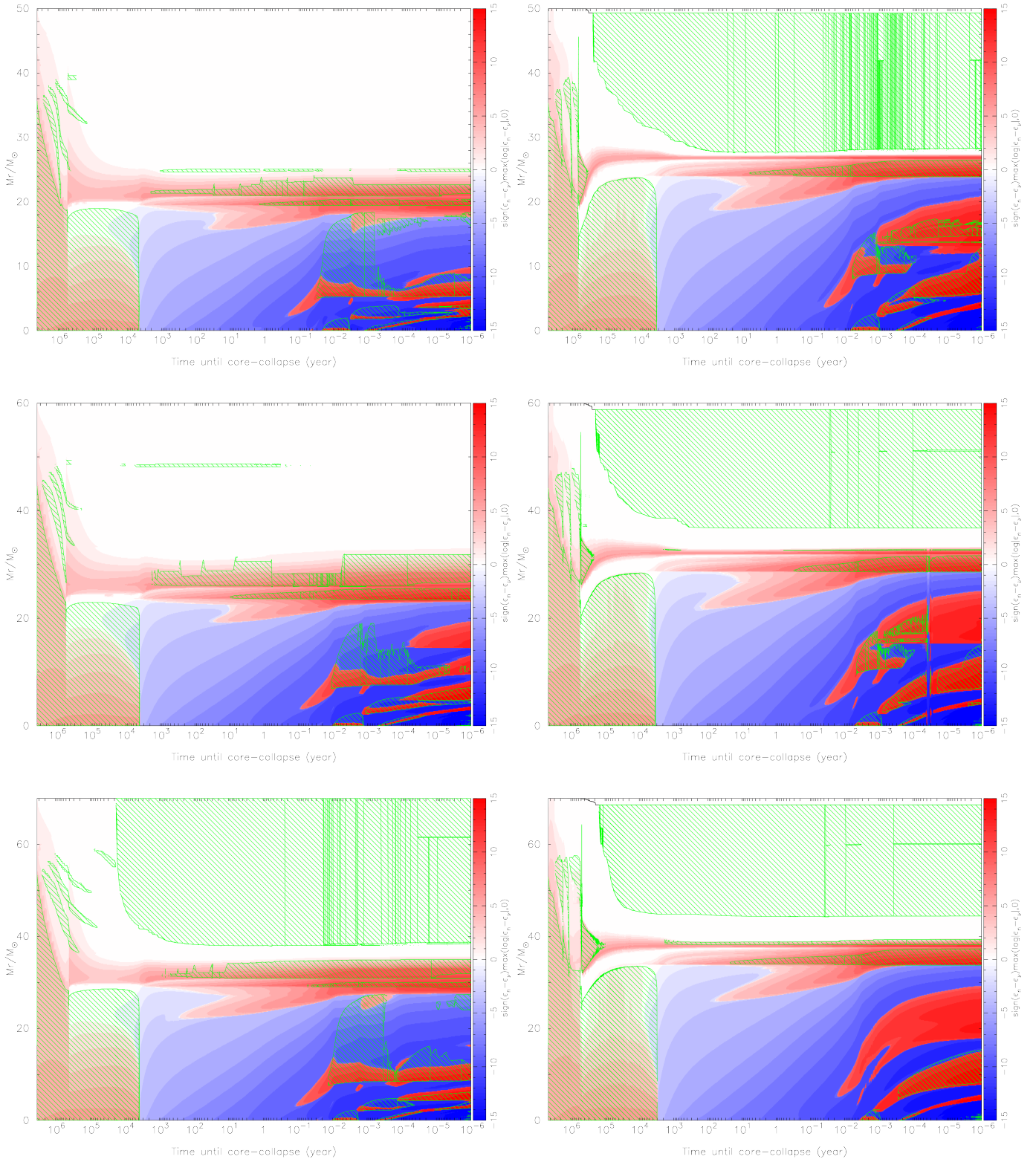
Figure B.3: Kippenhahn diagrams of the non-rotating (left) and rotating (right) 50 M$_\odot$ (top), 60 M$_\odot$ (middle), and 70 M$_\odot$ (bottom) models.
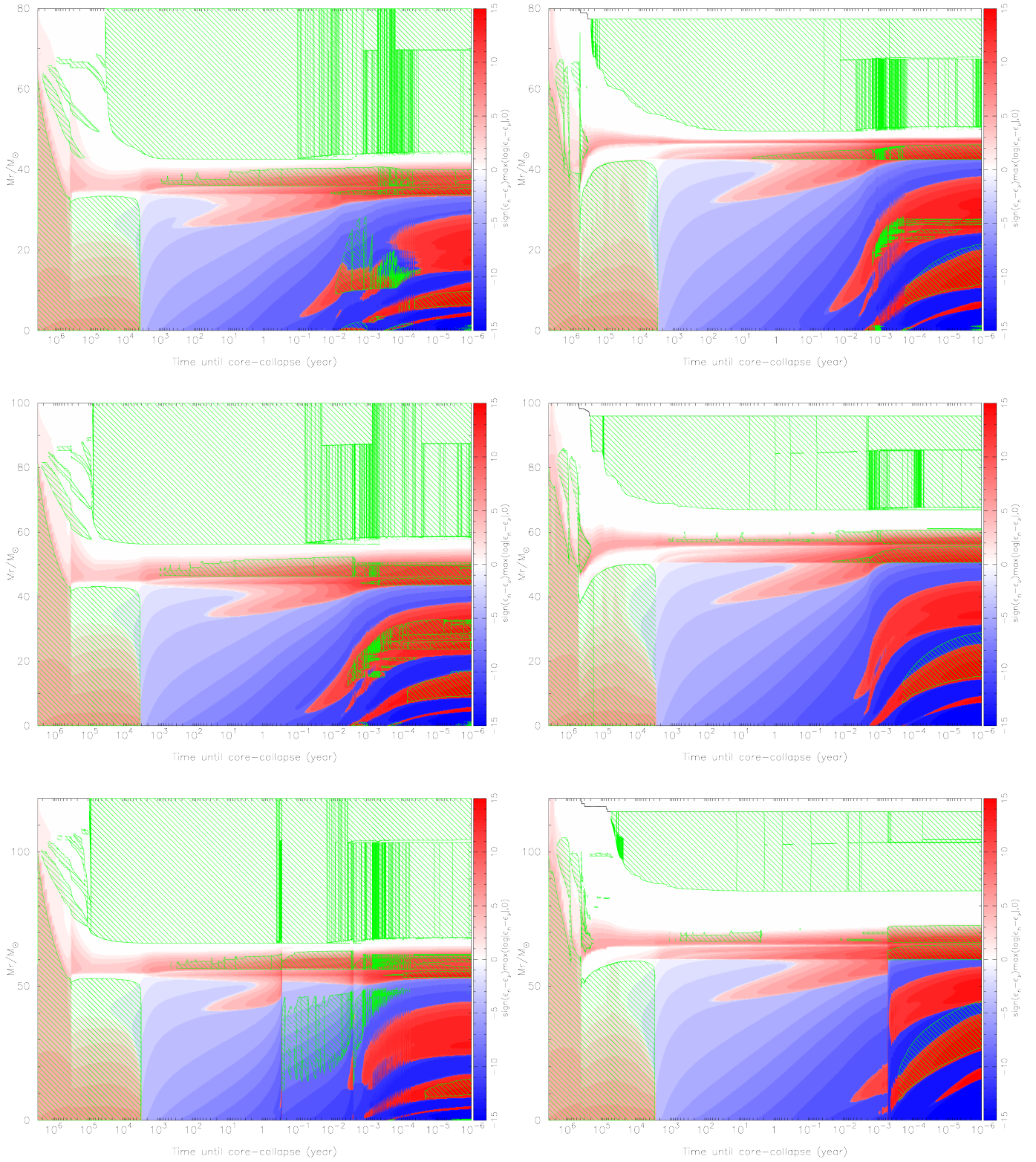
Figure B.4: Kippenhahn diagrams of the non-rotating (left) and rotating (right) 80 M$_\odot$ (top), 100 M$_\odot$ (middle), and 120 M$_\odot$ (bottom) models.
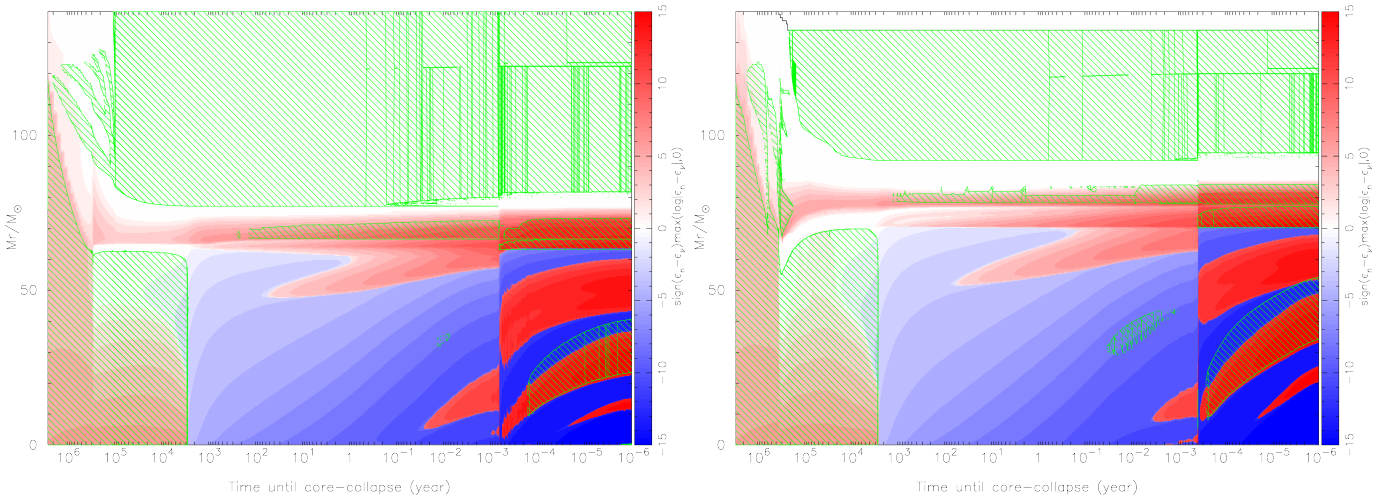
Figure B.5: Kippenhahn diagrams of the non-rotating (left) and rotating (right) 140 M$_\odot$ models.

Appendix C

Abundance patterns of metal-poor stars
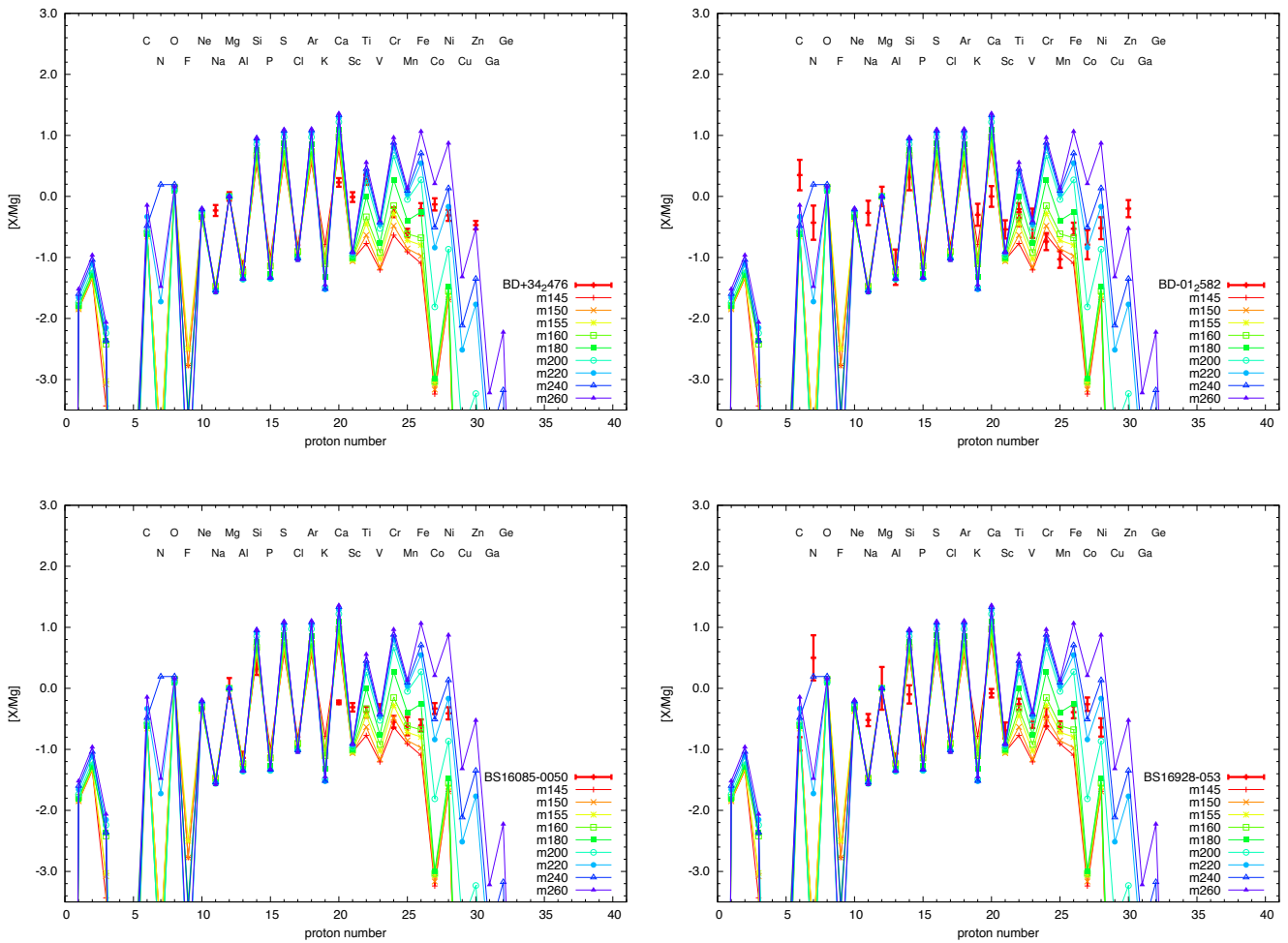
Figure C.1: The abundance patterns of selected metal-poor stars. Red thick crosses show observed values. Stars of #1–4 in Tab. 5.4 are plotted.
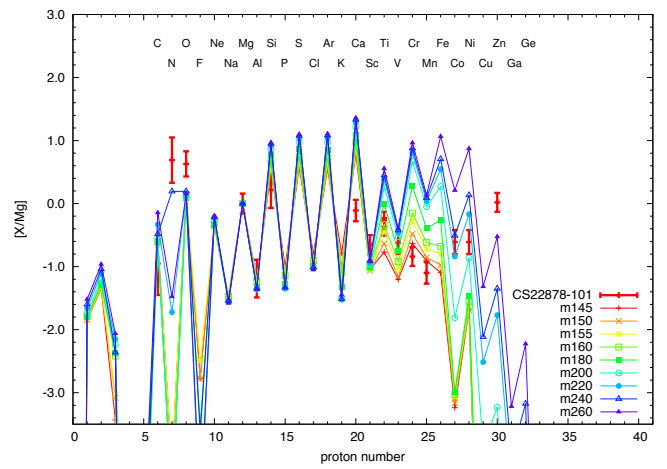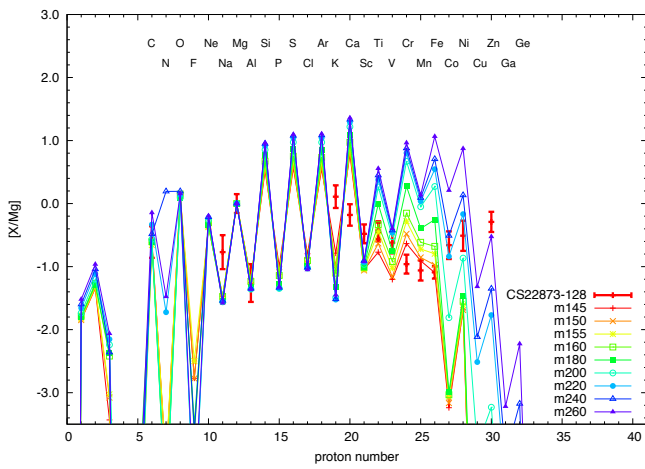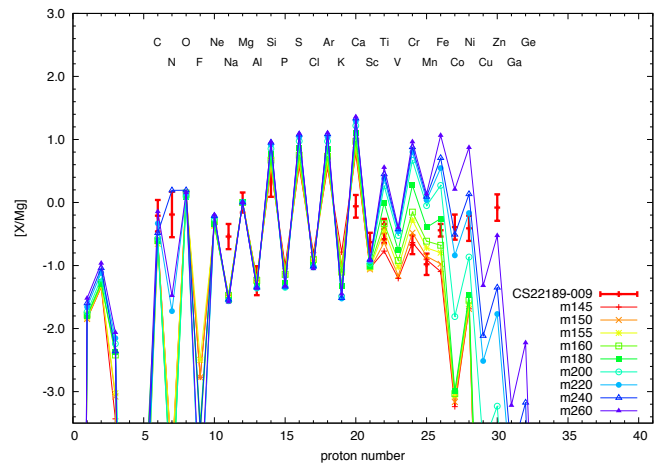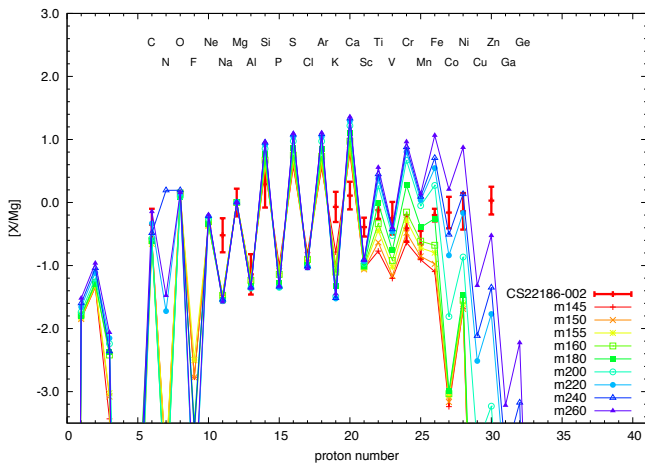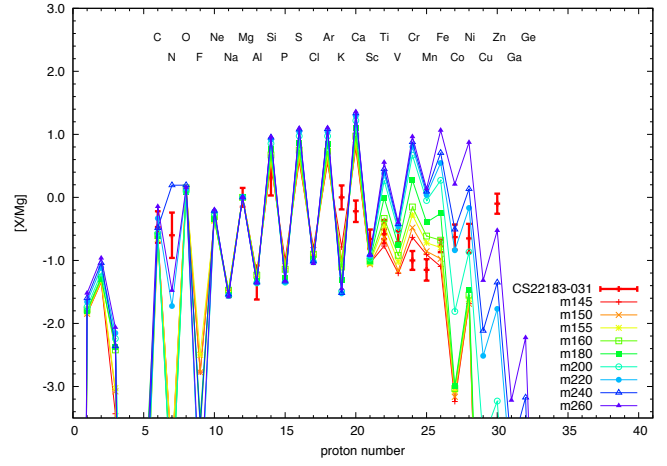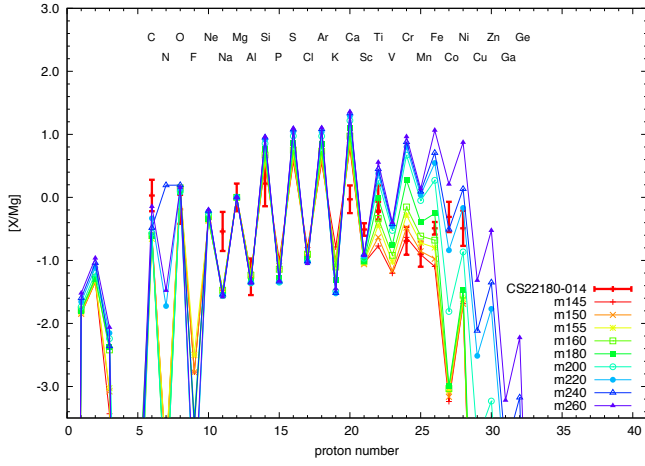
Figure C.2: Same as C.1. Stars of #5–10 in Tab. 5.4 are plotted.
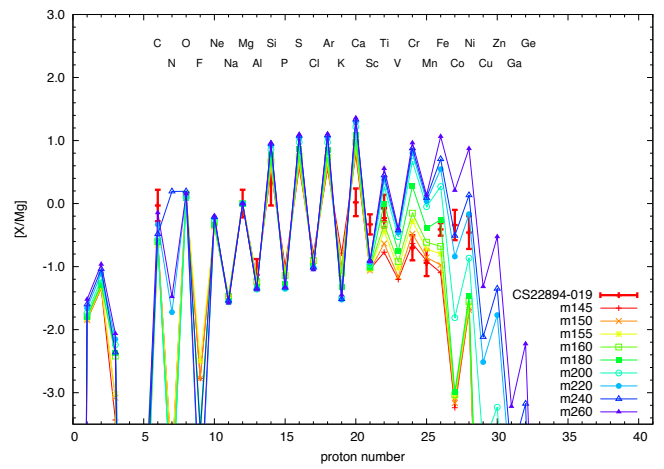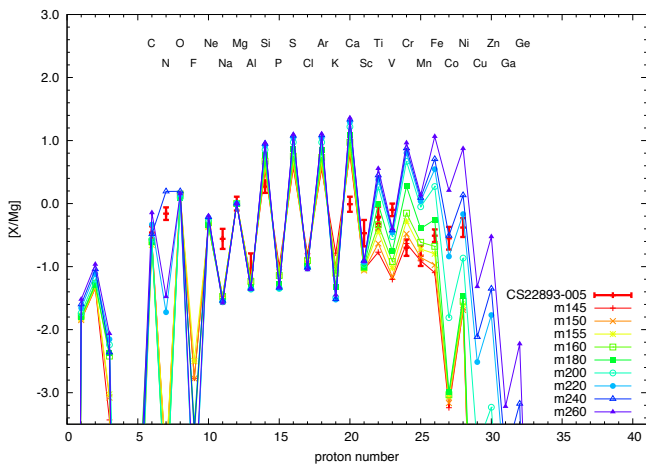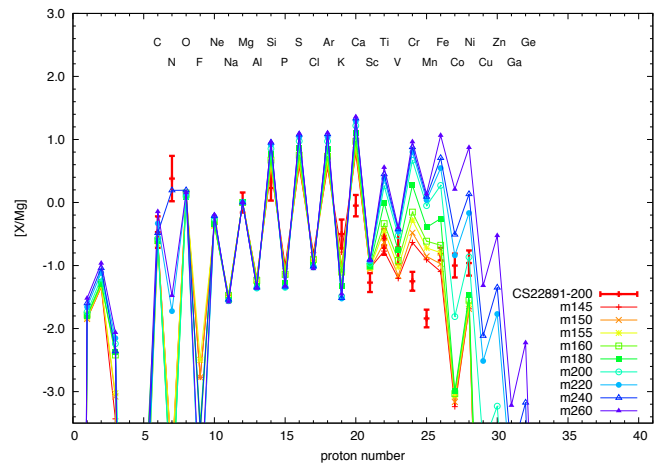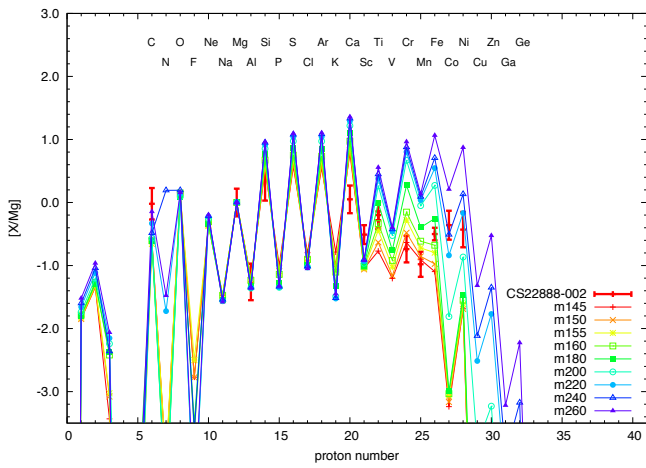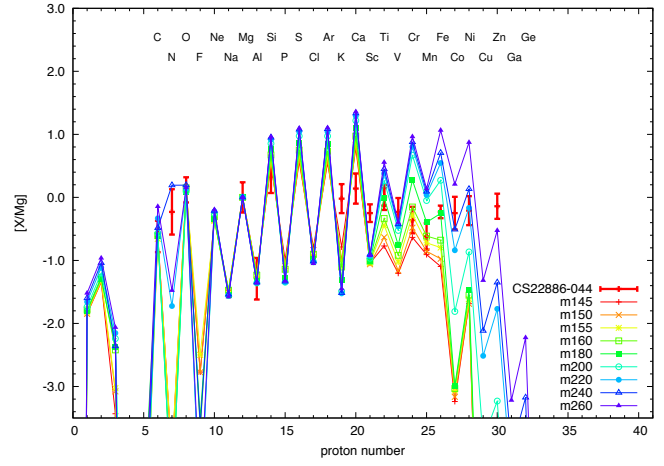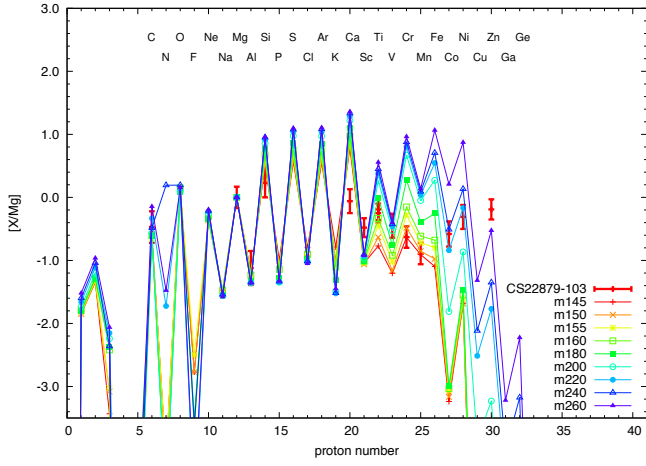
Figure C.3: Same as C.1. Stars of #11–16 in Tab. 5.4 are plotted.
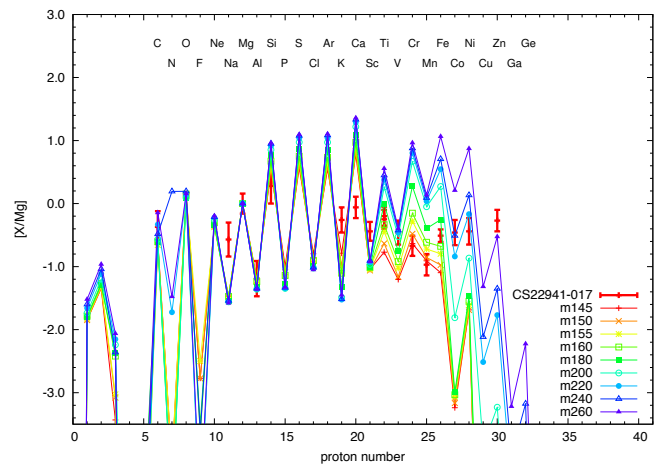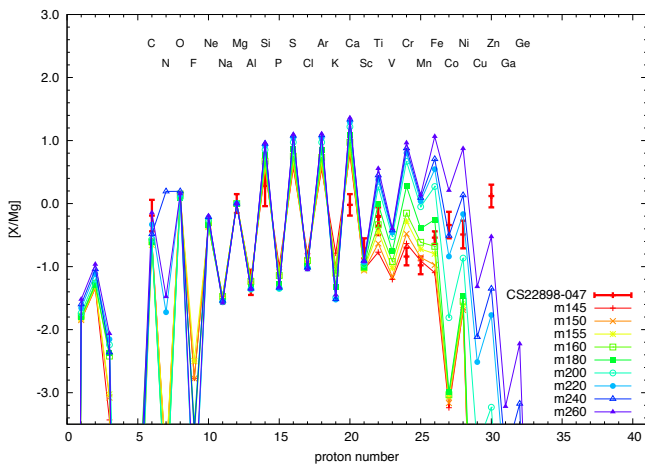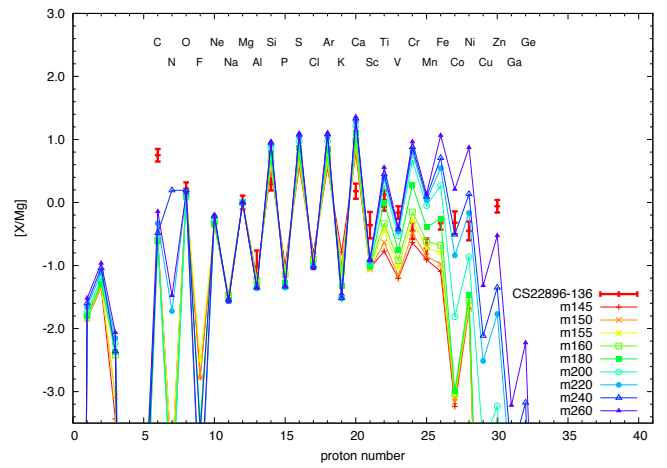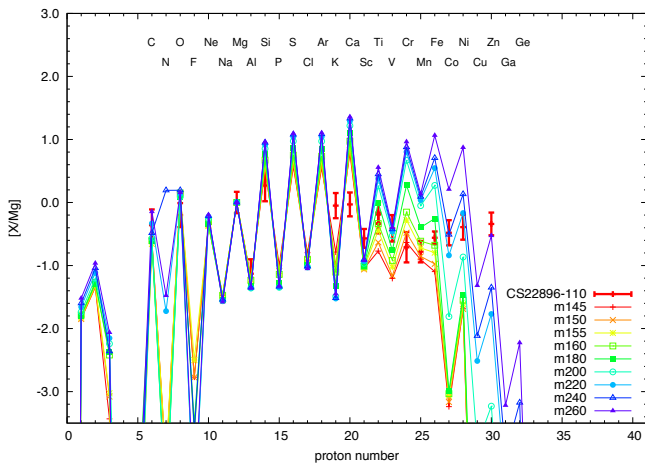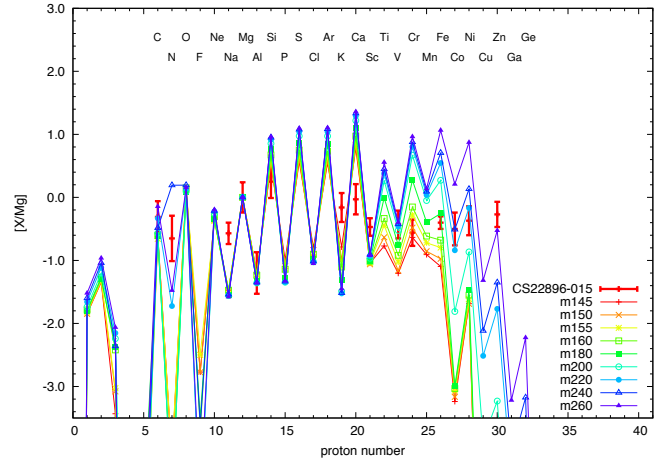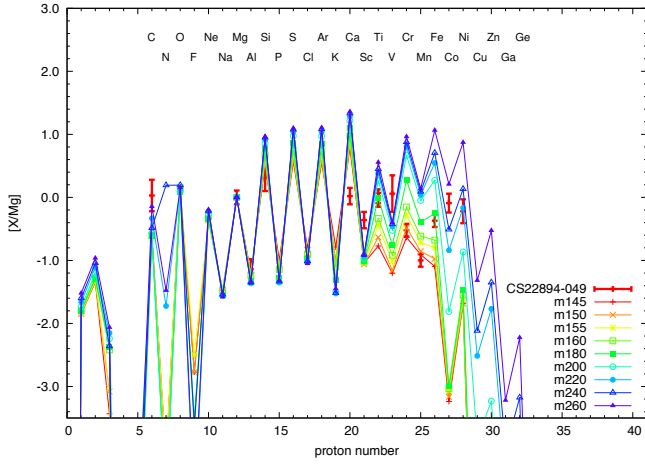
Figure C.4: Same as C.1. Stars of #17–22 in Tab. 5.4 are plotted.
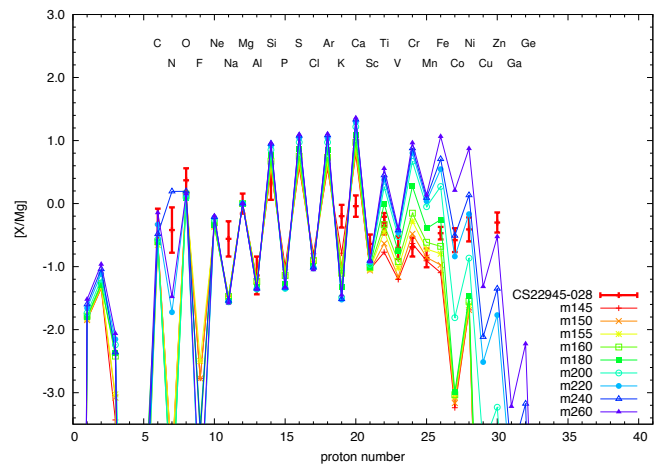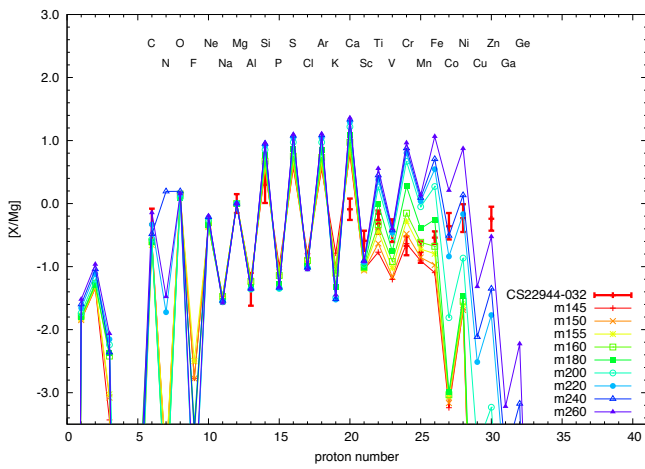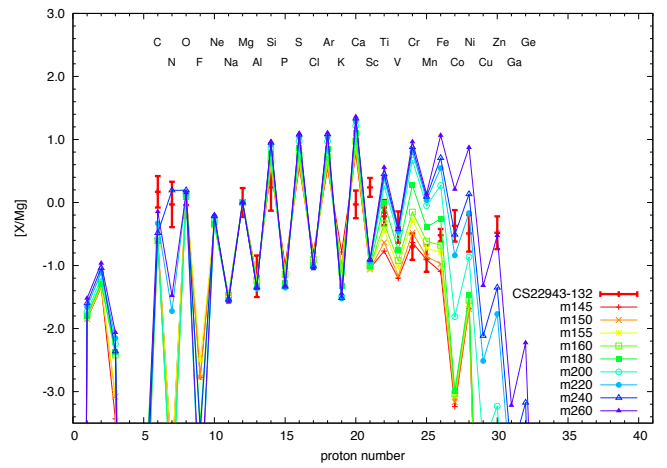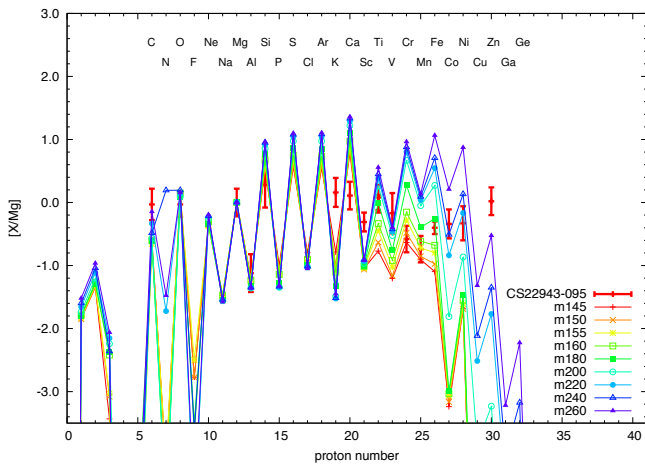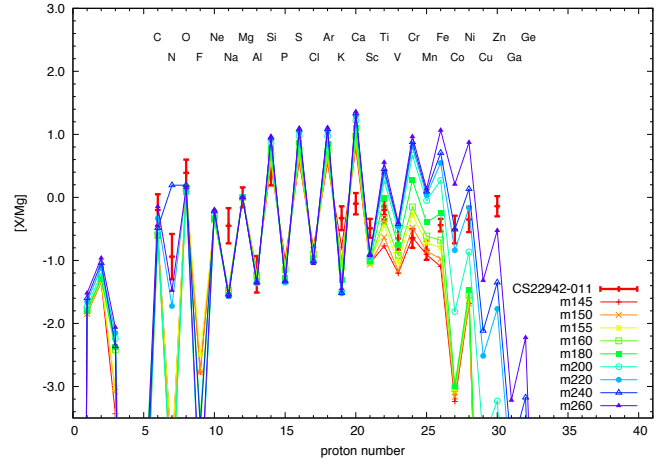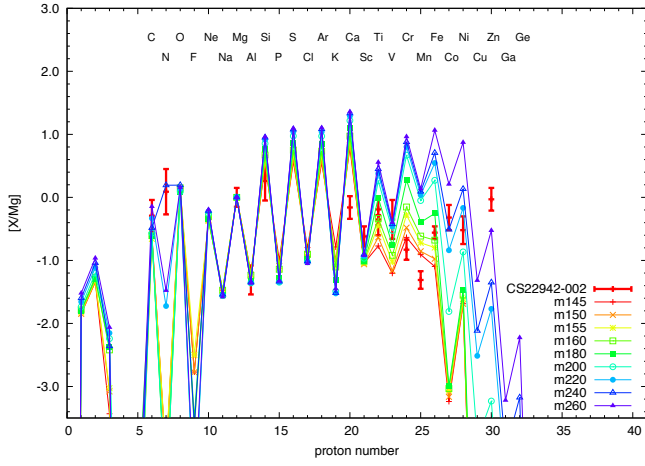
Figure C.5: Same as C.1. Stars of #23–28 in Tab. 5.4 are plotted.
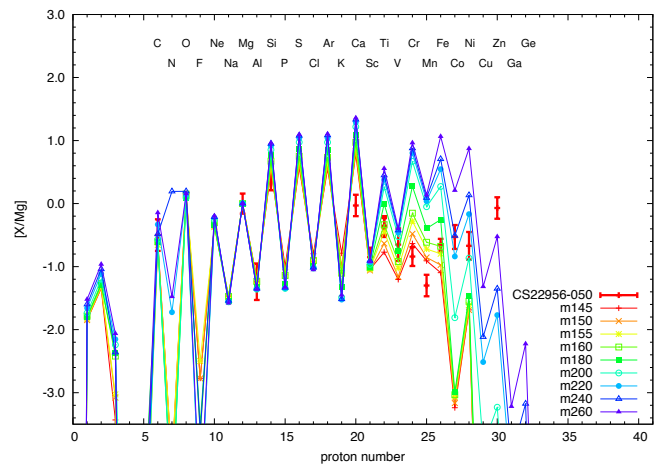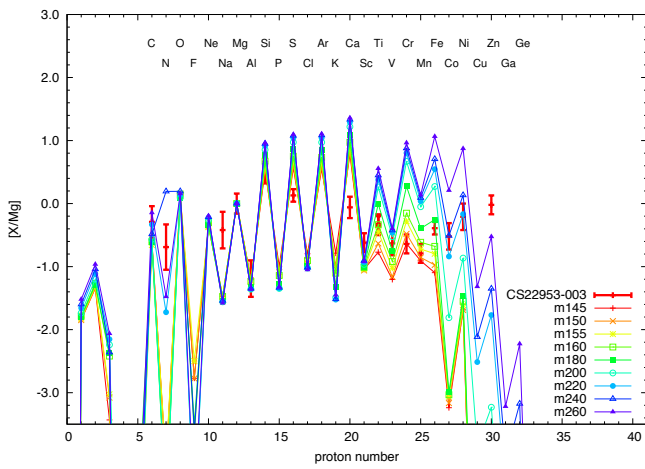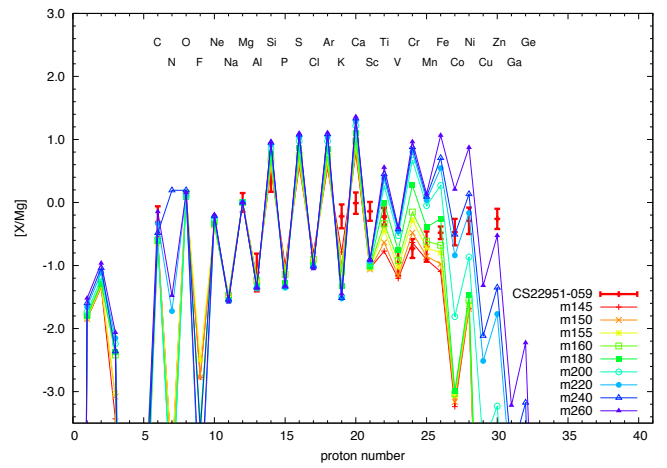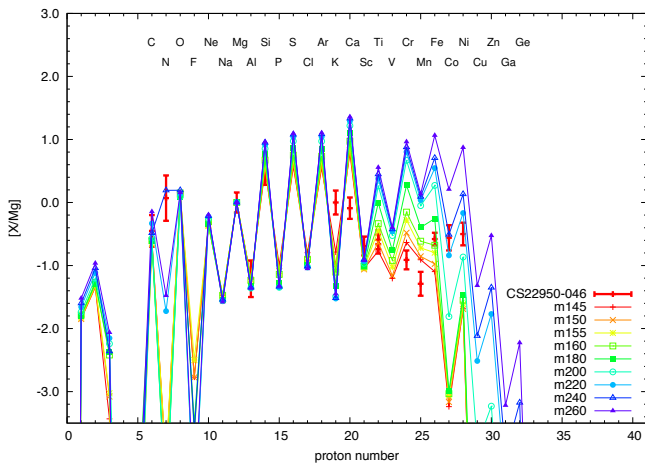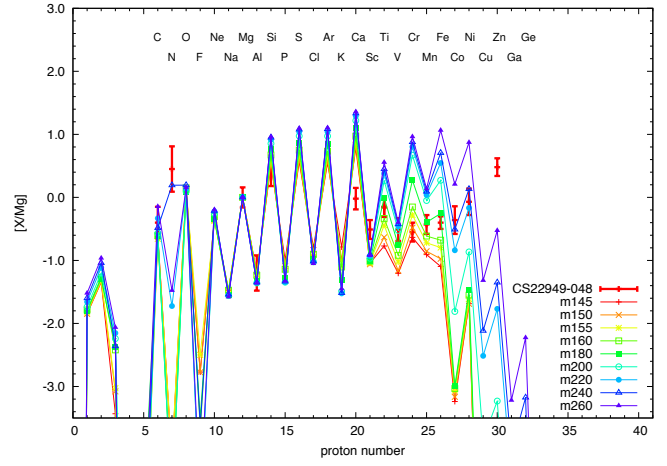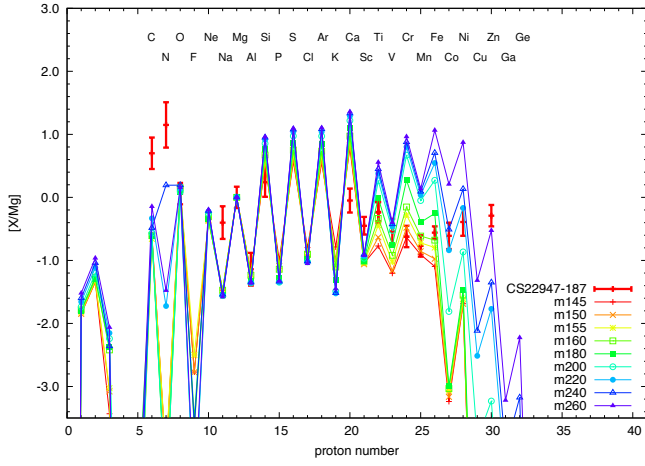
Figure C.6: Same as C.1. Stars of #29–34 in Tab. 5.4 are plotted.
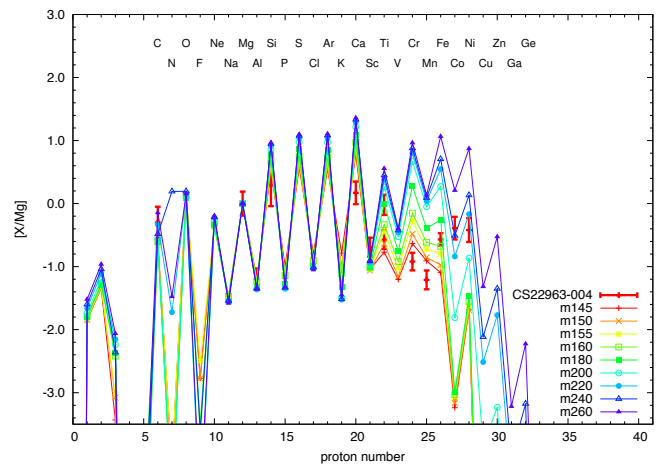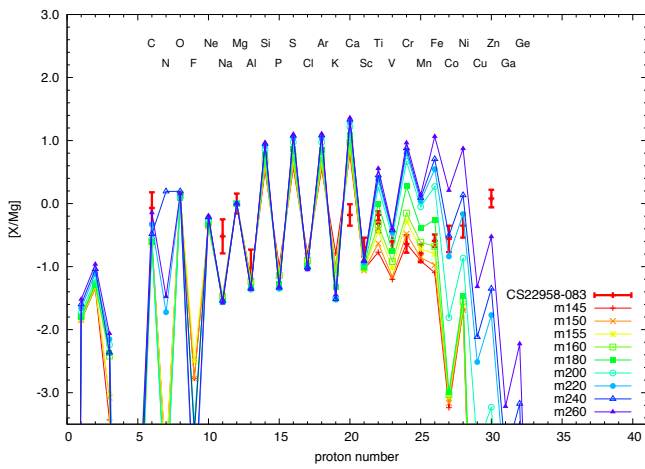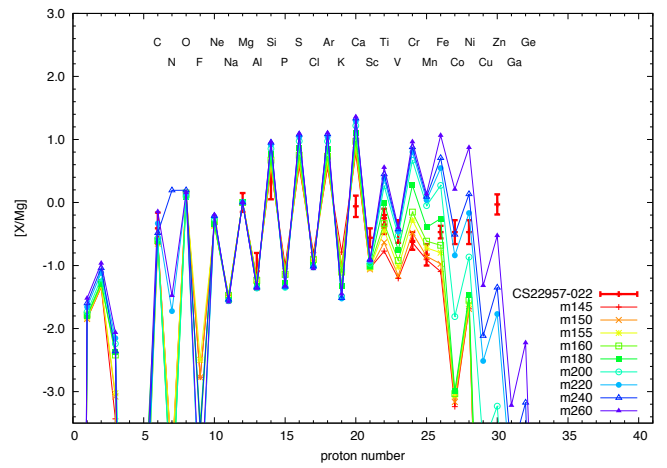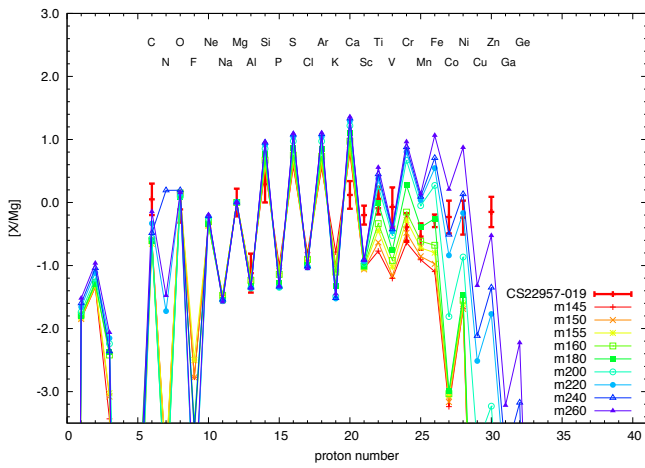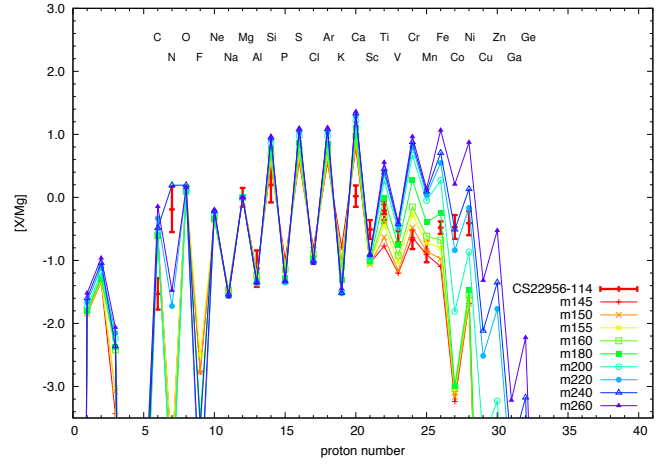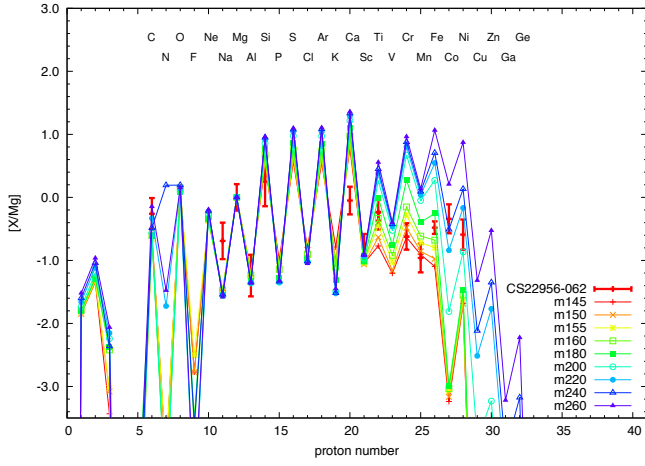
Figure C.7: Same as C.1. Stars of #35–40 in Tab. 5.4 are plotted.
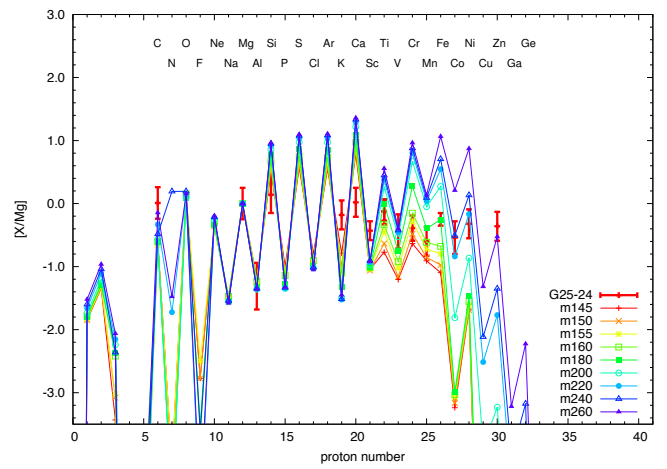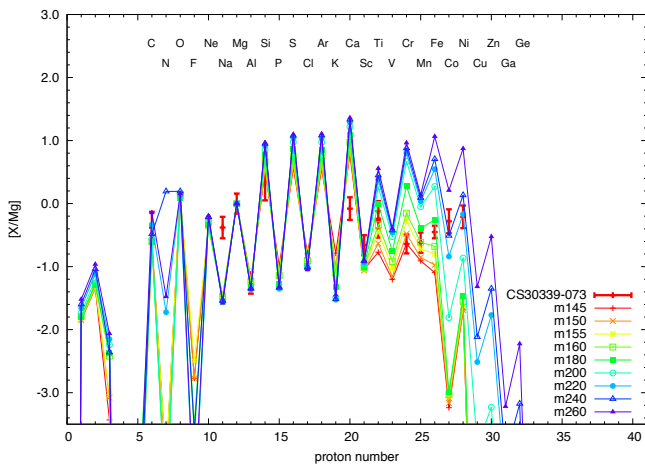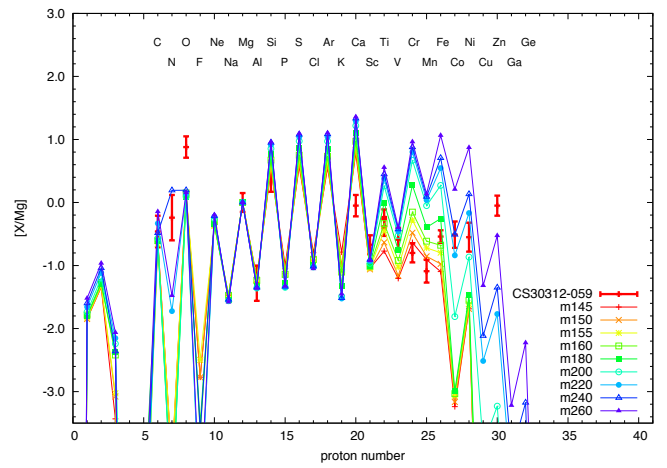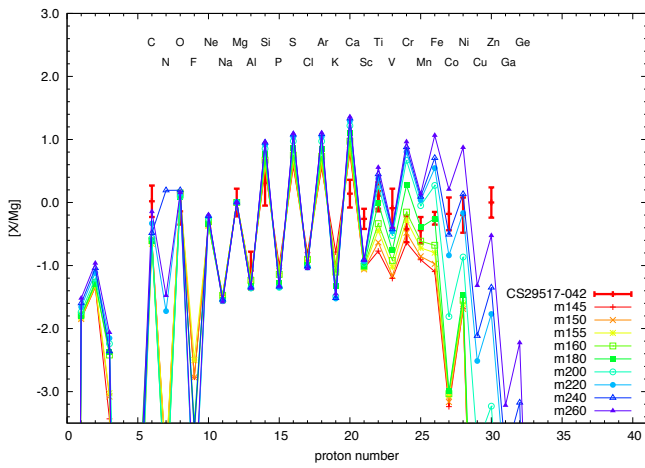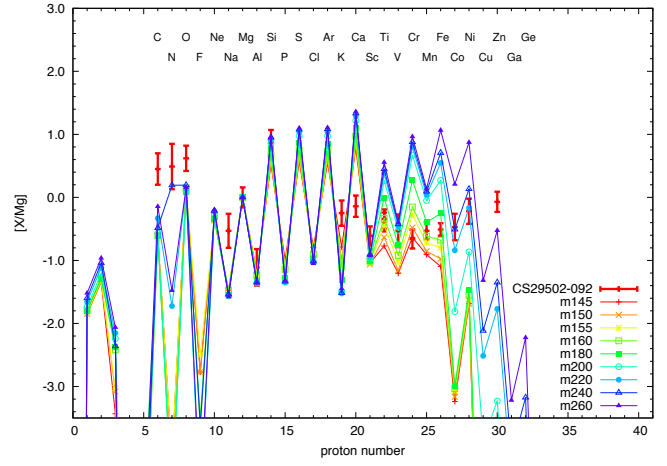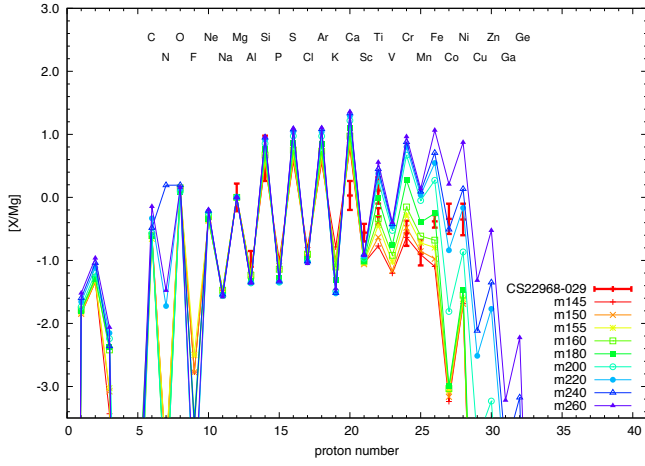
Figure C.8: Same as C.1. Stars of #41–46 in Tab. 5.4 are plotted.
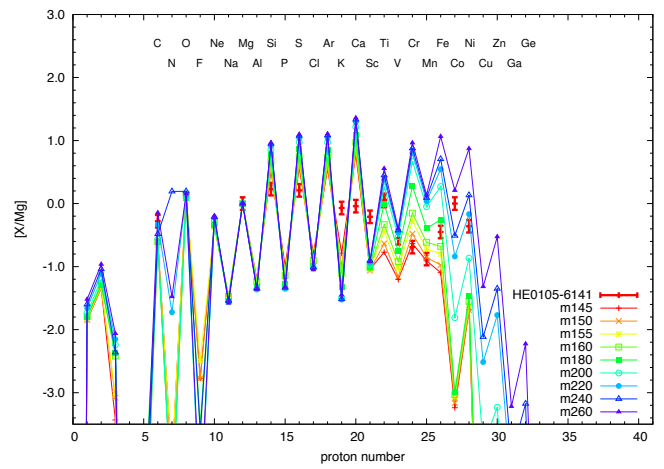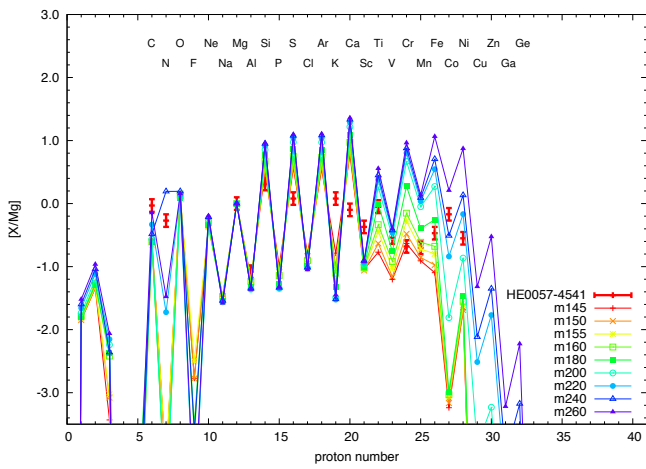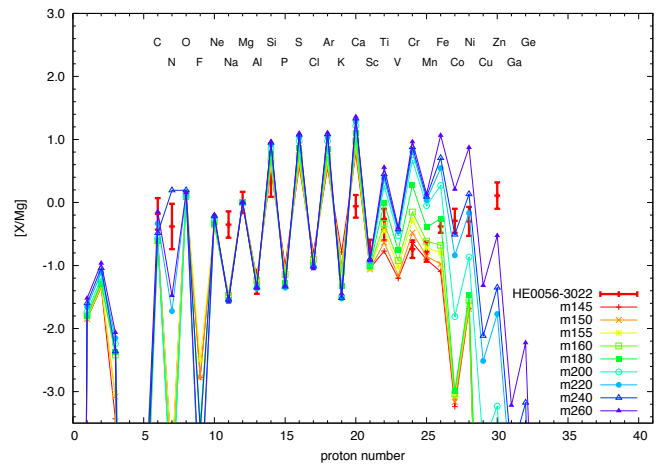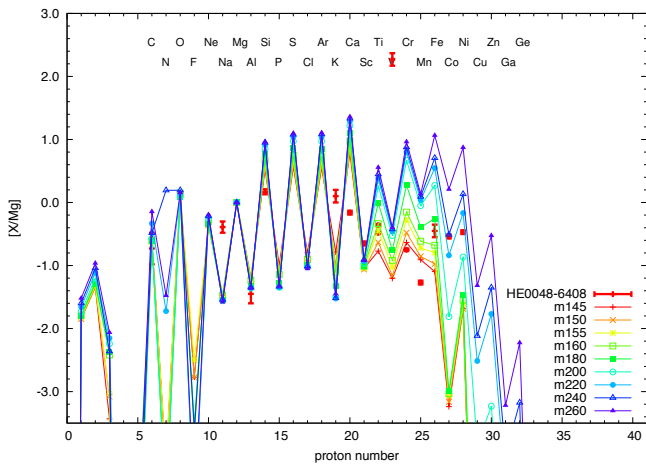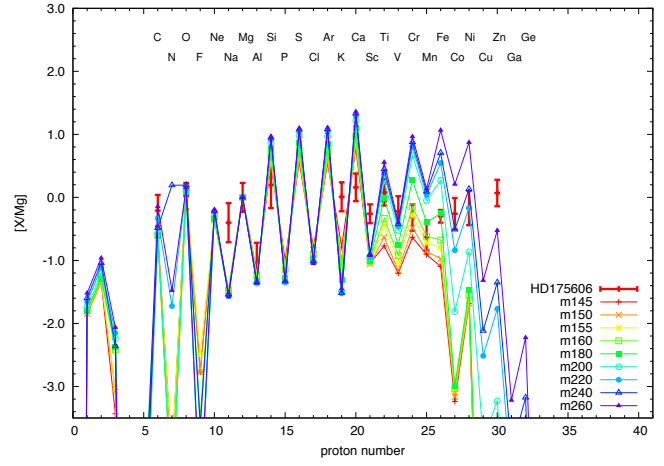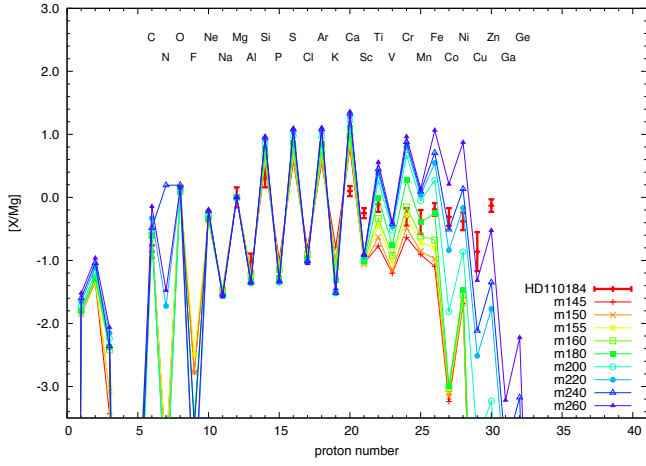
Figure C.9: Same as C.1. Stars of #47–52 in Tab. 5.4 are plotted.
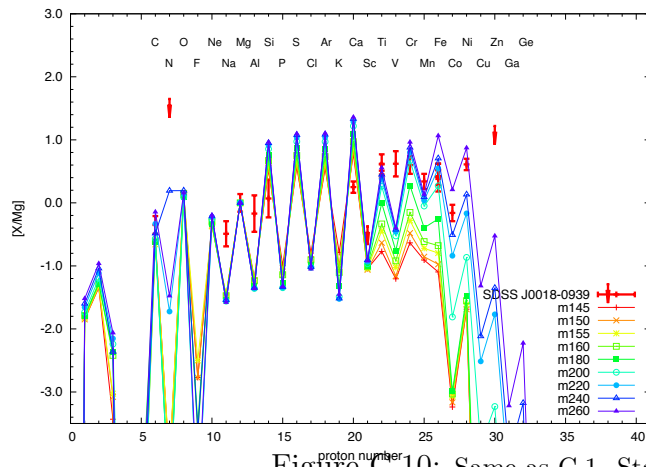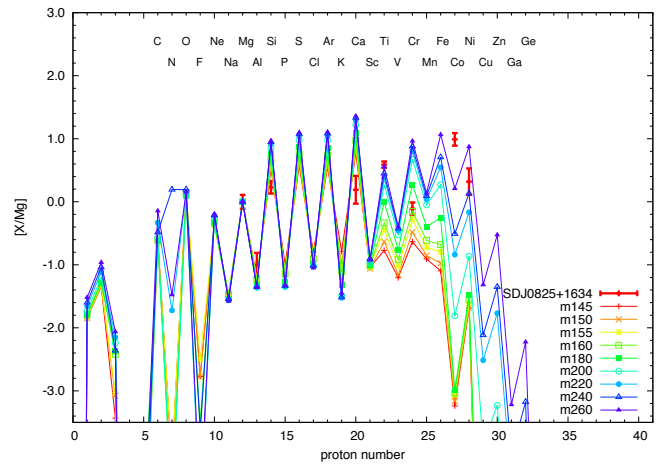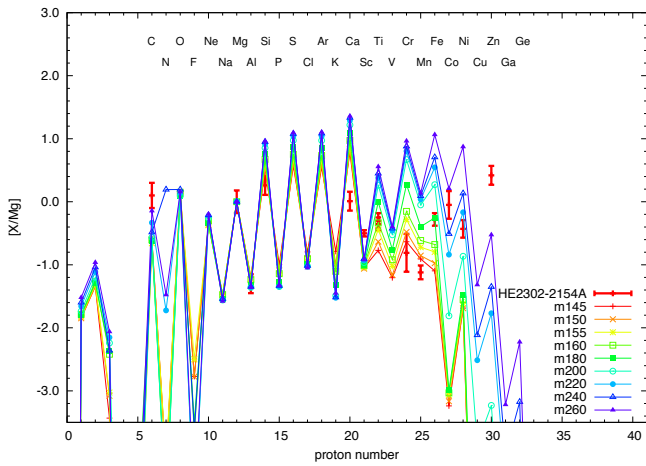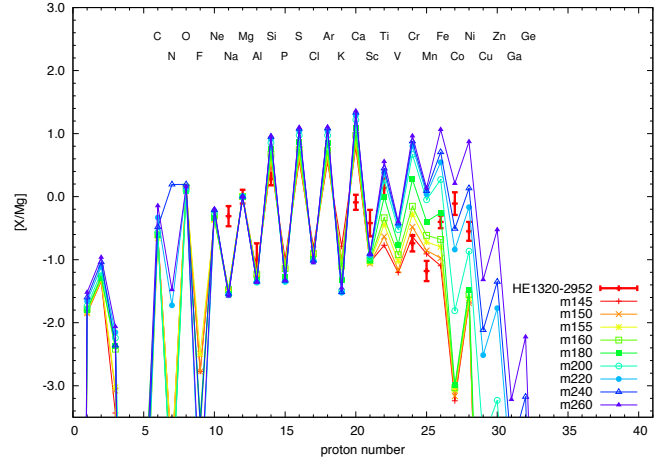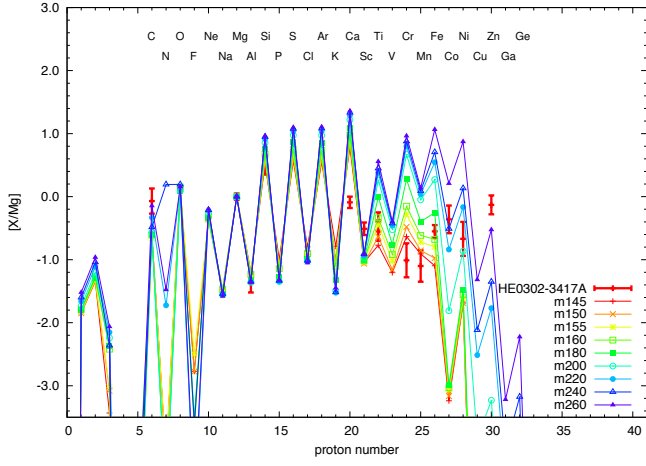
Figure C.10: Same as C.1. Stars of #53–57 in Tab. 5.4 are plotted.